PHENOTYPIC AND GENETIC VARIATION IN THE ARCHITECTURAL RESPONSES OF A C_4 GRASS TO DROUGHT STRESS

BY

DARSHI BANAN

DISSERTATION

Submitted in partial fulfillment of the requirements
for the degree of Doctor of Philosophy in Plant Biology
in the Graduate College of the
University of Illinois at Urbana-Champaign, 2019

Urbana, Illinois

Doctoral Committee:

Associate Professor Carl Bernacchi, Chair
Professor Andrew Leakey, Director of Research
Professor Don Ort
Dr. Ivan Baxter, Donald Danforth Plant Science Center

ABSTRACT

Improvement of next generation C_4 grass feedstocks is a promising avenue towards meeting the challenge of sustainably ensuring global food and fuel security in the face of climate change. C_4 grasses are inherently resource use efficient, have a variety of food, fuel, and other industrial product applications, and already play a large role in global agriculture. Ideally biofuel feedstocks should be grown on marginal and potentially drought prone acreage to avoid displacement of food production. Therefore, next generation C_4 grass feedstocks must be both highly productive and highly drought tolerance. Plant architecture provides a framework for finding a balance between these targets. Plant architecture is the organization of the plant body and enables the capture of resources, influences the local microenvironment, and ensures reproductive success. Due to its impacts on productivity and the maintenance of productivity in response to environmental stress, tailored modification of plant architecture is a focus of modern breeding efforts. Imaging techniques are widely used in modern crop improvement efforts to accelerate the detection of useful genotype-to-phenotype associations. Here we used *Setaria viridis* mapping populations as a field-based C_4 grass model system for understanding plant architectural responses to drought stress. Various imaging techniques were applied with the intent of capturing aspects of plant architecture within specific nuanced contexts determined by choice of imaging field of view, point of view, and time frame. Imaging within these contexts constrained the physiological, anatomical, and developmental interpretation of the image outputs. First, we show that canopy hemispherical imaging combined with light attenuation modeling is an effective means of detecting the same genotype-to-phenotype associations for aboveground biomass as laborious and destructive traditional harvests. However, hemispherical imaging was unable to resolve specific architectural contributions to growth. Next, we apply the same hemispherical imaging system to evaluate the canopy light environment at specific times of day to show that leaf rolling serves to temporarily reduce canopy radiation use as part of strategy to limit water use over prolonged periods of drought stress. Finally, image-based measurements of internode elongation and arrangement were combined with a modeled growth function to reveal the positive response of reproductive internodes to water-deficit and the compensatory effect that vegetative internode elongation has on recovering height lost to stress. Furthermore, the resulting phenotypes were correlated with life strategy and local adaptation and explained

genotype-to-phenotype associations that were missed by coarser measurements of growth. These results emphasize the power of low-cost digital imaging techniques when placed within effective contexts.

TABLE OF CONTENTS

CHAPTER 1: INTRODUCTION……..…1

CHAPTER 2: HIGH FIDELITY DETECTION OF CROP BIOMASS QTL FROM LOW-COST IMAGING IN THE FIELD……..10

CHAPTER 3: PHYSIOLOGICAL PLASTICITY THROUGH LEAF ROLLING AS A MEANS TO CONSERVE WATER AND MAINTAIN GROWTH OVER LONGER PERIODS IN A C_4 GRASS UNDER DROUGHT STRESS IN THE FIELD…….……31

CHAPTER 4: SUCCESSIVE INTERNODES AS A POSTMORTEM SIGNATURE OF ELONGATION RESPONSES TO DROUGHT……...….64

CHAPTER 5: CONCLUSIONS…….……119

CHAPTER 1
INTRODUCTION

Plant architecture is the shape that a plant's body takes in three-dimensional space. This shape is generated from the interplay of genes and gene networks with signals transduced from environmental variability. A plant's physical shape enables the capture of resources, alters the microenvironment, and allows for successful reproduction and distribution. Because plants are rooted in place and unable to immediately flee to more favorable conditions, the optimization of plant architecture in different developmental and spatiotemporal contexts is a vital part of plant responses to the environment. Within a human context, the consequences of plant architecture play an important role in determining productivity and maintaining productivity in response to environmental stress. Due to its influence on productivity and stress response, integrating plant architecture into crop improvement efforts is critical to meeting global food and fuel demands in a sustainable fashion.

Global population growth and development are placing an increased demand on plant-derived food, fibers, and fuels. However, current rates of yield gain are not on track to meet projected demand (Tilman et al., 2011; Ray et al., 2013). Biomass crops that produce the raw feedstock for liquid fuel production, direct combustion, and other industrial products have the potential to form the foundation of a domestic energy source capable of reducing greenhouse gas emissions (Hudiburg et al., 2016). As this form of biomass production becomes more widely adopted, it is important to maximize production per unit ground area grown under marginal conditions to ensure yield stability and profitability, avoid the displacement of food crop acreage and natural ecosystems, and provide resilience against climate change (Somerville et al., 2010). Climate change increasingly presents extreme and highly variable weather conditions that are pushing the norms of conventional agricultural practices. Improving yield and yield stability under these complex and urgent conditions requires targeted approaches. Relative to traditional food crops, there has been very little investment in the genetic improvement of the next generation of biomass crops. Therefore, there is great opportunity for rapid improvement.

An important step in crop improvement is uncovering genotype-to-phenotype associations for traits of interest (Furbank and Tester, 2011). This approach combines advances in genotyping (Poland and Rife, 2012; He et al., 2014), the development of mapping populations

(Casa et al., 2008; Li and Brutnell, 2011), the design and analysis of quantitative genetic experiments (Myles et al., 2009; Morrell et al., 2011), and high-throughput phenotyping (Araus and Cairns, 2014) to produce a predictive model of genotype-to-phenotype relationships that allows for an accelerated and more targeted approach to plant breeding. However, despite these advances, there remains the challenges of determining what phenotypes are interpretable and scalable in the context of phenomics and physiologically relevant to the particular production context.

Perennial C_4 grasses, such as miscanthus and switchgrass, are promoted as a next generation feedstock source. Their perennial life cycle means that these candidate feedstocks require less inputs, have a longer growing season that intercepts more photosynthetically active radiation (PAR), and provides ecosystem services such as habitat and soil stability. The use of perennial C_4 grass feedstocks in the production of aviation fuels or in a bioenergy and carbon capture system (BECCS) has the potential to drastically reduce carbon emissions from the travel sector and even drive negative emissions in the energy sector. The C_4 photosynthetic pathway is typified by a specialized Kranz anatomy bundle sheath that acts a CO_2 concentrating mechanism. This provides C_4 plants with higher nutrient and water use efficiency relative to their C_3 counterparts (Osborne and Sack, 2012; Atkinson et al., 2016) and alters the allocation and shape that C_4 grasses may take in response to the environment. These perennial grasses join other C_4 grasses such as maize, sugarcane, sweet sorghum, and energy sorghum to form a collection of highly productive and resource use efficient crops that play an outsized role in global agriculture. Of these C4 grasses, maize has the longest history of both ancient and modern improvement efforts (Wallace et al., 2014). The majority of other C4 grasses proposed as next generation feedstocks, especially the perennial miscanthus and switchgrass, are largely unimproved (Somerville et al., 2010).

With regards to the endogenous control of aboveground plant architecture, the literature suggests that relatively few genes have been the target of selection during domestication (Teichmann and Muhr, 2015). The physiological and molecular basis behind several crop architectural adaptations have been well studied. Decreased leaf angle in maize is the product of increased planting densities in modern cultivars and is shown to improve the redistribution and utilization of radiation by the canopy (Fellner et al., 2006; Ford et al., 2008). Similar results have been observed in assessing the impact of reduced leaf angle on energy sorghum productivity

(Troung et al., 2015). Yield improvements associated with the 1960's Green Revolution were largely produced by selection for short, sturdy stemmed varieties that could produce heavy grain and resist lodging. These changes in stem architecture were the result of an alter response to the hormone gibberellin and conferred by mutant dwarfing alleles at two specific loci (Peng et al., 1999). Despite this research on plant architecture produced under ideal growing conditions and despite their high water use efficiency, C_4 grasses remain largely understudied with respect to the genetic basis of architectural responses to abiotic stress.

Drought, the mismatch between water supply and water demand, is a major abiotic stress that marginalizes acreage, is responsible for large economic losses, and is projected to become more widespread, intense, and prolonged as climate change intensifies (Blum, 2011; Thiry et al., 2016). To both ensure that productivity is stable in the face of abiotic stress and land use does not unduly displace acreage for food production, optimizing aboveground architecture to improve the drought tolerance of next generation C_4 grasses should be prioritized. Drought tolerance in a crop production context can be defined as the ability of plants to grow and reproduce to generate a satisfactory yield despite limited water supply or periodic water deficit (Turner and Begg., 1981; Fleury et al., 2010). Plant architecture strongly influences productivity and the modification of certain aspects of plant architecture can help to maintain productivity despite stress. Potential strategies for modifying plant architecture in response to drought stress include the maintenance of cell elongation processes in maize and *Setaria* (Boyer, 1970; Martin et al., 2016; McCoughy et al., 2016) as well as the avoidance of acute stress via temporary reduction in leaf area (O'Toole, 1979; Dingkuhn et al., 1989; Heckathorn and DeLucia, 1991).

Despite progress made in streamlining components of the crop improvement pipeline, the ability to rapidly measure complex traits such as aboveground plant architecture remains as a major bottleneck to detecting useful genotype-to-phenotype associations (Furbank and Tester, 2011). High-throughput phenotypic seeks to address this bottleneck by improving the scale of application of plant measurement techniques. Imaging lends itself well to measuring plant architecture (Busemeyer et al., 2013; Casadesus, 2014). Imaging captures an impression of plant shape which can be split based on developmental or spatiotemporal landmarks. These split impressions then produce outputs that can be used as quantitative traits that describe specific features of plant architecture. Numerous imaging approaches appear in the literature and display a wide range in complexity, cost, and scalability. Approaches may be field based using aerial,

rover, or rail based platforms; applied in controlled environments using high resolution, multi-spectrum imaging stations; or laboratory based using copy stands and flatbed scanners to image isolated tissues. Some of these applications require huge platforms and resources unavailable to the majority of practitioners, therefore it is important to develop methods that balance between scale, cost, and information within different contexts to promote the democratization of plant improvement efforts. Regardless of platform, the general protocol for the majority of imaging applications involves: (1) image collection; (2) classification of plant versus non-plant pixels; (3) extraction of morphological features or application of a biophysical model; (4) and, ideally, image interpretation should be integrated with other measurements collected as proximal to the phenotype of interest as possible.

The large size of many C_4 grasses makes them ungainly for whole plant evaluations of plant productivity and architecture, especially within logistically limited experiments that impose complex treatment designs. Enter genus *Setaria,* an emerging model system for C_4 grasses (Li and Brutnell, 2011). *Setaria* is closely related to current and next generation C_4 grass food and fuel crops. Compared to its panicoid grass relatives, *Setaria* has the advantage of having a small physical stature, fast life cycle, and diploid genome (Doust et al., 2009). *Setaria* is able to grow in very water limited conditions and the genus contains a diverse range of architectures, two important traits for revealing genes that may confer drought tolerance.

This research utilizes two *Setaria* mapping populations. The first population is an F7 recombinant inbred line (RIL) produced from the cross between the weedy *Setaria viridis* A10 and the domesticated *Setaria italica* B100 (Bennetzen et al. 2012). Both parents are Eurasian in origin. The two parents have contrasting architectural phenotypes that result from natural selection on *Setaria viridis* A10 and human selection on *Setaria italica* B100 and produced a wide range of progeny phenotypes that contain a mixture of weedy and domesticated influences. The RIL population allows for the detection of genotype-to-phenotype associations in the form of quantitative trait loci (QTL), or constrained segments of the genomes that are related to a trait of interest. The second population is a natural diversity panel of *Setaria viridis* accessions collected from across North America. This population represents the result of local adaptation by multiple subpopulations introduced to the continent from Eurasia with potential admixture by *Setaria italica*. The diversity panel allows for a genome wide association study which reveals relationships between single nucleotide polymorphisms (SNP) and a trait of interest.

The following three chapters describe the use of a variety of imaging techniques applied to *Setaria* mapping populations as a means to understand C_4 grass architectural responses to drought stress:

Chapter two applied hemispherical field of view imaging from a below canopy point of view and a physical model of light attenuation to capture a phenotypic signature of whole plant aboveground productivity. Applying this method to the RIL population grown in the field detected the same genotype-to-phenotype associations as direct, destructive measurements of biomass. However, the results also show that imaging at this scale does not have the ability to break productivity down into its component parts and suggest that more targeted approaches that further dissect the genetic landscape of productivity and aboveground architecture may be warranted especially in stress contexts.

Chapter three combined below canopy hemispherical imaging at multiple time frames with direct measures of leaf morphology to reveal the adaptive significance of leaf rolling in C_4 grasses. This approach sought to connect leaf morphology to the canopy light environment and emphasizes the importance of applying an appropriate spatiotemporal context. A visual leaf rolling score was used to characterize the diversity of the trait across a North American *Setaria viridis* accession panel and identified a subset of accessions that exhibited a high degree of leaf rolling and their closest non-rolling relatives. An assessment of the productivity and life history of this subset suggested that leaf rolling in *Setaria viridis* is a means to water loss over prolonged periods of water-deficit by temporarily reducing leaf surface area.

Chapter four used an overhead point of view to image dissected internode samples and a modeled growth function to show that internode elongation is dependent on internode function and position on the tiller. Also, internode dimension and arrangement within a tiller was correlated with productivity, life strategy, and the population structure, geography, and climate of North American *Setaria viridis* accessions. This chapter utilized both mapping populations and detected genotype-to-phenotype associations that better inform previous efforts to understand the genetics of aboveground productivity and architecture as well as unique associations that can be used to identify candidate genes.

Together, these chapters highlight the utility of using an array of imaging fields of view, points of view, and time frames applied within specific developmental and anatomical contexts.

The results show that the architectural responses of C_4 grasses to drought stress are dynamic and can potentially be used to accelerate the improvement of next generation biofuel feedstocks.

REFERENCES

Araus JL, Cairns JE (2014) Field high-throughput phenotyping: The new crop breeding frontier. Trends Plant Sci **19**: 52–61

Atkinson RRL, Mockford EJ, Bennett C, Christin P-A, Spriggs EL, Freckleton RP, Thompson K, Rees M, Osborne CP (2016) C4 photosynthesis boosts growth by altering physiology, allocation and size. Nat Plants **2**: 16038

Bennetzen JL, Schmutz J, Wang H, Percifield R, Hawkins J, Pontaroli AC, Estep M, Feng L, Vaughn JN, Grimwood J, et al (2012) Reference genome sequence of the model plant Setaria. Nat Biotechnol **30**: 555–61

Blum A (2011) Drought resistance is it really a complex trait? Funct Plant Biol **38**: 753–757

Boyer JS (1970) Leaf enlargement and metabolic rates in corn, soybean at various leaf water potentials. Plant Physiol **46**: 236–239

Busemeyer L, Ruckelshausen A, Möller K, Melchinger AE, Alheit K V, Maurer HP, Hahn V, Weissmann E a, Reif JC, Würschum T (2013) Precision phenotyping of biomass accumulation in triticale reveals temporal genetic patterns of regulation. Sci Rep **3**: 2442

Casa AM, Pressoir G, Brown PJ, Mitchell SE, Rooney WL, Tuinstra MR, Franks CD, Kresovich S (2008) Community resources and strategies for association mapping in Sorghum. Crop Sci **48**: 30–40

Casadesús J, Villegas D (2014) Conventional digital cameras as a tool for assessing leaf area index and biomass for cereal breeding. J Integr Plant Biol **56**: 7–14

Dingkuhn M, Cruz RT, O'Toole JC, Dörffling K (1989) Net photosynthesis, water use efficiency, leaf water potential and leaf rolling as affected by water deficit in tropical upland rice. Aust J Agric Res **40**: 1171–1181

Doust AN, Kellogg EA, Devos KM, Bennetzen JL (2009) Foxtail Millet: A Sequence-Driven Grass Model System [W]. **149**: 137–141

Fellner M, Ford ED, Van Volkenburgh E (2006) Development of Erect Leaves in a Modern Maize Hybrid is Associated with Reduced Responsiveness to Auxin and Light of Young Seedlings In Vitro. Plant Signal Behav **1**: 201–211

Fleury D, Jefferies S, Kuchel H, Langridge P (2010) Genetic and genomic tools to improve drought tolerance in wheat. J Exp Bot **61**: 3211–3222

Ford ED, Cocke A, Horton L, Fellner M, Van Volkenburgh E (2008) Estimation, variation

and importance of leaf curvature in Zea mays hybrids. Agric For Meteorol **148**: 1598–1610

Furbank RT, Tester M (2011) Phenomics - technologies to relieve the phenotyping bottleneck. Trends Plant Sci **16**: 635–644

Heckathorn SA, DeLucia EH (1991) Effect of Leaf Rolling on Gas Exchange and Leaf Temperature of Andropogon gerardii and Spartina pectinata Author (s): Scott A. Heckathorn and Evan H. DeLucia Published by: The University of Chicago Press Stable URL: http://www.jstor.org/stable/29952. Bot Gaz **152**: 263–268

Hudiburg TW, Wang W, Khanna M, Long SP, Dwivedi P, Parton WJ, Hartman M, Delucia EH (2016) Impacts of a 32-billion-gallon bioenergy landscape on land and fossil fuel use in the US. Nat Energy **1**: 1–7

Li P, Brutnell TP (2011) Setaria viridis and Setaria italica, model genetic systems for the Panicoid grasses. J Exp Bot **62**: 3031–3037

Morrell PL, Buckler ES, Ross-Ibarra J (2011) Crop genomics: advances and applications. Nat Rev Genet **13**: 85–96

Myles S, Peiffer J, Brown PJ, Ersoz ES, Zhang Z, Costich DE, Buckler ES (2009) Association mapping: critical considerations shift from genotyping to experimental design. Plant Cell **21**: 2194–2202

O'Toole JC (1979) Leaf rolling and transpiration. Plant Sci Letters **16**: 111–114

Osborne CP, Sack L (2012) Evolution of C4 plants: a new hypothesis for an interaction of CO2 and water relations mediated by plant hydraulics. Philos Trans R Soc B Biol Sci **367**: 583–600

Peng J, Richards DE, Hartley NM, Murphy GP (1999) "Green revolution" genes encode mutant gibberellin response modulators. PNAS **400**: 8–13

Poland J a, Rife TW (2012) Genotyping-by-Sequencing for Plant Breeding and Genetics. Plant Genome **5**: 92–102

Ray DK, Mueller ND, West PC, Foley JA (2013) Yield Trends Are Insufficient to Double Global Crop Production by 2050. PLoS One. doi: 10.1371/journal.pone.0066428

Somerville C, Youngs H, Taylor C, Davis SC, Long SP (2010) Feedstocks for lignocellulosic biofuels. Science (80-) **329**: 790–792

Teichmann T, Muhr M (2015) Shaping plant architecture. Front Plant Sci **6**: 233

Thiry AA, Chavez Dulanto PN, Reynolds MP, Davies WJ (2016) How can we improve crop

genotypes to increase stress resilience and productivity in a future climate? A new crop screening method based on productivity and resistance to abiotic stress. J Exp Bot **67**: erw330

Tilman D, Balzer C, Hill J, Befort BL (2011) Global food demand and the sustainable intensification of agriculture. Proc Natl Acad Sci United States Am United States Am **108**: 20260–20264

Turner NC, Begg JE (1981) Plant-water relations and adaptation to stress. Plant Soil **58**: 97–131

Wallace JG, Larsson SJ, Buckler ES (2014) Entering the second century of maize quantitative genetics. Heredity (Edinb) **112**: 30–38

CHAPTER 2
HIGH FIDELITY DETECTION OF CROP BIOMASS QTL FROM LOW-COST IMAGING IN THE FIELD [1]

ABSTRACT

Field-based, rapid, and non-destructive techniques for assessing plant productivity are needed to accelerate the discovery of genotype-to-phenotype relationships in next-generation biomass grass crops. The use of hemispherical imaging and light attenuation modeling was evaluated against destructive harvest measures with respect to their ability to accurately capture phenotypic and genotypic relationships in a field-grown grass crop. Plant area index (PAI) estimated from below-canopy hemispherical images, as well as a suite of thirteen traits assessed by manual destructive harvests, were measured in a *Setaria* recombinant inbred line mapping population segregating for aboveground productivity and architecture. A significant correlation was observed between PAI and biomass production across the population at maturity ($r^2 = 0.60$), as well as for select diverse genotypes sampled repeatedly over the growing season ($r^2 = 0.79$). Twenty-seven quantitative trait loci (QTL) were detected for manually collected traits associated with biomass production. Of these, twenty-one were found in four clusters of co-localized QTL. Analysis of image-based estimates of PAI successfully identified all four QTL hotspots for biomass production. QTL for PAI had greater overlap with those detected for traits associated with biomass production than with those for plant architecture and biomass partitioning. Hemispherical imaging is an affordable and scalable method, which demonstrates how high-

1 This chapter was published in *Plant Direct* in February 2018 and is copied here with permission

Authors: Darshi Banan[1], Rachel E. Paul[1], Max Feldman[2], Mark Holmes[1], Hannah Schlake[1], Ivan Baxter[3], Hui Jiang[2], Andrew D.B. Leakey[1] *

[1] University of Illinois Urbana Champaign 1402 IGB 1206 W Gregory Dr Urbana, IL 61801 USA
[2] Donald Danforth Plant Science Center 975 North Warson Road St. Louis, MO 63132 USA
[3] USDA-ARS, Donald Danforth Plant Science Center 975 North Warson Road St. Louis, MO 63132 USA

Author contributions: A.D.B.L. conceived the original research plans; A.D.B.L., I.B., D.B. and R.E.P. supervised the experiments; H.J. provided seed for the mapping population, M.H. and H.S. collected validation data; D.B., R.E.P., and M.H. collected images and biomass data; D.B. and M.H. processed hemispherical images; R.E.P., M.F. and I.B. performed QTL analysis; D.B. and A.D.B.L. analyzed the data; D.B. and A.D.B.L. wrote the article; all authors reviewed and commented on the article.

throughput phenotyping can identify QTL related to biomass production of field trials in place of destructive harvests that are labor, time, and material intensive.

INTRODUCTION

Current rates of yield gain are unlikely to meet the projected demands of global population growth and development (Tilman et al., 2011; Ray et al., 2013). High-throughput phenotyping (HTP) techniques rapidly evaluate plant performance and leverage advances in genotyping (Bennetzen et al., 2012; Poland and Rife, 2012; He et al., 2014), the development of mapping populations (Casa et al., 2008; Doust et al., 2009; Li and Brutnell, 2011), and the design and analysis of quantitative genetic experiments to ultimately develop a predictive understanding of genotype-to-phenotype relationships (Myles et al., 2009; Morrell et al., 2011). This understanding enables an accelerated and more targeted approach to crop improvement (Furbank and Tester, 2011; Araus and Cairns, 2014). Biomass production generates both the calories that are partitioned towards food consumption and the raw feedstock used for carbon efficient biofuels (Hudiburg et al., 2016). Biomass productivity per unit ground area must be maximized to ensure profitability and avoid displacement or disturbance of natural ecosystems (Somerville and Long, 2015). However, biomass is a complex trait that is difficult to assess in the field and usually is measured by destructive harvest (White et al., 2012). We addressed this challenge by testing the ability of hemispherical imaging to identify genomic regions associated with above-ground biomass production. The successful application of hemispherical imaging was evaluated with respect to its strong phenotypic correlation and high degree of QTL co-localization with directly validated destructive harvest traits.

Numerous remote sensing methods have been demonstrated to correlate with destructive measures of biomass production and can be considered proxy measurements (Gitelson et al., 2003; Casadesús and Villegas, 2014; Li et al., 2015; Parent et al., 2015). These include multispectral and hyperspectral indices of radiation reflected from crop canopies, as well as measures of canopy light distribution. Often, a combination of sensor outputs and additional processing techniques such as regression, inverse modeling, and multivariate analysis are required to produce relevant phenotypes (White et al., 2012; Fiorani and Schurr, 2013). Tanger et al (2017) used a combination of tractor-mounted multispectral reflectance and ultrasonic sensors to detect manually validated QTL associated with biomass in rice (Tanger et al., 2017). Similar measurements have been deployed in other field-grown crops using ground vehicles, aerial

vehicles and gantries requiring investment in equipment that often exceeds $100,000s - $1,000,000s (Pauli et al., 2016; Vergara-díaz et al., 2016). In addition to the expense of HTP equipment, many techniques under development require extensive research infrastructure, permits (e.g. flight authorization) and complex data analyses. Highly trained personnel are consequently needed to support both data acquisition and analysis. Unfortunately, these factors combine to mean that the majority of HTP techniques can only feasibly be used by large research intuitions and companies. And, even in those organizations deployment of HTP has to be limited to a few high priority projects. Cheap methods of HTP that rely on simpler technology could greatly increase how widely HTP is adopted, and support work in a broader diversity of environmental conditions and crops outside of the major growing regions of the world's staple crops.

Hemispherical imaging captures the geometry of sky openings and models the attenuation of solar radiation by the canopy to estimate canopy properties, such as Leaf Area Index (LAI; leaf area per unit ground area) (Anderson, 1964; Rich, 1990). The ability to account for the influence of both stems and leaves allows its use for estimating Plant Area Index (PAI; above-ground plant tissue area per unit ground area) in herbaceous systems (Neumann et al., 1989). Canopy properties estimated from hemispherical images use mechanistic and biophysical models rather than reliance on statistical relationships between sensor and subject. Therefore, they should be less context dependent and more widely applicable to different crops, growing conditions, and management practices than other methods that require a training model to relate remotely sensed data to traditional measures of crop productivity (e.g. Busemeyer et al 2013). Traditionally, hemispherical photography equipment is tall, bulky, and not suited to crop HTP. In this study, a miniature remotely triggered digital camera designed for point-of-view action sport videography (GoPro Hero 3+, GoPro Inc, San Mateo, CA, USA) was modified with a miniature hemispherical lens (1.39 mm hemispherical lens, Quality Video Components LLC, Sparta, MI, USA) and mounted to a custom-built self-leveling gimbal (Fig. 1A-C). The resulting system was small enough to fit between tight crop rows and below the crop canopy.

An F7 recombinant inbred line (RIL) mapping population with 186 genotypes generated from a cross between the cultivated *Setaria italica* and its weedy ancestor *Setaria viridis* provides an ideal platform for assessing the ability of hemispherical imaging to detect QTL related to above-ground biomass production due to its wide diversity of morphologies and multi-

fold variation in biomass production (Doust et al., 2009; Bennetzen et al., 2012). As a model C_4 grass emerging as a tool for systems-level biology, the genus *Setaria* has the advantage of being closely related to C_4 grass food and fuel crops such as maize, sorghum, miscanthus, and switchgrass, while having a smaller stature, faster life cycle, and diploid genome (Brutnell et al., 2010). Here we use an inexpensive and simple, miniaturized system of hemispherical imaging and light attenuation modeling to identify the same set of key QTLs for biomass production as traditional destructive harvest methods applied to a field-grown *Setaria* mapping population. This provides a case study of a HTP technology that can deliver results for QTL mapping without high costs or complexity.

RESULTS AND DISCUSSION

First, a validation experiment determined whether the customized imaging system was suitable for HTP in *Setaria. Setaria viridis, Setaria italica,* and the phenotypically intermediate RIL #161 derived from crossing these two species were used as test material because they vary widely in canopy architecture and rate of biomass production. Each genotype was grown in eight replicated plots of which four were randomly chosen for measurement. An independent plot for each genotype was selected for collection of both hemispherical images and destructive canopy and biomass harvest measures on four dates distributed across the growing season to generate a wide range of canopy closures and biomasses with which to evaluate hemispherical imaging. Notably, total above-ground biomass correlated more strongly with PAI (r^2=0.79) than it did with destructively measured LAI (r^2=0.55, Figure 2.1 D). This difference in correlation with total above-ground biomass likely results from the ability of hemispherical imaging to evaluate all visible plant elements versus destructive LAI accounting only for plant elements identified as leaf. This highlights the ability of hemispherical imaging to robustly assess the total amount of plant tissue over an area of ground across a diversity of short, herbaceous grass canopies in a non-destructive manner. Data is easy to acquire and analyze since the camera, lens and analysis software are all commercially available.

Next, the ability of hemispherical imaging to detect QTLs for biomass production was tested in a *Setaria* F7 RIL mapping population. 186 RILs were planted in an unreplicated randomized design with six check plots for each parent. Hemispherical images, manually measured morphological traits, and destructive harvest weight data were collected from the same plots of each genotype.

Results from manual measures of developmental, architecture, and biomass production traits showed that the segregating population was phenotypically diverse for a comprehensive set of destructive harvest traits assessed at maturity, including total above-ground biomass, tiller number, and height (Supplemental Table 2.1).

Principal component analysis (PCA) was performed on directly measured traits – leaf mass, panicle mass, stem mass, branch number, clump spread, culm height, tiller height, days-after-sowing until panicle emergence, and reproductive-to-vegetative mass ratio – to simplify the description of plant performance relative to hemispherical imaging estimates (Figure 2.2). The first three principal components (PCs) with eigenvalues greater than 1.00 together explain 76% of the variation in the dataset. The trait loadings based on eigenvectors in each of these three orthogonal PCs appear to describe three plant growth components: (1) biomass production, (2) bushiness, and (3) partitioning of biomass to vegetative versus reproductive structures. Days-after-sowing until panicle emergence varied significantly within the RIL population, loading moderately in both PC1 and PC3, but not strongly in any single PC. PC1 accounted for 44% of overall variation and approximates above-ground biomass production based on strong loadings for culm height, tiller height, leaf mass, panicle mass, and stem mass. PC2 accounted for 20% of variation and approximates plant bushiness based on strong loadings for clump spread, branch number, and tiller number. PC3 accounted for 12% of variation and approximates the partitioning of biomass to vegetative versus reproductive structures based on strong loadings for panicle mass and reproductive-to-vegetative mass ratio.

These apparent descriptions, while not definitive, are biologically intuitive and provide a framework for interpreting the genetic and phenotypic attributes of a plant in the field. Correlation analysis of all traits measured shows that PAI correlated positively and strongly with total mass, vegetative mass, and with the other traits that loaded strongly into PC1 to describe biomass production (Figure 2.3).

Quantitative trait loci analysis detected 53 significant QTL across 12 traits (Supplemental Table 2.2). The identified loci clustered in groups corresponding with the segregation of traits into the three different PCs (Figure 2.4). This suggests that the variation underlying the separation of PCs is driven by genetic programs related to biomass production, bushiness, and partitioning of biomass to vegetative versus reproductive structures rather than uncontrolled physiological or environmental factors.

QTL for PAI were co-located with all four of the hotspots of QTL for traits related to above-ground biomass production evaluated in destructive harvests. These four hotspots found on chromosomes 2, 5, 6, and 9 featured QTL for between five and seven traits, including PAI, total mass, vegetative mass, leaf mass, stem mass, culm height, and tiller height. All PAI and biomass productivity QTL within the four hotspots had positive additive effects. Together, these loci appear to represent the primary features of the genetic architecture of above-ground biomass production in *Setaria.* There was very little overlap between the location of these QTL hotspots for biomass production and QTL for traits associated with bushiness or vegetative-to-reproductive biomass ratio. Single QTL each for PAI and leaf mass co-localized on chromosome 8 and both had positive additive effects. Additionally, isolated QTL for leaf mass (chromosome 3 @ position 107 cM) and culm height (9@131) did not overlap with QTL for PAI. In contrast to all the other QTLs for traits associated with biomass production, QTL for culm height and tiller height had negative additive effects and co-located with a single QTL for reproductive-to-vegetative mass ratio (5@100). There was also very close correspondence between QTL identified for PAI and other productivity traits in the study with an independent field experiment on the same RIL population in Oklahoma (Mauro-Herrera and Doust, 2016). This provides strong evidence in support of using HTP of PAI to evaluate the genetic architecture of field-grown grass crops biomass productivity.

Twelve QTL for traits related to plant bushiness and nine QTL for traits related to partitioning of biomass to vegetative versus reproductive structures were detected. Notably, there was minimal overlap between QTL for PAI and those for traits associated with plant bushiness and biomass partitioning rather than biomass production. So, while hemispherical imaging is a powerful tool for assessing the genetic architecture of productivity traits in the field, other more complex field imaging techniques or laboratory based methods will be needed to quickly phenotype plant architectural traits (McCormick et al., 2016; Fernandez et al., 2017).

QTL for PAI captured the main features of the genetic architecture for directly measured traits related to biomass productivity (PC1), but in a non-destructive and far less laborious manner and without the need for intermediate calibration models. This was achieved with a minimal number of genotypes (186), replicates (1), and subsampling (2), confirming the method's power to detect the genetic components of variation in biomass productivity. In addition to its high detection fidelity, hemispherical imaging has the characteristics of an ideal,

scalable HTP technique. Compared to the manual traits that it parallels, hemispherical imaging is very efficient (4 person-hours for image collection and 7 for image analysis compared to 148 person-hours for destructive biomass harvest and 15 person-hours for sample weighing). The equipment used to collect hemispherical images is easy to operate, inexpensive, and commercially available. Image processing and analysis was accomplished using a commercially available software (HemiView, Delta-T Devices Ltd, Cambridge, UK) on a standard desktop computer and did not require additional data streams. This simplicity, low-cost, and universally applicable principle of operation mean that the method could be deployed on diverse crops at any location by a small team of personnel with limited training. The equipment is compact and lightweight, meaning that it can also be deployed on a rover to further accelerate image collection, improve the signal-to-noise ratio, and uncover the temporal dynamics of biomass productivity.

MATERIALS AND METHODS

Validation experimental design

Setaria viridis and *Setaria italica,* the parents of the F7 RIL population, and the phenotypically intermediate RIL #161 were grown on the South Farms at the University of Illinois Urbana Champaign in summer 2014. The field site is rain-fed, tile-drained, has a deep, organically rich, Flanagan/Drummer series type soil. RIL #161 was selected as a phenotypic intermediate between *S viridis* and *S italica* because of its placement in the 50th percentile for both culm height and tiller number. The experiment was a randomized complete block design with all three genotypes replicated in eight plots of which four were randomly chosen for measurement. Each plot was 4 m^2 with 25 cm grid spacing between plants. Data was collected from an independent plot of each genotype on four dates through the growing season. This resulted in significant variation in height, biomass production, canopy architecture, and PAI. Measured plots were not used for subsequent data collection.

First, non-destructive estimates of PAI were generated using HemiView software (Delta-T Devices Ltd, Cambridge, UK) to analyze 6 canopy hemispherical photographs taken either within or between planting rows near the plot center under diffuse light conditions (pre-dawn, dusk, or high cloud cover). Hemispherical photographs were taken with a GoPro Hero 3+ digital camera (GoPro Inc, San Mateo, CA, USA) modified with a fully hemispherical lens (1.39 mm hemispherical lens, Quality Video Components LLC, Sparta, MI, USA) and mounted on a

custom-built miniature self-leveling gimbal. Second, 8 or 16 plants (depending on collection date) were harvested from each plot, and separated into leaf, stem, and reproductive tissues. Fresh leaves were laid flat and photographed with a digital SLR camera (Cannon EOS 7D, 50mm lens, Canon Inc, Huntington, NY, USA) alongside a scaling object to allow estimation of total leaf area using ImageJ (National Institutes of Health, Bethesda, MD, USA). All tissues were then dried at 65^{o}C and weighed.

QTL experimental design

186 F7 recombinant inbred lines from an interspecific cross between *Setaria italica* x *Setaria viridis* were evaluated on the South Farms at the University of Illinois Urbana-Champaign in summer 2014. Seeds were germinated in greenhouses and transplanted by hand into a mechanically tilled field 7 days after sowing. The experiment was an un-replicated randomized design with six check plots for each parent. Data was collected from a single plot (36 plants, 1 m^2, 20 cm grid spacing between plants) of each RIL and six plots of each parent genotype.

Climate conditions

Over the duration of the validation experiment, the average air temperature was 21.7^{o}C, the average humidity was 72%, and the cumulative rainfall was 37.2 cm. Over the duration of QTL experiment, the average air temperature was 19.4^{o}C, the average humidity was 79%, and the cumulative rainfall was 18.9 cm.

Phenotyping

Panicle emergence was measured as the number of days after sowing at which the panicle head was seen past the collar of the flag leaf. The angle between the outermost tillers (i.e. clump spread) was measured in the field with a modified protractor 50 days after sowing. Non-destructive estimates of PAI were generated using Hemiview software (Delta-T Devices Ltd, Cambridge, UK) to analyze 2 canopy hemispherical photographs taken with a GoPro Hero 3+ digital camera manually placed either within or between planting rows at the plot center under diffuse light conditions at dusk or dawn when the canopy was near maximum size prior to senescence at the end of the growing season, between 67 and 70 days after sowing. The GoPro camera was customized by replacing the standard lens with a 1.39mm 190^{o} hemispherical lens and mounted on a custom-built self-leveling gimbal in order to insure the camera faced upwards from horizontal. Image capture was triggered using a hand-held Wi-Fi remote (GoPro Inc, San

Mateo, CA, USA) such that the operator remained out of frame. The camera was consistently staged such that the top of the image was oriented north. Two identical camera setups were used and images were analyzed by two people. A common set of images were processed and analyzed to confirm a lack of camera or person bias. End of season destructive harvest was done on three representative center plants in each plot beginning 72 days after sowing. Plants were cut at the base, separated into leaf, stem, and reproductive tissues, and the following morphological traits were measured. Culm height was measured as the length from the base of the plant to the collar of the flag leaf on the first emerged tiller. Tiller height was measured as the length from the base of the plant to the collar of the flag leaf on the second emerged tiller. Basal circumference was measured with a length of twine wrapped around the root crown. Tiller number was measured as the count of tillers emerging from the bottommost node. Branch number was measured as the count of primary branches emerging from nodes one or higher. The separated leaf, stem, and reproductive tissues were dried at 65^{o}C and weighed. Vegetative mass was calculated as the sum of leaf and stem mass. Total mass was calculated as the sum of leaf, stem, and panicle mass. All masses were standardized by planting density and are reported on a per unit ground area basis. The following R packages were used for data analysis and visualization: *ggplot2, plyr, reshape2,* and *ggrepel*. Data and scripts used in analyses are available in a .zip folder included in the supplemental information. Raw hemispherical images are hosted on Dryad and are available for community use.

Data transformation

Data were normalized using a second power, square root, or cube root transformation. Normality was assessed through the R function *shapiro.test* and the associated histograms and Shapiro Wilk's values. Results of the transformation procedures are shown in Supplemental Table 2.1**.**

Trait correlations

Trait correlations were tested using the R function *cor* using pairwise deletion to generate Pearson's coefficients of correlation and visualized with *corrplot.*

Principle Component Analysis

Principle component analysis was performed using the R function *prcomp,* with default parameters. 176 genotypes—those with complete sets of observations--were used in the principle component analysis. Evaluation of individual eigenvectors for each trait was used to describe the

significant PCs and used to parse the traits into biologically relevant groupings (Figure 2.2). The three most significant principle components were treated as individual traits in correlation analysis.

QTL analysis

QTL analysis was performed using "*foxy_qtl_pipeline",* available at https://github.com/maxjfeldman/foxy_qtl_pipeline, written by Max Feldman and adapted from *R/qtl* (Broman et al., 2003; Feldman et al., 2016). QTL detection was done using forward-backward Haley-Knott regression in order to build a multiple QTL model from each trait. A genome scan interval of 1 cM and a window size of 10 were used. 1,000 permutations were performed to estimate LOD (logarithm of the odds) threshold values. Additive effects were estimated as half the distance between phenotypic averages for the two homozygotes. To compare additive effects across traits with different scales, additive effects were normalized as a percent of the phenotypic mean (Des Marais et al., 2013). Co-localized QTL were grouped into "clusters" based on their mapping to same or neighboring markers where confidence intervals overlapped. Confidence intervals were calculated as the interval where the LOD score was within 1.5 units of its maximum. Lander and Botstein (1989) first proposed the use of 2 LOD support intervals and more recently Dupuis and Siegmund (1999) provided support for using the 1.5 LOD interval method (Lander and Botstein, 1989; Dupuis and Siegmund, 1999). The use of LOD support intervals as a method to estimate the location of QTL and define co-localized clusters continues in current plant biology QTL experiments (Topp et al., 2013).

Acknowledgements:

Funded through Subaward No. 23009-UI, CFDA #81.049 between University of Illinois and Donald Danforth Plant Science Center Under Prime Agreement No. DE-SC0008769 from Department of Energy

We thank Scott Baker and Jarad Bear for constructing the camera gimbal. We thank Kannan Puthaval and Mac Singer for technical support at the SoyFACE research facility. We thank Marshall Alston-Yeagle, Kara Barto, Johnathon Yockey, Sarah Keeley, Zach Reynado, Finey Ruan, and the many project partners from the Danforth Plant Science Center, Carnegie Institute, Washington State University, and University of Minnesota that helped with transplanting seedlings.

FIGURE AND TABLES

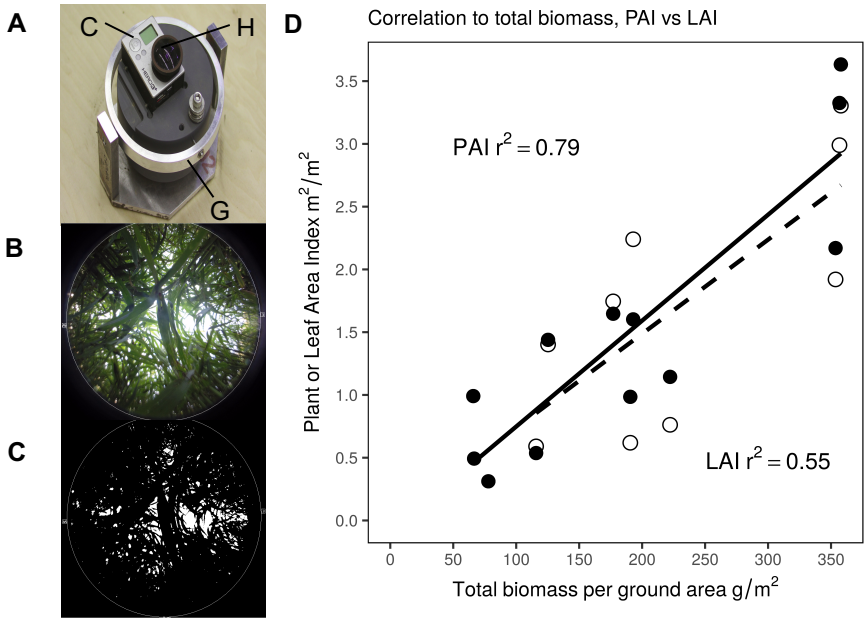

Figure 2.1: Customized hemispherical imaging system application to high throughput phenotyping of above-ground biomass production. A, A hemispherical lens (H) fitted on a GoPro Hero3+ digital camera (C) and mounted on a self-leveling gimbal (G). The camera unit had maximum dimensions of 5.8*4*3.7 cm and the full system was 11*15*13.3 cm. B, The system was used to capture fully hemispherical images of a plant canopy. C, Images were thresholded for analysis and estimation of Plant Area Index (PAI) using Delta-T Hemiview software. D, These estimates were correlated to total biomass (filled symbols, solid line) and compared to that between Leaf Area Index estimated from destructive harvest and total biomass (open symbols, dashed line). Measurements made on parent lines A.10, B.100 and phenotypically intermediate RIL#161 together represent a diversity of growth habit and morphology seen across the population. Symbols correspond to single plots from which all images and measurements were collected 38, 44, 52, and 60 days after sowing. Correlation r^2 values are reported for both measurements.

	PC1	PC2	PC3
Clump spread	0.0567	0.4673	0.1197
Tiller number	0.1015	0.4358	0.2538
Branch number	0.2357	0.4866	0.1732
Culm height	-0.4206	-0.1947	-0.0498
Second tiller height	-0.4332	-0.1118	-0.0226
Leaf mass	-0.4049	0.2478	0.216
Stem mass	-0.4266	0.1527	0.2055
Panicle mass	-0.3723	0.3511	-0.3114
Reproductive to vegetative mass ratio	-0.0365	0.3092	-0.7965
Panicle emergence days after sowing	-0.2837	0.0292	0.2607
Eigenvalue	2.1	1.41	1.09
Proportion of variance	0.44	0.2	0.12
Cumulative proportion	0.44	0.64	0.76

Figure 2.2: Principal component analysis of directly measured biomass traits. Trait loadings based on eigenvectors (color-coded by direction and magnitude, blue: positive, yellow: negative) in each principal component (PC) appear to describe three orthogonal processes: biomass production (PC1), bushiness (PC2), and partitioning of biomass to vegetative versus reproductive structures (PC3). The individual and cumulative contributions of each PC are reported.

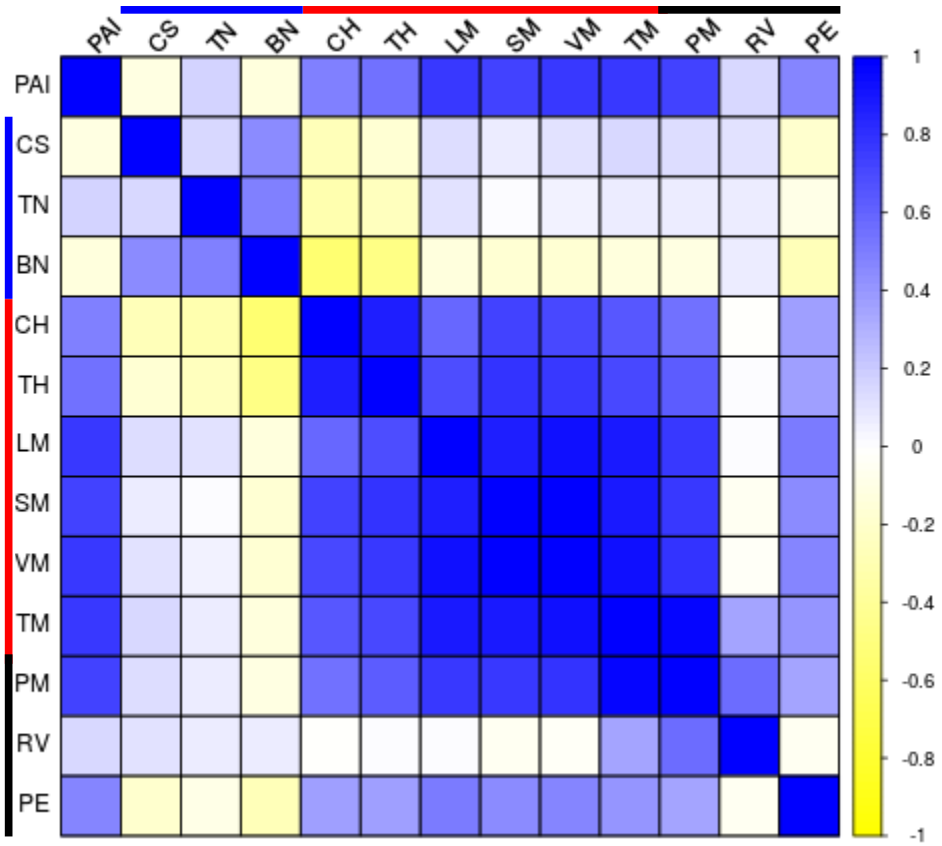

Figure 2.3: Correlation matrix of PAI and directly measured biomass traits. PAI correlates strongly and positively with traits associated with biomass production. Blue, yellow, and white cells represent positive, negative, and no correlation, respectively, between traits based on Pearson correlation coefficient values. Color bars at top and left indicate traits corresponding to bushiness (blue), biomass production (red), and partitioning of biomass to vegetative versus reproductive structures (black). PAI=plant area index, CS=clump spread, TN=tiller number, BN=branch number, CH=culm height, TH=second tiller height, LM=leaf mass per m^2 ground, SM=stem mass per m^2 ground, PM=panicle mass per m^2 ground, VM=vegetative mass per m^2 ground, TM=total mass per m^2 ground, RV=reproductive to vegetative mass ratio, PE=panicle emergence days after sowing.

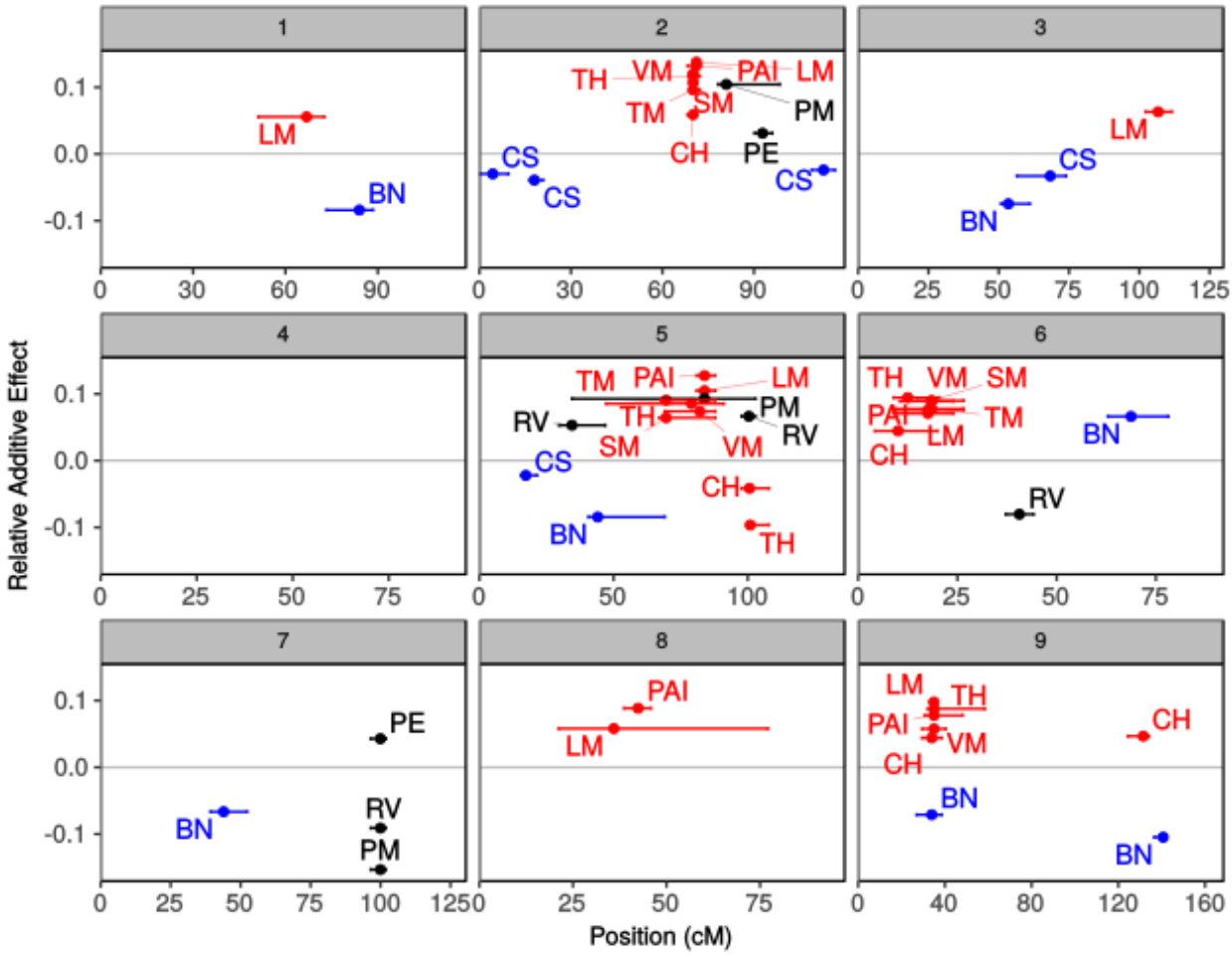

Figure 2.4: QTL mapping for PAI and directly measured biomass traits. Panels 1-9 correspond to each chromosome in the *Setaria* genome. Additive effects relativized by phenotypic mean are plotted against centimorgan position for each QTL. Error bars represent the 1.5 LOD score confidence intervals for each QTL's location. Colored points represent QTL corresponding to biomass production (red) bushiness (blue) and partitioning of biomass to vegetative versus reproductive structures (black). PAI=plant area index, CS=clump spread, BN=branch number, CH=culm height, TH=second tiller height, LM=leaf mass per m^2 ground, SM=stem mass per m^2 ground, PM=panicle mass per m^2 ground, VM=vegetative mass per m^2 ground, TM=total mass per m^2 ground, RV=reproductive to vegetative mass ratio, PE=panicle emergence days after sowing.

Supplemental Table 2.1: Summary of phenotyping results. Mean, number of observations, minima, maxima, range, fold change, and summary of transformation procedures for 13 measured traits are reported.

Trait	Mean	N	Minimum	Maximum	Range	Fold change	Transformation	Wilks statistic	P-value
Branch number (count)	3.47	185	1.00	7.39	6.39	6.39	square root	0.99	0.1908
Clump spread (degrees)	3.93	203	2.99	4.89	1.90	0.64	cube root	0.99	0.6265
Culm height (mm)	20.20	188	10.25	27.47	17.22	1.68	square root	0.99	0.3258
Leaf mass (g)	9.07	189	4.41	16.69	12.28	2.79	square root	0.99	0.0459
PAI (m^2/m^2)	0.91	186	0.25	1.62	1.37	5.46	square root	0.98	0.0172
Panicle emergence (days after sowing)	39.17	210	29.00	49.00	20.00	0.69		0.93	0.0000
Panicle mass (g)	20.12	190	2.88	35.19	32.31	11.23	square root	0.99	0.4337
Reproductive to vegetative mass ratio	1.20	187	0.33	1.52	1.19	3.59	square root	0.93	0.0000
Stem mass (g)	14.22	191	6.87	22.49	15.62	2.27	square root	0.99	0.1684
Tiller height (mm)	359.68	187	113.67	721.67	608.00	5.35		0.99	0.1354
Tiller number (count)	1.81	187	1.26	2.69	1.43	1.14	cube root	0.99	0.0802
Total mass (g)	26.46	187	9.14	43.13	33.99	3.72	square root	0.99	0.5196
Vegetative mass (g)	16.92	188	8.44	28.01	19.57	2.32	square root	0.99	0.2685

Supplemental Table 2.2: Summary of QTL results. Marker name, location, proportion of genotypic variance explained, and relative additive effect for QTL identified for 13 measured traits at a 0.05 detection threshold are reported.

Trait	Marker	Chromosome	Position (cM)	LOD	Proportion of variance	Additive relative effect
Branch number	S1_36617026	1	84.01	6.18	8.9	-0.08
Branch number	S3_10844641	3	53.4	4.43	6.23	-0.07
Branch number	S5_7622386	5	44.09	5.38	7.67	-0.08
Branch number	S6_32411928	6	68.73	3.91	5.45	0.07
Branch number	S7_18218515	7	43.93	3.94	5.51	-0.07
Branch number	S9_6501061	9	33.94	3.74	5.21	-0.07
Branch number	S9_51926088	9	140.72	8.53	12.72	-0.1
Clump spread	S2_1368736	2	4.37	4.33	6.26	-0.03
Clump spread	S2_3532599	2	18	6.16	9.13	-0.04
Clump spread	S2_46536006	2	112.82	4.63	6.71	-0.02
Clump spread	S3_18761486	3	68.28	8.2	12.51	-0.03
Clump spread	S5_1722371	5	17.26	3.96	5.69	-0.02
Culm height	S2_37820883	2	70.03	7.21	13.12	0.06
Culm height	S5_42085155	5	100.66	3.99	6.92	-0.04
Culm height	S6_1367337	6	10.03	5.07	8.95	0.04
Culm height	S9_6295446	9	33.94	4.27	7.45	0.04
Culm height	S9_48859174	9	131.48	4.81	8.45	0.05
Leaf mass	S1_31298551	1	66.87	3.82	4.45	0.06
Leaf mass	S2_37965908	2	71.12	16.1	22.35	0.14
Leaf mass	S3_47360417	3	106.7	5.13	6.08	0.06
Leaf mass	S5_34517974	5	83.88	12.33	16.2	0.1
Leaf mass	S6_2365280	6	17.58	5.61	6.7	0.07
Leaf mass	S8_2959300	8	35.91	4.46	5.23	0.06
Leaf mass	S9_6724364	9	34.93	9.93	12.6	0.1
PAI	S2_37987785	2	71.12	10.94	18.47	0.13
PAI	S5_34517974	5	83.88	12.62	21.87	0.13
PAI	S6_2365280	6	17.58	4.73	7.27	0.08
PAI	S8_6974146	8	42.4	6.74	10.67	0.09
PAI	S9_6724364	9	34.93	4.27	6.52	0.08
Panicle emergence	S2_43829684	2	92.82	5.46	11.63	0.03

Supplemental Table 2.2: (cont.)

Panicle emergence	S7_32133319	7	99.94	5.13	10.87	0.04
Panicle mass	S2_41096419	2	80.96	5.79	12.09	0.1
Panicle mass	S5_34517974	5	83.88	5.22	10.83	0.09
Panicle mass	S7_32133319	7	99.94	6.27	13.19	-0.15
Reproductive to vegetative mass ratio	S5_4501200	5	34.5	5.22	8.49	0.05
Reproductive to vegetative mass ratio	S5_41999990	5	100.41	8.16	13.85	0.07
Reproductive to vegetative mass ratio	S6_7525462	6	40.63	7.76	13.08	-0.08
Reproductive to vegetative mass ratio	S7_32133319	7	99.94	7.18	12.01	-0.09
Second tiller height	S2_37820883	2	70.03	6.96	13.24	0.12
Second tiller height	S5_32800961	5	79.01	4.39	8.05	0.09
Second tiller height	S5_42113193	5	100.9	5.31	9.87	-0.1
Second tiller height	S6_1682903	6	12.47	5.59	10.43	0.09
Second tiller height	S9_6724364	9	34.93	4.46	8.19	0.09
Stem mass	S2_37820883	2	70.03	9.15	18.11	0.11
Stem mass	S5_29574617	5	69.56	4.39	8.12	0.06
Stem mass	S6_2516340	6	18.48	7.39	14.27	0.09
Total mass	S2_37820883	2	70.03	5.89	12.47	0.1
Total mass	S5_29574617	5	69.56	6.47	13.8	0.09
Total mass	S6_2516340	6	18.48	4.38	9.07	0.08
Vegetative mass	S2_37820883	2	70.03	11.56	22.02	0.12
Vegetative mass	S5_33682130	5	82.15	5.83	10.22	0.07
Vegetative mass	S6_2516340	6	18.48	7.77	14.01	0.09
Vegetative mass	S9_6724364	9	34.93	3.34	5.65	0.06

REFERENCES

Anderson, CM (1964) Studies of the Woodland Light Climate: I. The Photographic Computation of Light Conditions. Br Ecol Soc **52**:27-41

Araus JL, Cairns JE (2014) Field high-throughput phenotyping: The new crop breeding frontier. Trends Plant Sci **19**: 52–61

Bennetzen JL, Schmutz J, Wang H, Percifield R, Hawkins J, Pontaroli AC, Estep M, Feng L, Vaughn JN, Grimwood J, et al (2012) Reference genome sequence of the model plant Setaria. Nat Biotechnol **30**: 555–61

Broman KW, Wu H, Sen Ś, Churchill GA (2003) R/qtl: QTL mapping in experimental crosses. Bioinformatics **19**: 889–890

Brutnell TP, Wang L, Swartwood K, Goldschmidt A, Jackson D, Zhu X-G, Kellogg E, Van Eck J (2010) Setaria viridis: a model for C4 photosynthesis. Plant Cell **22**: 2537–2544

Busemeyer L, Ruckelshausen A, Möller K, Melchinger AE, Alheit K V, Maurer HP, Hahn V, Weissmann E a, Reif JC, Würschum T (2013) Precision phenotyping of biomass accumulation in triticale reveals temporal genetic patterns of regulation. Sci Rep **3**: 2442

Casa AM, Pressoir G, Brown PJ, Mitchell SE, Rooney WL, Tuinstra MR, Franks CD, Kresovich S (2008) Community resources and strategies for association mapping in Sorghum. Crop Sci **48**: 30–40

Casadesús J, Villegas D (2014) Conventional digital cameras as a tool for assessing leaf area index and biomass for cereal breeding. J Integr Plant Biol **56**: 7–14

Doust AN, Kellogg EA, Devos KM, Bennetzen JL (2009) Foxtail Millet : A Sequence-Driven Grass Model System. Plant Phys **149**: 137–141

Dupuis J, Siegmund D (1999) Statistical methods for mapping quantitative trait loci from a dense set of markers. Genetics **151**: 373–386

Feldman MJ, Paul RE, Banan D, Barrett JF, Sebastian J, Yee M, Jiang H, Lipka AE, Brutnell TP, José R, et al (2017) Time dependent genetic analysis links field and controlled environment phenotypes in the model C4 grass Setaria. PloS Genetics **13:** 1-31

Fernandez MGS, Bao Y, Tang L, Schable PS (2017) A High-Throughput, Field-Based Phenotyping Technology for Tall Biomass Crops. Plant Phys **174**: 2008-2022

Fiorani F, Schurr U (2013) Future Scenarios for Plant Phenotyping. Annu Rev Plant Biol **64**: 267–291

Furbank RT, Tester M (2011) Phenomics - technologies to relieve the phenotyping bottleneck. Trends Plant Sci **16**: 635–644

Gitelson AA, Viña A, Arkebauer TJ, Rundquist DC, Keydan G, Leavitt B (2003) Remote estimation of leaf area index and green leaf biomass in maize canopies. Geophys Res Lett **30**: 1248–1252

He J, Zhao X, Laroche A, Lu Z-X, Liu H, Li Z (2014) Genotyping-by-sequencing (GBS), an ultimate marker-assisted selection (MAS) tool to accelerate plant breeding. Front Plant Sci. doi: 10.3389/fpls.2014.00484

Hudiburg TW, Wang W, Khanna M, Long SP, Dwivedi P, Parton WJ, Hartman M, Delucia EH (2016) Impacts of a 32-billion-gallon bioenergy landscape on land and fossil fuel use in the US. Nat Energy **1**: 1–7

Lander ES, Botstein S (1989) Mapping mendelian factors underlying quantitative traits using RFLP linkage maps. Genetics **121**: 185–199

Li P, Brutnell TP (2011) Setaria viridis and Setaria italica, model genetic systems for the Panicoid grasses. J Exp Bot **62**: 3031–3037

Li XM, He ZH, Xiao YG, Xia XC, Trethowan R, Wang HJ, Chen XM (2015) QTL mapping for leaf senescence-related traits in common wheat under limited and full irrigation. Euphytica **203**: 569–582

Des Marais DL, Hernandez KM, Juenger TE (2013) Genotype-by-environment interaction and plasticity: exploring genomic responses of plants to the abiotic environment. Annu Rev Ecol Evol Syst **44**: 5–29

Mauro-Herrera M, Doust AN (2016) Development and Genetic Control of Plant Architecture and Biomass in the Panicoid Grass, Setaria. PLoS One **11**: e0151346

Mccormick RF, Truong SK, Mullet JE (2016) 3D sorghum reconstructions from depth images enable identification of quantitative trait loci regulating plant architecture. Plant Phys **172:** 823-834

Morrell PL, Buckler ES, Ross-Ibarra J (2011) Crop genomics: advances and applications. Nat Rev Genet **13**: 85–96

Myles S, Peiffer J, Brown PJ, Ersoz ES, Zhang Z, Costich DE, Buckler ES (2009) Association mapping: critical considerations shift from genotyping to experimental design. Plant Cell **21**: 2194–2202

Neumann HH, Hartog G Den, Shaw RH (1989) Leaf area measurements based on hemispheric photographs and leaf-litter collection in a deciduous forest during autumn leaf-fall. Agric For Meteorol **45**: 325–345

Parent B, Shahinnia F, Maphosa L, Berger B, Rabie H, Chalmers K, Kovalchuk A, Langridge P, Fleury D (2015) Combining field performance with controlled environment plant imaging to identify the genetic control of growth and transpiration underlying yield response to water-deficit stress in wheat. J Exp Bot **66**: 5481–5492

Pauli D, Andrade-sanchez P, Carmo-silva AE, Gazave E, French AN, Heun J, Hunsaker DJ, Lipka AE, Setter TL, Strand RJ, et al (2016) Field-Based High-Throughput Plant Phenotyping Reveals the Temporal Patterns of Quantitative Trait Loci Associated with Stress-Responsive Traits in Cotton. G3 **6**: 865–879

Poland J a, Rife TW (2012) Genotyping-by-Sequencing for Plant Breeding and Genetics. Plant Genome **5**: 92–102

Ray DK, Mueller ND, West PC, Foley JA (2013) Yield Trends Are Insufficient to Double Global Crop Production by 2050. PLoS ONE **8:** 0066428

Rich PM (1990) Characterizing plant canopies with hemispherical photographs. Remote Sens Rev **5**: 13–29

Somerville C, Long SP (2015) Energy, the environment, and climate change. Natl Acad Sci **45**: 32–40

Tanger P, Klassen S, Mojica JP, Lovell JT, Moyers BT, Baraoidan M, Naredo MEB, Mcnally KL, Poland J, Bush DR, et al (2017) Field-based high throughput phenotyping rapidly identifies genomic regions controlling yield components in rice. Nat Publ Gr **7:** 42839

Tilman D, Balzer C, Hill J, Befort B (2011) Global food demand and the sustainable intensification of agriculture. Proc Natl Acad Sci **108**: 20260–20264

Topp CN, Iyer-Pascuzzi AS, Anderson JT, Lee C-R, Zurek PR, Symonova O, Zheng Y, Bucksch A, Mileyko Y, Galkovskyi T, et al (2013) 3D phenotyping and quantitative trait locus mapping identify core regions of the rice genome controlling root architecture. Proc Natl Acad Sci **110**: 1695–1704

Vergara-díaz O, Zaman-allah MA, Masuka B, Hornero A (2016) A Novel Remote Sensing Approach for Prediction of Maize Yield Under Different Conditions of Nitrogen Fertilization. **7**: 1–13

White JW, Andrade-Sanchez P, Gore MA, Bronson KF, Coffelt TA, Conley MM, Feldmann KA, French AN, Heun JT, Hunsaker DJ, et al (2012) Field-based phenomics for plant genetics research. F Crop Res **133**: 101–1

CHAPTER 3
PHYSIOLOGICAL PLASTICITY THROUGH LEAF ROLLING AS A MEANS TO CONSERVE WATER AND MAINTAIN GROWTH OVER LONGER PERIODS IN A C_4 GRASS UNDER DROUGHT STRESS IN THE FIELD

ABSTRACT

As a mechanism for temporarily reducing leaf area under periods of high evaporative demand and low water supply, leaf rolling has been considered as a potential trait for improving the drought tolerance of many grass crops. However, the literature shows a mixture of results with regards to the effectiveness of leaf rolling in protecting yield from drought. Relative to common C_3 cereals such as rice, C_4 crops are understudied with regards to the impact of leaf rolling on protecting biomass production from drought stress. Here we use a combination of leaf cross sections, canopy hemispherical imaging, and visual leaf rolling scores in the field to show that leaf rolling has the potential to improve drought tolerance in S*etaria viridis*. Leaf rolling in *Setaria viridis* was a reversible behavior characterized by midday folding and elevation of leaf blade angle which reduced canopy radiation interception by 11 % on average. A visual leaf rolling score adapted from the rice literature was effective in capturing the diversity in leaf rolling phenotype across a North American *Setaria viridis* accession panel. Accessions that exhibited the highest degree of leaf rolling tended to be larger and flower later than their closest, non-rolling relatives while still maintaining an equivalent level of biomass productivity resistance to water-deficit treatment. These results suggest that leaf rolling in *Setaria viridis* is an effective means to reversibly reduce evaporative demand and conserve water while prolonging growth through drought conditions.

INTRODUCTION

To maintain yield gains despite climate extremes and variability, crop breeding must optimize plant stress responses. Drought, the mismatch between plant evaporative demand and soil moisture supply, is expected to become more widespread and intense in coming decades (Dai, 2011; Wang et al., 2014). Elevated temperature often accompanies drought and together these stresses reduce crop production and have profound economic and societal impacts (Lobell and Tebaldi, 2014; Lesk et al., 2016). Although irrigation may help dampen drought and temperature stress effects, this is not a realistic management strategy to apply broadly to

otherwise rainfed areas (Troy et al., 2015). Drought can manifest with variable timing and duration, which makes both forecasting of environmental conditions and breeding for suitably tolerant crop varieties difficult (Passioura, 2007; Dai, 2011). Leaf rolling, the reversible reduction of apparent leaf area, is an attractive and flexible trait for improving drought stress response without sacrificing yield potential in economically important food and fuel grasses. Due to the highly variable nature of drought stress and the wide diversity of grasses, effective implementation of leaf rolling as a drought tolerance trait requires confirmation of its potential adaptive significance in target germplasm.

Leaf rolling in grasses is driven by intercostally distributed bulliform cells which act as osmotic motors to temporarily alter the architecture of the leaf lamina depending on a plant's water status. A loss of bulliform cell turgor pressure causes the leaf margins to fold or curl towards each other and reduces apparent leaf area (Jane and Chiang, 1990). Due to the shell structure of the grass leaf blade, folding is accompanied with a longitudinal change in leaf shape which forces the leaf to angle upright (Moulia, 2000). This process is reversed when the bulliform cells regain turgor pressure and return the leaf lamina to a fuller exposed surface area. Leaf rolling initiation occurs at a range of water potentials and varies among species and cultivars (Begg, 1980; O'toole and Cruz, 1980; Wright and Smith, 1983; Turner et al., 1986). Typically the most negative leaf water potentials are observed around midday when evaporative demand is also at its highest (Kadioglu, 2007). This is reflected in the diurnal trend of leaf rolling, with leaves open and relaxed in the morning and severely rolled in the afternoon. However, in cases of extreme, terminal drought conditions or cultivar-specific drought sensitivity, leaf rolling may exhibit a progressive pattern with leaf rolling severity increasing over timescales of multiple days (O'toole and Cruz, 1980).

Rolled leaves have an altered energy budget due to lowered radiation interception and therefore lowered leaf temperature (Redmann, 1985). This reduced temperature results in a reduced leaf-to-air vapor pressure deficit which in turn decreases transpiration and conserves water (O'Toole and Cruz, 1979; Turner et al., 1986; Matthews et al. 1990; Heckathorn and DeLucia, 1991). The reduction in radiation interception and leaf temperature also serves to protect the leaf from photoinhibition associated with drought stress (Corlett et al., 1994; Feng et al., 2002; Saglam et al., 2014). Rolled leaves have reduced net photosynthesis and transpiration,

but leaf rolling in rice affects transpiration more strongly than CO2 assimilation, making rolled leaves more water use efficient compared to manually unrolled leaves (Dingkuhn et al., 1989).

Leaf rolling has historically been suggested as a screening tool for drought tolerance in major rice breeding programs (Loresto et al., 1976) and great effort has gone towards characterizing the physiology and diversity of leaf rolling in rice. However, subsequent experiments in rice have shown cases where leaf rolling gave no benefit to dry matter accumulation in drought (Turner et al., 1986) leading to a general consensus that leaf rolling is more so a sign of drought sensitivity rather than tolerance in rice. It should be noted that rice is a predominantly wetland adapted crop and dryland conditions have different ecological considerations. Furthermore, rice utilizes the C_3 pathway of photosynthesis. Due to their carbon concentrating machinery (i.e. Kranz anatomy), leaf rolling as a drought response may take on different nuances in C_4 grasses compared to C_3 grasses such as rice. A number of undomesticated C_4 grasses that exhibit leaf rolling are known to thrive in conditions much drier than the typical rice production environment (Heckathorn and DeLucia, 1991; Vergara et al., 2015) and this inconsistent pattern in the wider leaf rolling literature warrants further investigation into the trait's adaptive significance.

Although they are inherently water use efficient and have a photosynthetic advantage under well-watered conditions, C_4 grasses are sensitive to severe water-deficits and can have slower recovery times compared to co-occurring C_3 grasses (Ripley et al., 2010). By avoiding photoinhibition, leaf rolling may stave off these deficiencies under drought stress.

Leaf rolling can alter whole plant hydraulic conductance by limiting transpiration in a dynamic and non-committal fashion (Sinclair et al., 2017). By decreasing transpiration leaf rolling serves to limit hydraulic conductance but does not involve the permanent loss in leaf area and photosynthetic potential associated with reduced leaf expansion or increased leaf senescence (Devi et al., 2015). When vapor pressure deficit is at its peak, leaf rolling can limit transpiration which in turn conserve soil water supply (Matthews et al., 1990). This is seen in the life strategy that an undomesticated tropical C_4 forage grass, *Brachiaria spp.,* takes in response to drought conditions; water conservation via leaf rolling until more favorable conditions return (Vergara et al., 2015). Leaf rolling associated reductions in evaporative demand and transpiration address both the supply (inadequate soil water) and demand (increased vapor pressure deficit) aspects of drought stress.

Various metrics for leaf rolling appear in the literature. They include tracking leaf rolling progression after excision (O'toole and Cruz, 1980; Price et al., 1997), evaluating the curvature of leaf cross sections (Sirault et al., 2015), and visual scores (IRRI, 1996). Recently, remote sensing technologies such as repeated measures of normalized difference of vegetation index (NDVI) and below-canopy hemispherical imaging have been adapted to evaluate leaf rolling at the canopy level and suggest potential for improved collection throughput and resolution (Lu et al., 2011; Baret et al., 2018; Henry et al., 2019). Repeated image capture can characterize the temporal dynamic of leaf rolling and determine whether or not it is part of a reversible stress response. Hemispherical imaging has the added benefits of providing an in situ estimate of canopy radiation use and aboveground biomass productivity (Banan et al., 2018).

Efforts to uncover the genetics of leaf rolling have been primarily focused on rice. Mapping experiments have identified numerous loci related to leaf rolling using both rice recombinant inbred line populations and accession panels (O'Toole and Moya, 1978; Price et al., 1997; Courtois et al., 2000; Henry et al., 2019). Genes that modulate leaf rolling act by altering bulliform cell and schlerenchyma development (Xu et al., 2009; Zou et al., 2011; Xiang et al., 2012; Zhang et al., 2015). Overlap between loci for leaf rolling and root morphology (Courtois et al., 2000) and genes that alter both leaf rolling and xylem development (Zhang et al., 2018) suggests genetic coordination between leaf rolling and other drought response traits in rice. Comparatively less work has been done in C_4 crops such as maize and sorghum, with studies evaluating leaf rolling variation using only a small set of genotypes (Blum et al., 1989; Matthews et al., 1990; Agata and Saneoka, 1996; Baret et al., 2018).

Despite their economic and ecological significance, efforts to understand the physiology and genetics of leaf rolling in C_4 grasses are thus far limited. Maize and sorghum are important cereal crops while perennial grasses such as switchgrass and miscanthus are potential next generation cellulosic biofuel feedstocks (Tilman et al., 2011). To avoid taking arable acreage away from food production, next generation feedstocks must be grown on marginal and possibly water-limited land. Leaf rolling as a limit to transpiration has the potential to improve the drought stress response of already highly water use efficient C_4 grasses.

Setaria viridis (L.) Beauv. is a convenient model system to study the stress responses of C4 grasses. This widely distributed species has a small stature, fast life cycle, diploid genome, broad phenotypic diversity, and high drought tolerance (Li and Brutnell, 2011). *Setaria viridis*

uses the NADP-ME C4 photosynthesis pathway; similar to maize, sorghum, sugarcane, and miscanthus (Brutnell et al., 2010). Experiments both in the field and in controlled environments have shown *Setaria viridis* to be an effective model both in a variety of contexts (Feldman et al., 2017). Genetic resources including a reference genome sequence (Bennetzen et al., 2012) and natural populations representing diverse germplasm collected from wide geographic distributions (Huang et al., 2014; Schröder et al., 2016) are available. Natural populations contain extensive phenotypic and genetic variation that is not confounded by human domestication efforts. Previous work characterizing localized North American *Setaria viridis* adaptations to stress have thus far only focused on herbicide tolerance and there is great need to examine its abiotic response potential (Douglas et al., 1985). Given that *Setaria viridis* has an inherently high drought tolerance and occupies a wide range of geographies with varied environmental factors, there is likely great opportunity to take advantage of its attempts at local adaptation and introgress this wild variation into domesticated stock to produce more drought tolerant food and fuel crops (Huang et al., 2014).

The present study evaluated leaf rolling responses to water limitation in 207 North American *Setaria viridis* accessions grown in the field during a serendipitous period of intense, sustained mid-season heat between July 20-24, 2016 (39-43 days after sowing). The combination of natural diversity, field imposed treatment conditions, and prevailing background environmental conditions provided suitable circumstances to ask the following about leaf rolling: (1) What are the architectural and temporal characteristics of *Setaria viridis* leaf rolling responses to water deficit and to what degree does leaf rolling alter the radiation use of the canopy? (2) Can a visual score effectively capture leaf and canopy components of leaf rolling and survey variation in a genetically diverse population? (3) Does leaf rolling represent adaptation or sensitivity to water deficit?

RESULTS

Leaf rolling in Setaria viridis is a reversible diurnal adjustment of leaf and canopy architecture in response to drought stress

Leaf and canopy adjustment were measured in 15 *Setaria viridis* accessions to characterize the genotypic variability of leaf rolling in response to water availability. The 15 accessions were selected to represent the range of diversity in both leaf rolling severity and aboveground architecture found in North American *Setaria viridis*. Leaf blade roll angle (the

cross-sectional angle between leaf margins and midrib), leaf blade inclination angle (the angle between the leaf blade and the stem), the proportion of photosynthetic photon flux density (PPFD) penetrating the canopy (canopy light penetration, CLP), plant area index (PAI), and a visual canopy level leaf rolling score (scaled 0-3; 0 indicating no rolling, 3 indicating severe rolling) were measured 41 days after sowing (DAS) at dawn and midday in both well-watered and water-stressed treatments. 41 DAS corresponded with a period in which the majority of accessions had already exhibited panicle emergence and a period that was forecast to have sustained high temperatures (Supplemental Figure 3.1).

At dawn in both treatments, all leaves appeared to be unrolled and at equivalent inclination angles (Figure 3.1 A, B). At midday, leaf roll angle was significantly (p-value < 0.001) reduced, i.e. more tightly rolled, by 32% in water-deficit plants. Leaf roll angle for water-deficit plants measured at midday was also significantly (p-value < 0.001) reduced compared to well-watered planted measured at both dawn and midday. However, in well-watered plants leaf roll angle did not significantly ($p > 0.05$) change over time (Figure 3.1 A). Leaf inclination angle was 10 degrees steeper, i.e. leaves were more upright, in water-deficit plants measured at midday compared to well-watered plants measured at midday (Figure 3.1 B, p-value < 0.05). Assessed as an overall population, PAI and CLP were not significantly different between well-watered and water-deficit treatments (Figure 3.1 C, D). There was also substantial genotypic variation in the magnitude and direction of responses of leaf and canopy architecture over the course of the day in well-watered and water-deficit conditions.

To determine the degree of diurnal adjustment in leaf and canopy architecture within individual accessions, traits were calculated as the ratio at midday relative to dawn (midday:dawn). Calculating diurnal adjustment in this fashion maintained the distribution of the data. The ratio of all leaf and canopy traits at midday relative to dawn was significantly different between drought treatments (Figure 3.1 E-H, p-values < 0.01). The ratio of leaf roll angle at midday relative to dawn was lower in water-deficit plants than in well-watered plants, indicating that leaves became more tightly folded at midday in response to drought stress while remaining open under well-watered conditions. The difference in leaf inclination angle midday:dawn ratio showed that leaves became more upright at midday in water-deficit plants and more relaxed in well-watered plants. The ratios of PAI at midday relative to dawn were greater in well-watered plants than in water-deficit plants, indicating that well-watered plants had a fuller canopy area at

midday than water deficit plants. Conversely, ratios of PAI at midday relative to dawn were greater in water-deficit plants than in well-watered plants, indicating that a greater proportion of light passed through the canopy at midday than at dawn in response to water deficit. Because dawn measurement were collected the day after midday measurements, it can be demonstrated that leaf rolling is a reversible diurnal movement for *Setaria viridis* grown under this level of water and temperature stress.

The correlation of leaf and canopy diurnal adjustments were used to demonstrate the degree to which changes at the leaf level scaled up to reduce the display of leaf area and reduce absorption of radiation (Figure 3.2). The ratio of leaf roll angle at midday relative to dawn was positively correlated with the ratio of PAI at midday relative to dawn in water-deficit plants (Figure 3.2 E, $r = 0.52$, p-value < 0.05) and negatively correlated with ratio of CLP at midday relative to dawn in water deficit plants (Figure 3.2 C, $r = -0.55$, p-value < 0.05). PAI and CLP midday:dawn ratios were negatively correlated with each other in both treatments (Figure 3.2 B, $r = -0.78$ p-value < 0.001). The ratio of leaf inclination angle at midday relative to dawn under water-deficit was not significantly correlated with the water-deficit midday:dawn ratio for any other trait. The correlation between the ratio of leaf roll angle at midday relative to dawn and the ratios for PAI and CLP at midday relative to dawn suggests that diurnal adjustments in leaf architecture scale up to diurnal adjustments in canopy architecture and light environment.

Leaf roll scores (LRS) greater than zero were only observed in water-deficit canopies at midday. LRS was negatively correlated with the ratio of leaf roll angle at midday relative to dawn under water deficit (Figure 3.3 A, $r^2 = 0.51$, p-value < 0.01), negatively correlated with the ratio of PAI at midday relative to dawn under water-deficit (Figure 3.3 D, $r^2 = 0.34$, p-value < 0.05), and positively correlated with the ratio of CLP at midday relative to dawn under water-deficit (Figure 3.3 C, $r^2 = 0.47$, p-value < 0.01). The correlation between LRS and leaf and canopy diurnal adjustments suggests that a visual canopy level score effectively captures the diurnal changes in leaf architecture, canopy leaf area, and canopy light penetration associated with leaf rolling and is an appropriate method for quickly screening a *Setaria viridis* population for leaf rolling diversity.

Leaf rolling correlation with mid-season aboveground productivity responses to water deficit

To determine the correlation between leaf rolling and whole plant responses to drought stress, leaf rolling was compared to mid-season biomass productivity responses to water availability. Mid-season biomass productivity was estimated using PAI generated from hemispherical images collected at dawn and a drought response was calculated between treatments (water-deficit/well-watered). Loss of biomass production to water-deficit, as estimated from dawn hemispherical imagery, was negatively correlated with the ratio of leaf roll angle at midday relative to dawn under water deficit (Figure 3.4 A, $r^2 = 0.45$, p-value < 0.01). The loss of biomass production to water deficit was positively correlated with both the change in CLP from dawn to midday (Figure 3.4 B, $r^2 = 0.27$, p-value < 0.05) and leaf rolling score assessed at midday (Figure 3.4 C, $r^2 = 0.48$, p-value < 0.01) under water-deficit.

Leaf rolling and end-of-season productivity across North American accession panel

Leaf rolling score (LRS) was evaluated across a panel of 207 North American *Setaria viridis* accessions on 41 DAS. LRS demonstrated a non-normal distribution with 39 % of the population exhibiting no leaf rolling, 61 % exhibiting some degree of rolling, and 8 % exhibiting a LRS ≥ 2.0 (Supplemental Figure 3.2). The distribution of LRS did not overlap with the clustering of accessions as determined by their single nucleotide polymorphism (SNP) distances (Supplemental Figure 3.3). These SNP distances were used to identify the accessions with a LRS ≤ 0.5 that were most closely related to each of the accession with a LRS ≥ 2.0 and used for subsequent analysis comparing high rolling and low-to-non rolling accessions with similar genetic backgrounds (Supplemental Figure 3.4; Supplemental Table 3.1).

The relation between leaf rolling and plant productivity responses to drought stress was assessed using aboveground vegetative biomass measurements from the end of season destructive harvest and height and tiller count measurements taken both in the field and from the end of season destructive harvest. Across the population, accessions with a LRS = 2.0 produced more vegetative biomass under water-deficit than accessions with a LRS ≤ 0.5 (Figure 3.5 A, Tukey's pairwise comparison test). Additionally, accessions with a LRS ≥ 2.0 had vegetative biomass values greater than the bottom 36^{th} percentile of the entire population regardless of leaf rolling severity. The vegetative biomass under water-deficit of accessions with a LRS ≥ 2.0 and

their closest relatives, as identified by SNP distances, with a LRS ≤ 0.5 are highlighted in Figure 5 A relative to the entire accession panel.

Vegetative biomass under water-deficit was significantly (p-value < 0.001) larger for accessions with a LRS ≥ 2.0 than it was for closely related accessions with a LRS ≤ 0.5 (Figure 3.5 B). The magnitudes of the difference in vegetative biomass under water-deficit between individual accessions with a LRS ≥ 2.0 and closely related accessions with a LRS ≤ 0.5 was highly variable (Figure 3.5 C).

The response of culm height and vegetative mass measured at harvest to drought stress (WD/WW) was not significantly different between accessions with a LRS ≥ 2.0 and closely related accessions with a LRS ≤ 0.5 (Figure 3.5 D; Supplemental Figure 3.5).

Culm height and tiller number were not significantly different between accessions with a LRS ≥ 2.0 and closely related accessions with a LRS ≤ 0.5 when measured early in the season (31 DAS) (Figure 3.6 A, D). However, both culm height and tiller number were significantly larger in accessions with a LRS ≥ 2.0 compared to closely related accession with a LRS ≤ 0.5 when measured at the destructive harvest (Figure 3.6 B, E; p-value > 0.01). The magnitudes of the difference in culm height and tiller number between individual accession with a LRS ≥ 2.0 and closely related accessions with a LRS ≤ 0.5 was close to zero when measured at mid-season in the field and highly variable when measured at the end of season destructive harvest (Figure 3.6 C, F).

Accessions with a LRS ≥ 2.0 had a significantly (p-value < 0.001) later panicle emergence date than closely related accession with a LRS ≤ 0.5 (Supplemental Figure 3.6 A). The magnitudes of the difference in panicle emergence DAS under water-deficit between individual accessions with a LRS ≥ 2.0 and closely related accessions with a LRS ≤ 0.5 was highly variable (Supplemental Figure 3.6 B).

DISCUSSION

The combination of leaf and canopy level measurements of leaf rolling and their relation to aboveground productivity presented here provides evidence which suggests that leaf rolling in C4 grasses is a beneficial adaptation rather than a product of compounding stress. Leaf rolling in *Setaria viridis* was characterized by a reversible diurnal folding of the leaf blade which increased canopy light penetration by 11 % on average. A visual score adapted from the rice literature was an appropriate means of capturing leaf and canopy level aspects of leaf rolling and was used for

a coarse survey of population level diversity. Plants with more tightly rolled leaves and a greater proportion of light penetration through the canopy lost less mid-season biomass to drought stress than plants without leaf rolling and an unaltered canopy light environment. Although accessions that exhibited severe leaf rolling experienced drought stress for a longer duration than closely related non-rolling accessions, severely rolled accessions lost a similar proportion of biomass compared to non-rolling accessions and were still productive under water deficit.

What are the architectural and temporal characteristics of leaf rolling responses to water-deficit and to what degree does leaf rolling alter the radiation use of the canopy?

In response to water-deficit, leaves became more folded and upright at midday while the apparent leaf area of the canopy decreased and a greater proportion of light penetrated through the canopy (Figure 3.1 E-F). These changes in leaf and canopy architecture were fully reversed at dawn.

Midday changes in leaf roll angle under water-deficit were significantly (Figure 3.2 C, $r = -0.55$, p-value < 0.05) correlated with changes in canopy light penetration and reduced the radiation use of the canopy by an average of 11 % (Figure 3.1 H). By reducing their apparent leaf area and thermal load, the most vulnerable leaves in the upper canopy transpire less and avoid photoinhibition. At the same time, this allows light to penetrate more deeply into the canopy where lower leaves can photosynthesize at an improved rate under more humid conditions if water supply is adequate (Truong et al., 2015).

The strong correspondence among leaf, canopy, and score observations provides a cohesive set of methods for evaluating leaf rolling in *Setaria viridis* at different scales and throughputs. In particular, the use of time-course below canopy hemispherical imaging offers a potentially high-throughput and high resolution complement to the traditional but coarser visual scoring method. We show that a minimal number (2) of hemispherical image timepoints is sufficient to generate a canopy-level leaf rolling value that correlates well (Figure 3.3 C, $r^2 = 0.47$, p-value < 0.01) with leaf rolling score and therefore can be used as an effective proxy, as suggested for maize (Baret et al., 2018).

For hemispherical imaging to truly replace a visual leaf rolling score at the population screening level, it needs to be adapted to some sort of autonomous rover such as that seen in Young 2018 (Young et al., 2018) Hemispherical imaging has the added benefit of providing an estimate of aboveground productivity that can replace destructive harvest (Banan 2018). Having

both a well-watered and a water-deficit treatment condition allows the added benefit of a simultaneous estimate of and correlation to in situ biomass productivity responses to stress generated from hemispherical images.

Leaf rolling associated changes in canopy area and light environment should be taken into account when timing the collection of hemispherical images as a proxy for productivity, especially when water supply is relevant. In the present study, diurnal percent differences of up to 20 % were observed for PAI. Dawn image collection corresponded with a canopy whose leaves were in a relaxed state and provided a more consistent measurement opportunity. Dawn PAI from hemispherical imaging is a measure of all the tissue contributing to aboveground biomass. Changes in PAI from dawn to midday are associated exclusively with changes in leaf display because leaves did not fall off the plant due to senescence within that time period and PAI rebounded the next morning (Figure 3.1).

Can a visual score effectively capture leaf and canopy components of leaf rolling and survey variation in a genetically diverse population?

The visual leaf rolling score was significantly correlated with diurnal changes in leaf roll angle, CLP, and PAI under water-deficit (Figure 3.3) and proved to be an effective method for quickly surveying the entire accession panel for leaf rolling severity (Supplemental Figure 3.2). Leaf rolling score and the SNP distances between accessions was used to find closely related severely rolling and non-rolling pairs for further investigation (Supplemental Figure 3.3).

The lack of a detectable genetic signature for leaf rolling in this experiment could be attributed to (1) an insufficient amount of stress experienced at the time leaf rolling was measured, or (2) the visual leaf rolling score used did not have the resolution needed to parse apart genotypic variation. Future experiments should improve sensor and time resolution by taking advantage of advances in high-throughput hemispherical imaging. Additionally, given the inherent hardiness of *Setaria viridis*, a more severe or longer period of water-deficit may be warranted.

To emphasize genotypic variation related to leaf rolling, a recombinant inbred line population could be derived from parental accessions exhibiting contrasting severities of leaf rolling. The set of accessions with a LRS ≥ 2 and the corresponding closely related accessions with a LRS ≤ 0.5 provides potential pairings to produce a recombinant inbred line (RIL) population that maximizes variation in leaf rolling (Supplemental Table 3.1). This approach

combined with higher resolution phenotyping and a more severe water-deficit treatment may reveal genotype-to-phenotype associations related to leaf rolling.

Does leaf rolling represent adaptation or sensitivity to water deficit?

The mid-season productivity response to water-deficit reflects plant stress performance in the moment and its positive correlation with leaf rolling score (Figure 3.4 C, $r^2 = 0.48$, p-value < 0.01) is consistent with there being an adaptive benefit to leaf rolling in the plant's vegetative growth stage. End of season biomass is important agronomically, however, it may also reflect the compounding effects of the plant's life cycle experience--including accumulated stress interactions--and produces a noisier representation of plant performance. Leaf rolling measurements and estimates of mid-season productivity were collected during a period of sustained and elevated temperature that coincided with the period just after peak panicle emergence across the population (Supplemental Figure 3.1). This serendipitous timing allows us to hone in on leaf rolling interactions with mid-season productivity and lessens the influence that phenology might have on plant performance in response to water-deficit at the time of leaf rolling measurement collection.

Accessions with severe leaf rolling (LRS ≥ 2) had more end of season productivity under water-deficit and later panicle emergence dates than closely related accessions that exhibited little to no leaf rolling (LRS ≤ 0.5) (Figure 3.5 B; Figure 3.6 B, E). This is consistent with observations in rice in which taller genotypes tend to have higher leaf rolling scores (Dingkhun et al., 1989, 1999). Despite their larger potential evaporative demand and more time spent experiencing drought stress, accessions with severe leaf rolling lost the same proportion of vegetative biomass and culm height to drought stress (evaluated as WD/WW) compared to closely related accessions with little to no leaf rolling (Figure 3.5 D, Supplemental Figure 3.5).

Determining whether leaf rolling is an adaptation to drought stress or a sign of sensitivity requires an evaluation of the environmental and life history context. Environmental data shows that although water demand (P-PET) was high throughout the season, decreases in soil moisture supply (volumetric water content) were not apparent until later in the experiment (Supplemental Figure 3.1). In the present study, the positive impacts of leaf rolling on productivity responses to drought stress were most apparent mid-season (41 DAS) when hemispherical images were collected. This suggests that water demand played an important role in driving leaf rolling. In an

attempted follow up experiment phenotyper platform, leaf rolling was not observed despite severe water withholding resulting growth impairment; likely because the controlled environment did not establish enough vapor pressure deficit to generate the necessary water demand.

It is difficult to predict what sort of phenotype would result from different combinations of treatment severity and various phylogenetic backgrounds and this may account for the mixture of findings seen in the literature. For any given species or locally adapted accession, there is likely an optimum range within which leaf rolling is most beneficial. The results presented here are consistent with leaf rolling as an adaptive trait for *Setaria viridis* accessions that delay their transition to reproductive development, prolong their growth, and therefore need to conserve water through periods of moderate and potentially variable drought stress defined by high levels of evaporative demand.

METHODS

Experimental design

The experiment, from seed sowing to final destructive biomass harvest, ran from June 11th to August 24th, 2016. The experiment was a randomized complete block design replicated twice with two water treatments (well-watered and water-limited) and 208 *Setaria* genotypes.

A panel of 207 *Setaria viridis* accessions collected from across North America were obtained from the Donald Danforth Plant Science Center, St Louis, MO. *Setaria italica* B100 was used as check plot material planted throughout the experimental plots.

Seeds were germinated in glasshouse and transplanted by hand into a mechanically tilled field seven days after sowing. The field site was the South Farms of the University of Illinois Urbana-Champaign and is rain-fed, tile-drained, and has a deep, organically rich, Flanagan/Drummer series type soil.

Plants were arranged in 0.3 m by 0.25 m plots each containing 30 plants with 5 cm grid spacing housed under retractable awning rain-out shelters which diverted precipitation from both well-watered and drought plots (Gray et al., 2016). Drip irrigation was applied to well-watered plots and irrigation was withheld from water-limited plots after transplant establishment. Soil volumetric water content was measured three times weekly using a capacitance probe inserted into access tubes installed in Setaria italica B100 check plots distributed throughout the

experimental plots following the procedure detailed in Markelz et al 2011 (Diviner 2000, Sentek Sensor Technologies; Markelz et al., 2011).

Climate conditions

Over the duration of the field experiment, the average air temperature was 24 ^{o}C and the average relative humidity was 76 %. Climate conditions were monitored at weather station how far from the field site operated by the Illinois State Water Survey (ISWS).

Canopy hemispherical imaging

Canopy hemispherical images were collected to generate estimates of Plant Area Index (PAI) and Canopy Light Penetration (CLP). Images were collected using a GoPro Hero 3+ digital camera customized with a 1.39 mm 190^{o} hemispherical lens and triggered with a hand-held remote (GoPro Hero 3+, GoPro Inc, San Mateo, CA, USA; 1.39 mm hemispherical lens, Quality Video Components LLC, Sparta, MI, USA). The camera was manually placed in the center of each plot with a consistent cardinal direction and oriented upward with the aid of a bull's-eye level. A light-box constructed from a PVC frame and sheer fabric with outer dimensions of 0.35 * 0.3 * 0.5 m was placed over the subject plot during the imaging process to create a diffuse light environment and exclude imaging artifacts from the rain-out shelters, neighboring plots, and the afternoon sun's orb. Images were classified using ImageJ (ImageJ, National Institutes of Health, Bethesda, MD, USA) and analyzed using HemiView (Delta-T Devices Ltd, Cambridge, UK) to estimate GSF and PAI.

Leaf rolling measurements

Leaf inclination angle and leaf transverse folding angle were measured on a subset of 15 genotypes at dawn and midday on the second mature leaf down from the shoot apex on three representative plants per plot in a single replicate 41 days after sowing. The 15 genotypes were selected for their variation in degree of leaf rolling and overall aboveground architecture. Leaf inclination angle was measured as the angle between leaf blade and stem with a protractor. Leaf transverse folding angle was measure by taking a transverse cross section midway down the length of the blade. The cut end of the excised leaf blade was dipped in stamp ink and pressed onto printer paper. The adaxial angle between leaf margins and midrib was measured in ImageJ (NIH).

A visual leaf rolling score scaled between 0-3, 0 indicating no rolling and 3 indicating severe rolling was assessed across the entire population 41 days after sowing. This scale was

adapted from a standardized evaluation system developed at the International Rice Research Institute for screening rice populations (IRRI, 1996).

Destructive harvest

Destructive harvest was initiated on a per plot basis 30 days after panicle emergence observation. The same three plants evaluated for in-field culm height and tiller number were cut at the base and separated into leaf, stem and reproductive tissues. The separated tissues were dried at 65 ^{o}C and stem tissue was laid in the drying oven such that the overall architecture was kept intact. Culm height was measured as the length from the base of the plant to the collar of the flag leaf on the first emerged tiller. The dried leaf, stem, and reproductive tissues were weighed on a digital mass balance.

Data analysis and visualization

The following R packages were used for data analysis and visualization: *lsmeans, ggplot2, cor.test, t.test*

Hierarchical clustering and contrasting accession selection

A genetic map was generated from 1316 single nucleotide polymorphisms (SNP) selected for their location in a non-transcribed sequence, presence in all samples, having a major allele frequency > 0.3, and having a distribution of one SNP every 100 kb evenly tiled across genome.

The SNP distance matrix was generated using *dist()*. Clustering and cophenetic distances were generated using *hclust()*. A set of closest non-rolling relatives was selected on the basis of their having a LRS $\leq$ 0.5, complete culm height, tiller number, and vegetative mass data, and having minimum cophenetic distance with an accession with a LRS $\geq$ 2.0. In cases where multiple non-rolling accessions met these criteria, phenotypic values were averaged across the tied non-rolling accessions (Supplemental Table 3.1).

FIGURES AND TABLE

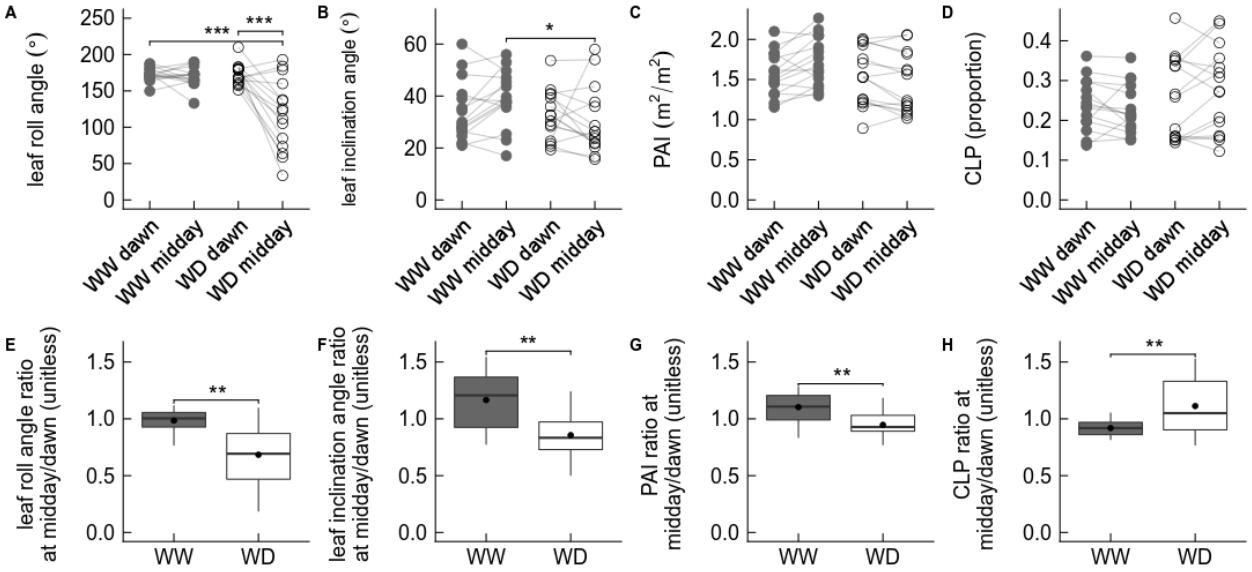

Figure 3.1: Reaction norms and box plots of leaf and canopy diurnal adjustments (Figure 3.1 A-D) Individual accession reaction norms. Points represent accession averages within each trait-time-treatment combination. Lines connect accession timepoints within treatment. Grey points represent well-watered observations; open points represent water-deficit observations. Stars indicate p-values from two-way ANOVA and Tukey Honest Significant Differences: ns > 0.05, * < 0.05, ** <0.01, *** < 0.001
(Figure 3.1 E-H) Box plots of diurnal adjustment expressed as midday:dawn ratios. Points indicate treatment means. Grey boxes represent well-watered observations; white boxes represent water-deficit observations. Stars indicate p-values from Welch's two sample t-test: ns > 0.05, * < 0.05, ** <0.01, *** < 0.001
WW: well-watered; WD: water-deficit; PAI: plant area index; CLP: canopy light penetration

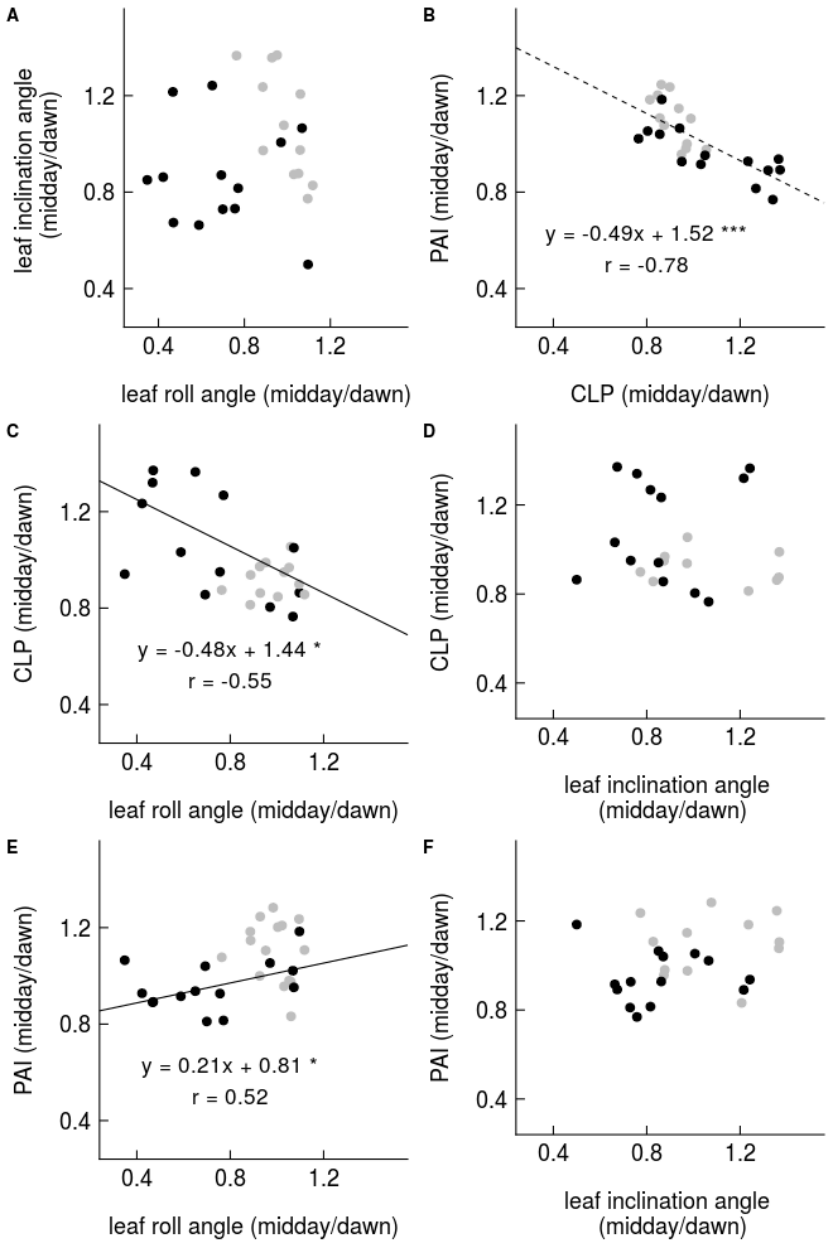

Figure 3.2: Correlation across leaf and canopy diurnal adjustments
(Figure 3.2 A-F) Correlation of leaf and canopy diurnal adjustments. Grey points represent well-watered observations; black points represent water-deficit observations. Solid black lines represent linear regression for water-deficit observations; dashed line represents linear regression for both well-watered and water-deficit observations together. Pearson's correlation coefficients are reported for significant relationships (p-value < 0.05). Stars indicate p-values from Pearson's test: ns > 0.05, * < 0.05, ** <0.01, *** < 0.001
PAI: plant area index; CLP: canopy light penetration

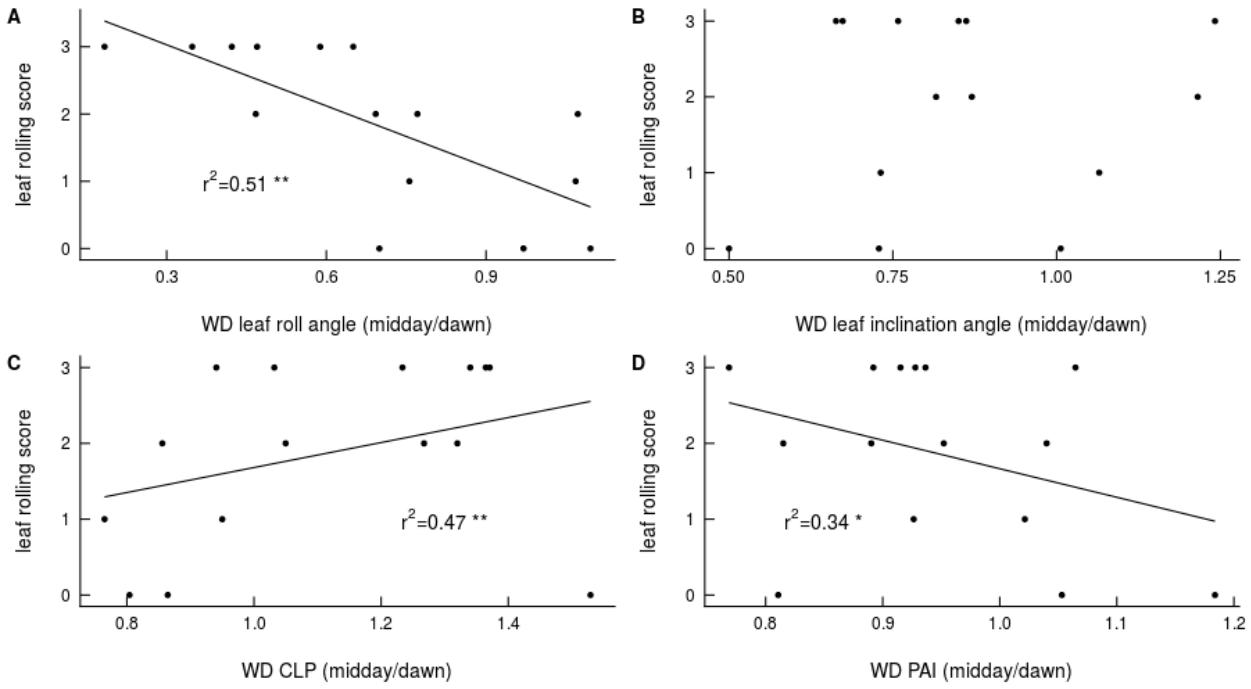

Figure 3.3: Leaf rolling score correlation with diurnal leaf and canopy adjustments
(Figure 3.3 A-D) Midday leaf rolling score correlations with leaf and canopy diurnal adjustments under water-deficit conditions. Coefficients of determination (r-squared) are reported for significant relationships. Stars indicate p-values from Pearson's test: ns > 0.05, * < 0.05, ** <0.01, *** < 0.001
WW: well-watered; WD: water-deficit; PAI: plant area index; CLP: canopy light penetration

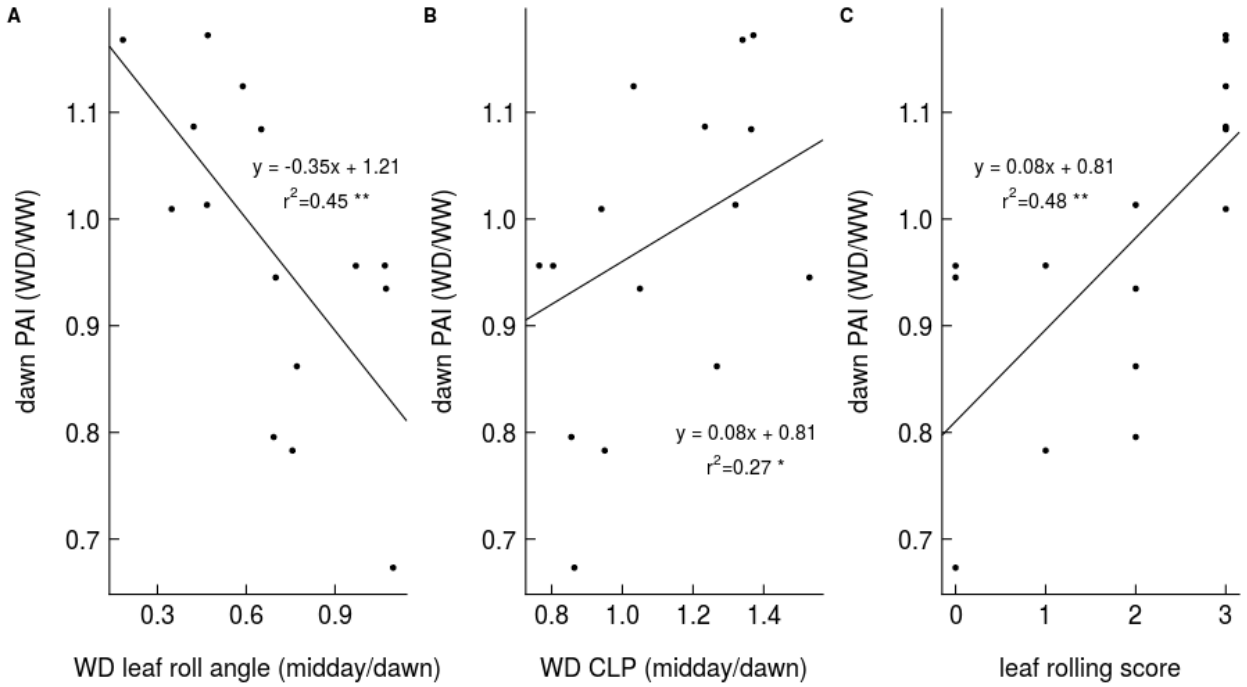

Figure 3.4: Dawn PAI treatment response correlation with leaf and canopy diurnal adjustment

(Figure 3.4 A-C) Dawn PAI treatment response (WD/WW) correlation with leaf and canopy diurnal adjustment. Coefficients of determination (r-squared) are reported for significant relationships. Stars indicate p-values from Pearson's test: ns > 0.05, * < 0.05, ** <0.01, *** < 0.001

WW: well-watered; WD: water-deficit; PAI: plant area index; CLP: canopy light penetration

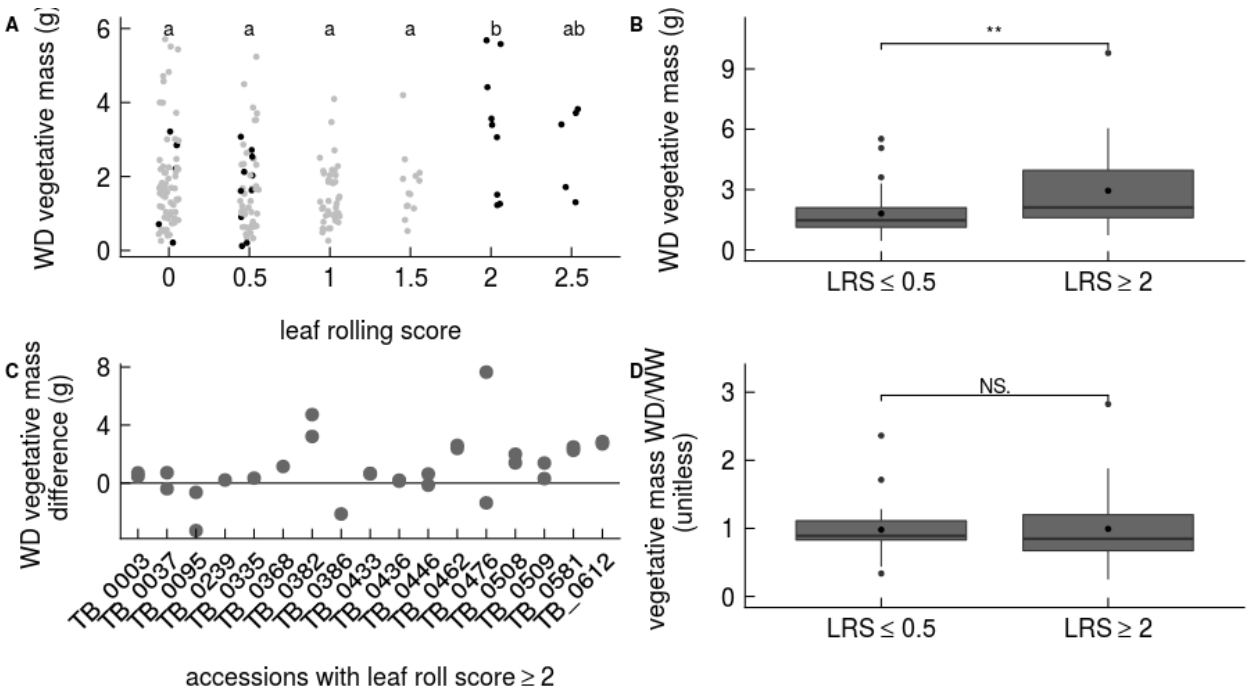

Figure 3.5: Accessions that display severe leaf rolling are larger and more productive under water deficit than their non-rolling counterparts

(Figure 3.5 A) Aboveground vegetative biomass under water-deficit measured at end of season destructive harvest as a function of midday leaf rolling score across entire accession panel. Points represent accession values averaged across both replicates. Black points represent accessions with a leaf rolling score ≥ 2 and their closest relative with a leaf rolling score ≤ 0.5 as identified by minimum SNP cophenetic distance. All other accession observations are represented by grey points. Letters indicate groupings based on Tukey adjusted pairwise multiple comparisons of least-square means using a 95% confidence interval.

(Figure 3.5 B) Box plots comparing vegetative biomass under water-deficit between accessions with a leaf rolling score ≥ 2 and their closest relatives with a leaf rolling score ≤ 0.5.

(Figure 3.5 C) Difference in vegetative biomass under water-deficit between each accession with a leaf rolling score ≥ 2 and their closest relative with a leaf rolling score ≤ 0.5 for each replicate. Accessions with a leaf rolling score ≥ 2 are displayed on the horizontal axis.

(Figure 3.5 D) Box plots comparing vegetative biomass response to drought stress (WD/WW) between accessions with a leaf rolling score ≥ 2 and their closest relatives with a leaf rolling score ≤ 0.5.

Stars indicate p-values from Welch's two sample t-test: NS. > 0.05, * < 0.05, ** <0.01, *** < 0.001

WW: well-watered; WD: water-deficit; LRS: leaf rolling score

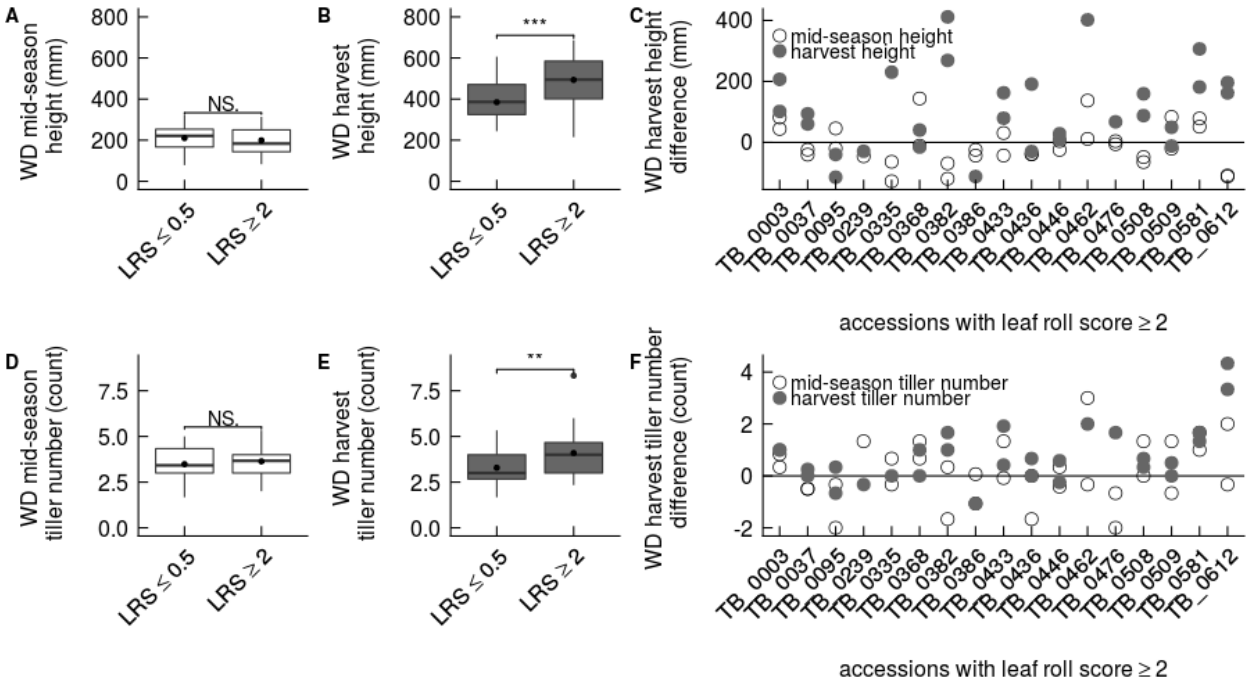

Figure 3.6: Although they are similar early in growth, high rolling accessions have greater final productivity under water-deficit and produce more and taller tillers compared to closely related low-to-non rolling accessions

(Figure 3.6 A, D) Box plots of culm height (A) and tiller number (D) measured at 41 DAS in the field under water-deficit comparing accessions with a leaf rolling score ≥ 2 to accessions with a leaf rolling score ≤ 0.5.

(Figure 3.6 B, E) Box plots of culm height (B) and tiller number (E) measured at end of season destructive harvest under water-deficit comparing accessions with a leaf rolling score ≥ 2 to accessions with a leaf rolling score ≤ 0.5.

(Figure 3.6 C, F) Differences in culm height (C) and tiller number (F) measured at 41 DAS in the field (open points) and at end of season destructive harvest (grey points) under water-deficit between each accession with a leaf rolling score ≥ 2 and their closest relative with a leaf rolling score ≤ 0.5 for each replicate. Accessions with a leaf rolling score ≥ 2 are displayed on the horizontal axis.

Stars indicate p-values from Welch's two sample t-test: NS. > 0.05, * < 0.05, ** <0.01, *** < 0.001

WD: water-deficit; LRS: leaf rolling score

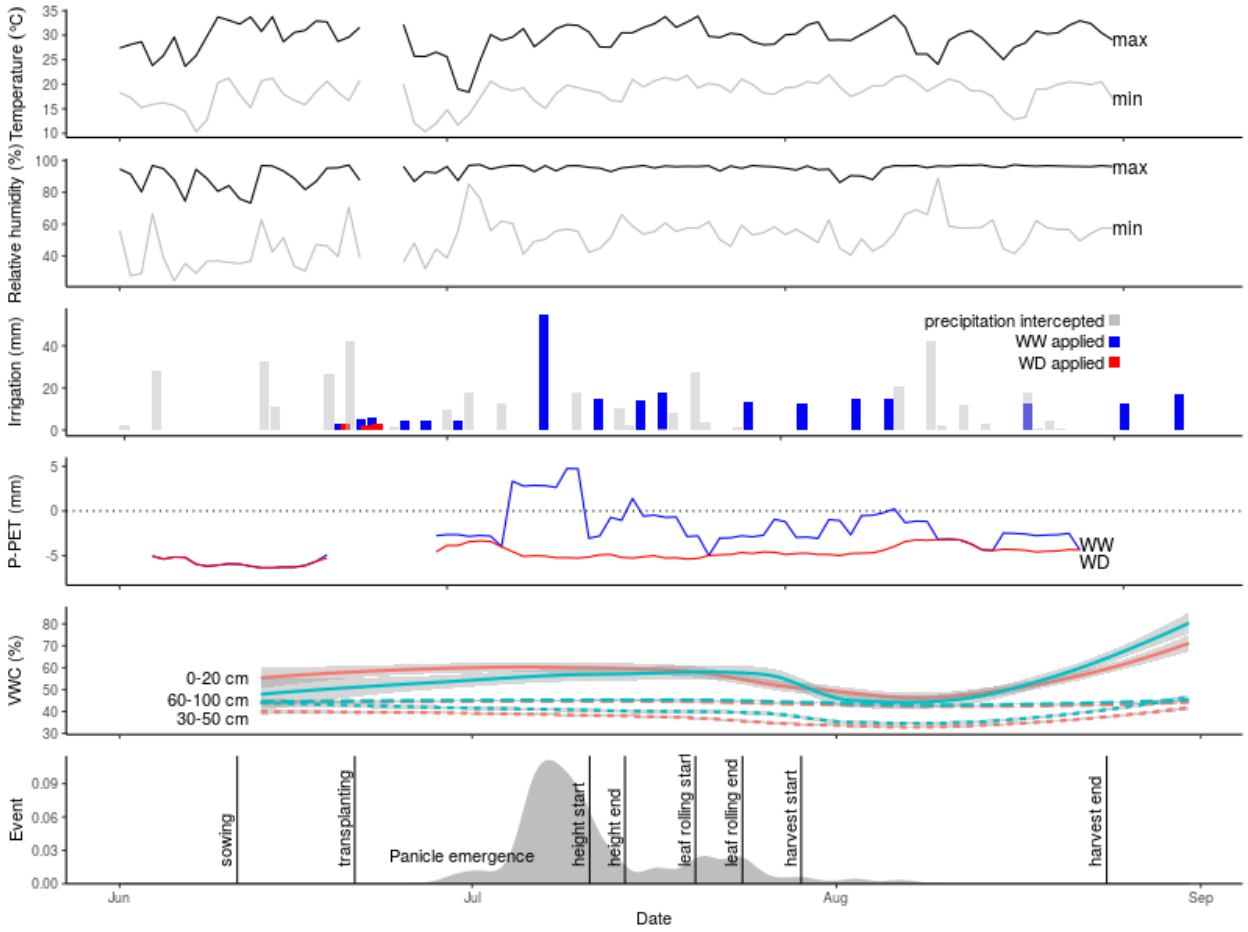

Supplemental Figure 3.1: Experimental timeline and environmental conditions
Summary of environmental conditions and experimental timeline. Temperature, humidity, precipitation, and potential evapotranspiration data downloaded from Illinois State Water Survey archive. Gaps reflect missing archive data. Precipitation minus potential evapotranspiration (P-PET) calculated on a seven day running average using either precipitation intercepted (ambient, grey line) or irrigation applied (well-watered, WW, blue line; water-deficit, WD, red line). Volumetric water content (VWC) displayed as smoothed LOESS functions across treatments and three depth horizons: 0-20 cm (solid lines), 30-50 cm (small dashed lines), and 60-100 cm (large dashed lines); well-watered (blue), water-deficit (red).

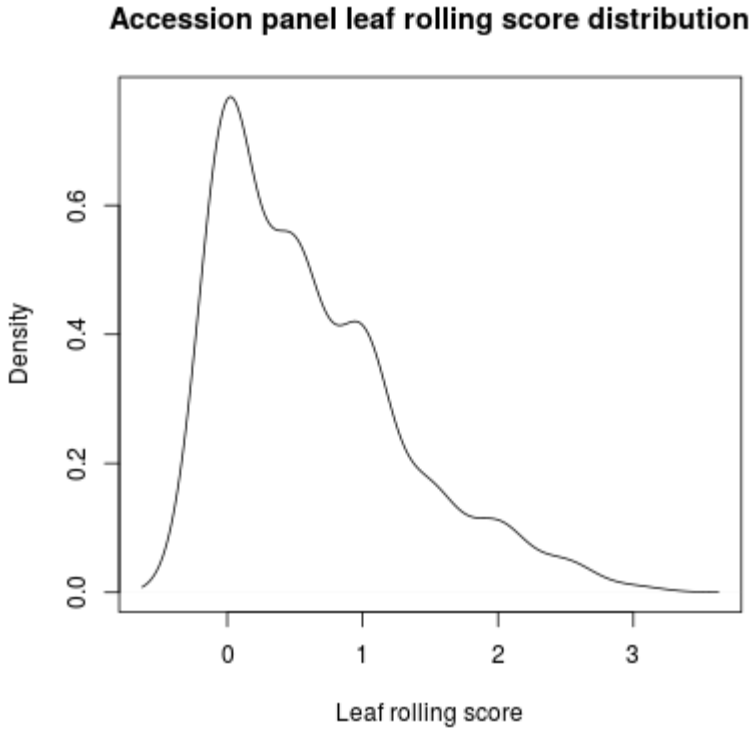

Supplemental Figure 3.2: Leaf rolling score distribution
Leaf rolling score distribution across North American *Setaria viridis* accession panel.

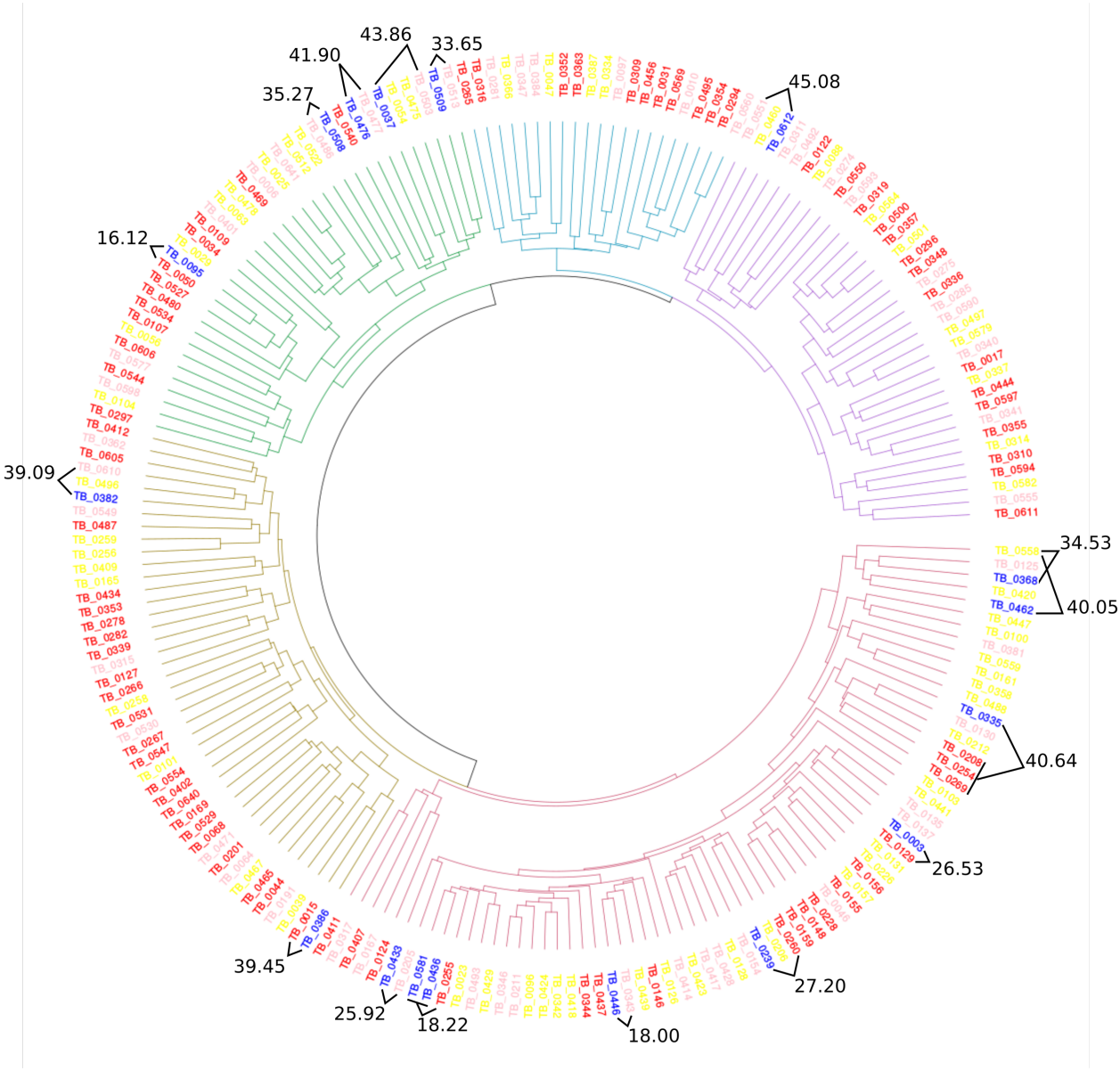

Supplemental Figure 3.3: Dendrogram of accession relatedness from SNP distances. Dendrogram generated from accession SNP distances. Branch color differentiates five major population clusters. Accession label color represents leaf rolling score: red = 0, pink = 0.5, yellow = 1-1.5, blue ≥ 2. Brackets connect accession with leaf rolling score ≥ 2 to their closest "sibling" accession with leaf rolling score ≤ 0.5. Bracket label displays cophenetic distance between siblings used to assess whole plant performance across leaf rolling severity contrasts.

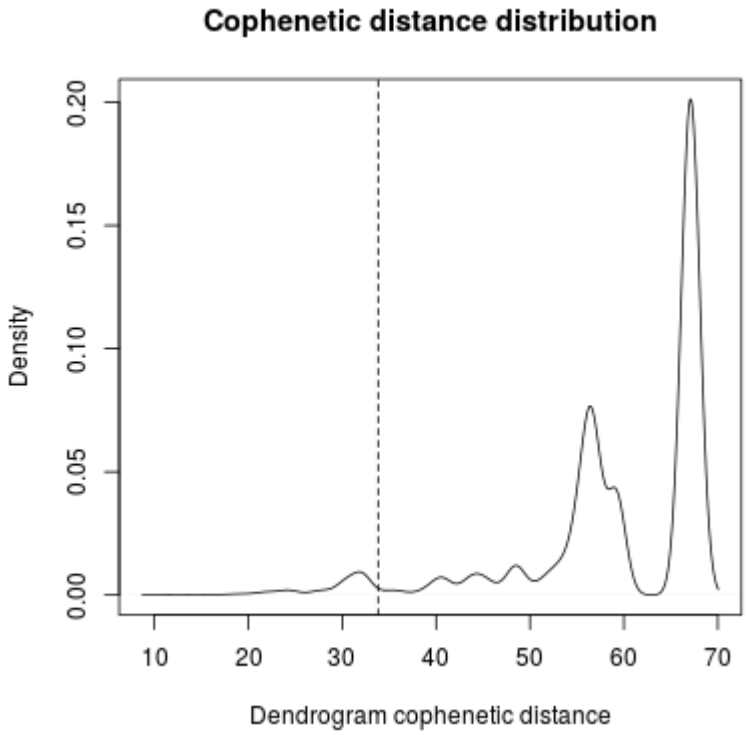

Supplemental Figure 3.4: Density distribution of cophenetic distances between accessions based on dendrogram generated from SNP matrix. Solid line represents the distribution of cophenetic distances between all potential genotype pairs within the North American *Setaria viridis* accession panel. The vertical dashed line represents the average cophenetic distance between accessions with a LRS ≥ 2 and their most closely related accession with a LRS ≤ 0.5.

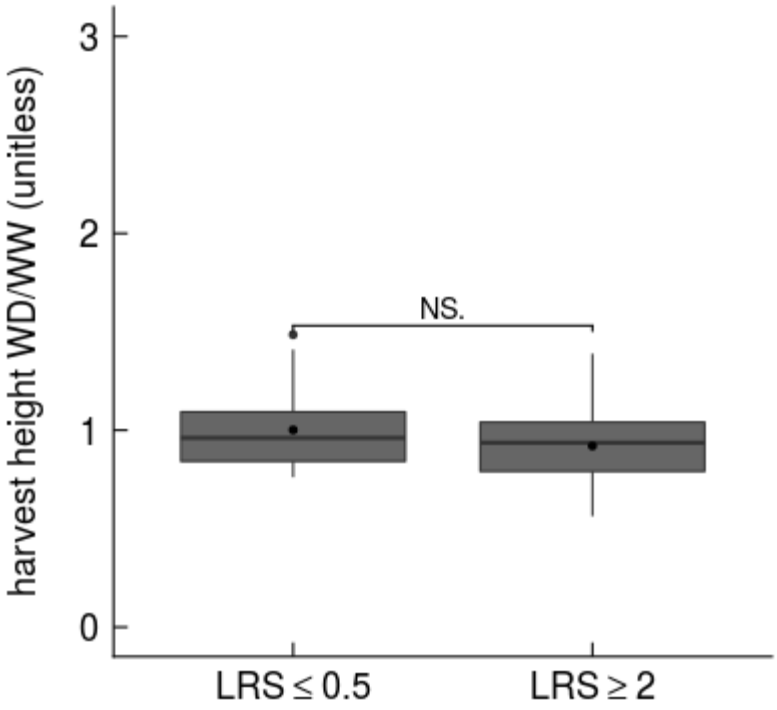

Supplemental Figure 3.5: End-of-season culm height response to drought stress as a function of leaf rolling score.
Box plots comparing harvest culm height response to drought stress (WD/WW) between accessions with a leaf rolling score ≥ 2 and their closest relatives with a leaf rolling score ≤ 0.5. Stars indicate p-values from Welch's two sample t-test: NS. > 0.05, * < 0.05, ** <0.01, *** < 0.001
WW: well-watered; WD: water-deficit; LRS: leaf rolling score

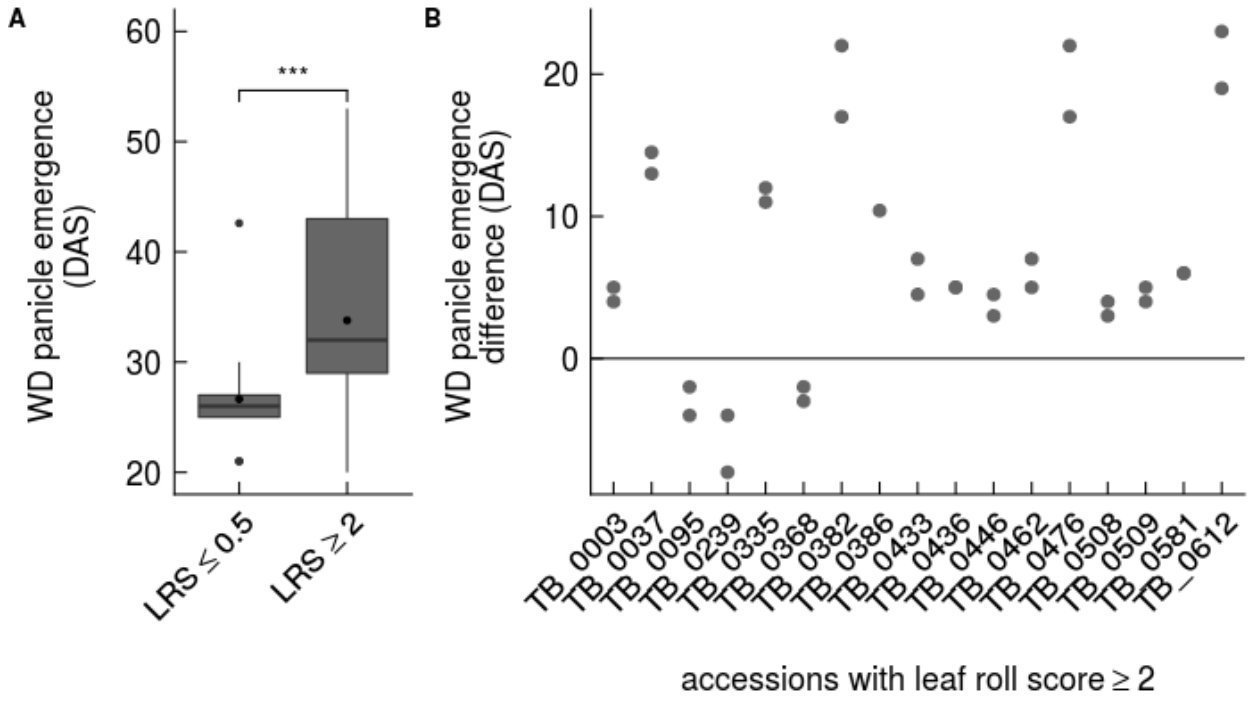

Supplemental Figure 3.6: High rolling accessions have a later panicle emergence date than their low-to-non rolling closest relatives

(Supplemental Figure 3.6 A) Box plots comparing panicle emergence dates under water-deficit between accessions with a leaf rolling score ≥ 2 and their closest relatives with a leaf rolling score ≤ 0.5.

(Supplemental Figure 3.6 B) Difference in panicle emergence date under water-deficit between each accession with a leaf rolling score ≥ 2 and their closest relative with a leaf rolling score ≤ 0.5 for each replicate. Accessions with a leaf rolling score ≥ 2 are displayed on the horizontal axis.

Stars indicate p-values from Welch's two sample t-test: NS. > 0.05, * < 0.05, ** <0.01, *** < 0.001

WW: well-watered; WD: water-deficit; LRS: leaf rolling score

Supplemental Table 3.1: Accessions with a LRS ≥ 2 and the most closely related accession(s) with a LRS = 0.5 as determined by their cophenetic distance. These pairing were used to compare productivity responses to stress between closely related rolling and non-to-low rolling accessions. In cases where multiple accessions with LRS =< 0.5 had the same cophenetic distance, phenotypic values were averaged.

Accessions with LRS ≥ 2	**Accessions with LRS ≤ 0.5**	**Cophenetic distance**
TB_0003	TB_0135	27.57
	TB_0137	27.57
TB_0037	TB_0503	43.86
	TB_0513	43.86
TB_0095	TB_0050	16.12
TB_0239	TB_0260	27.20
TB_0335	TB_0130	37.95
TB_0368	TB_0125	34.53
TB_0382	TB_0610	39.09
TB_0386	TB_0064	47.16
	TB_0191	47.16
	TB_0201	47.16
	TB_0471	47.16
	TB_0529	47.16
TB_0433	TB_0211	27.64
	TB_0344	27.64
	TB_0437	27.64
	TB_0493	27.64
TB_0436	TB_0493	19.70
TB_0446	TB_0493	24.33
	TB_0211	24.33
	TB_0344	24.33
	TB_0437	24.33
TB_0462	TB_0125	40.05
TB_0476	TB_0477	41.90
TB_0508	TB_0486	35.27
TB_0509	TB_0513	33.65
TB_0581	TB_0493	19.70
TB_0612	TB_0551	45.08

REFERENCES

Agata W, Saneoka H (1996) Cultivar Differences in Dry Matter Production and Leaf Water Relations in Water-stressed Maize. Japanese Journal of Grasslands. **41:** 294-301

Banan D, Paul RE, Feldman MJ, Holmes MW, Schlake H, Baxter I, Jiang H, Leakey ADB (2018) High-fidelity detection of crop biomass quantitative trait loci from low-cost imaging in the field. 1-8 DOI: 10.1002/pld3.41

Baret F, Madec S, Irfan K, Lopez J, Comar A, Hemmerlé M, Praud S, Tixier MH (2018) Leaf-rolling in maize crops: from leaf scoring to canopy-level measurements for phenotyping. **69**: 2705–2716

Bennetzen JL, Schmutz J, Wang H, Percifield R, Hawkins J, Pontaroli AC, Estep M, Feng L, Vaughn JN, Grimwood J, et al (2012) Reference genome sequence of the model plant Setaria. Nat Biotechnol **30**: 555–61

Blum A, Mayer J, Golan G (1989) Agronomic and physiological assessments of genotypic variation for drought resistance in sorghum. Aust J Agric Res **40**: 49–61

Botanical M, Press G (2016) Adaptation of Grasses to Water Stress-Leaf Rolling and Stomate Distribution Author (s): R. E. Redmann Source: Annals of the Missouri Botanical Garden, Vol. 72, No . 4 (1985), pp. 833-842 Published by: Missouri Botanical Garden Press Stable URL. **72**: 833–842

Brutnell TP, Wang L, Swartwood K, Goldschmidt A, Jackson D, Zhu X-G, Kellogg E, Van Eck J (2010) Setaria viridis: a model for C4 photosynthesis. Plant Cell **22**: 2537–2544

Corlett JE, Jones HG, Massacci A, Masojidek J (1994) Water deficit, leaf rolling and susceptibility to photoinhibition in field grown sorghum. Physiol Plant **92**: 423–430

Courtois B, McLaren G, Sinha PK, Prasad K, Yadav R, Shen L (2000) Mapping QTLs associated with drought avoidance in upland rice. Mol Breed **6**: 55–66

Dai A (2011) Drought under global warming: A review. Wiley Interdiscip Rev Clim Chang **2**: 45–65

Devi MJ, Taliercio EW, Sinclair TR (2015) Leaf expansion of soybean subjected to high and low atmospheric vapour pressure deficits. J Exp Bot **66:** 1845-1850

Dingkuhn M, Cruz RT, O'Toole JC, Dörffling K (1989) Net photosynthesis, water use efficiency, leaf water potential and leaf rolling as affected by water deficit in tropical upland rice. Aust J Agric Res **40**: 1171–1181

Dingkuhn M, Audebert AY, Jones MP, Etienne K, Sow A (1999) Control of stomatal conductance and leaf rolling in *O. sativa* and *O. glaberrima* upland rice. Field Crops Research **61:** 223-236

Douglas BJ, Thomas AG, Morrison IN, Maw MG (1985) The biology of Canadian weeds. 70. *Setaria viridis* (L.) Beauv. Can J Plant Sci **65:** 669-690

Feldman MJ, Paul RE, Banan D, Barrett JF, Sebastian J, Dinneny R, Yee M, Jiang H, Lipka AE, Brutnell TP, et al (2017) Time dependent genetic analysis links field and controlled environment phenotypes in the model C 4 grass Setaria. PLoS Genet **13**: 1–31

Feng Y, Cao K, Feng Z (2002) Thermal dissipation, leaf rolling and inactivation of PSII reaction centres in Amomum villosum. 865–876

Gray SB, Dermody O, Klein SP, Locke AM, McGrath JM, Paul RE, Rosenthal DM, Ruiz-Vera, UM, Siebers MH, Strellner R, et al (2016) Intensifying drought eliminates the expected benefits of elevated carbon dioxide for soybean. Nature Plants **2:** 1-8

Heckathorn SA, DeLucia EH (1991) Effect of Leaf Rolling on Gas Exchange and Leaf Temperature of Andropogon gerardii and Spartina pectinata. Bot Gaz **152**: 263–268

Henry A, McNally KL, Luquet D, Sanciangco M, Torres RO, Rebolledo MC, Cal AJ (2019) Leaf morphology, rather than plant water status, underlies genetic variation of rice leaf rolling under drought. Plant Cell Environ. doi: 10.1111/pce.13514

Huang P, Feldman M, Schroder S, Bahri BA, Diao X, Zhi H, Estep M, Baxter I, Devos KM, Kellogg EA (2014) Population genetics of Setaria viridis, a new model system. Mol Ecol **23**: 4912–4925

IRRI (1996) Standard evaluation system for rice. 4th Edition, IRRI, The Philippines.

Jane WN, Chiang SHT (1990) Morphology and development of bulliform cells in *Arundo formosana* hack. Taiwania **36:** 85-96

Kadioglu A (2007) A Dehydration Avoidance Mechanism: Leaf Rolling. The Botanical Review **73**: 290–302

Lesk C, Rowhani P, Ramankutty N (2016) Influence of extreme weather disasters on global crop production. Nature **529**: 84–87

Li P, Brutnell TP (2011) Setaria viridis and Setaria italica, model genetic systems for the Panicoid grasses. J Exp Bot **62**: 3031–3037

Lobell DB, Tebaldi C (2014) Getting caught with our plants down: The risks of a global crop yield slowdown from climate trends in the next two decades. Environ Res Lett. doi: 10.1088/1748-9326/9/7/074003

Loresto GC, Chang TT, Tagumpay O (1976) Field evaluation and breeding for drought resistance. Philipp J Crop Sci **1**: 36–39 LA–English

Lu Y, Hao Z, Xie C, Crossa J, Araus JL, Gao S, Vivek BS, Magorokosho C, Mugo S, Makumbi D, et al (2011) Large-scale screening for maize drought resistance using multiple selection criteria evaluated under water-stressed and well-watered environments. F Crop Res **124**: 37–45

Markelz RJC, Strellner RS, Leakey ADB (2011) Impairment of C4 photosynthesis by drought is exacerbated by limiting nitrogen and ameliorated by elevated [CO2] in maize. J Exp Bot **62:** 3235-3246

Matthews RB, Azam-Ali SN, Peacock JM (1990) Response of four sorghum lines to mid-season drought. II. Leaf characteristics. F Crop Res **25**: 297–308

Moulia B (2000) Leaves as Shell Structures: Double Curvature, Auto-Stresses, and Minimal Mechanical Energy Constraints on Leaf Rolling in Grasses. J Plant Growth Regul **19**: 19–30

O'Toole JC, Moya TB (1978) Genotypic variation in maintenance of leaf water potential in rice. Crop Sci **18**: 873–876

O'toole JC, Cruz RT (1980) Response of Leaf Water Potential, Stomatal Resistance, and Leaf Rolling to Water Stress. Plant Physiol **65**: 428–432

Passioura J (2007) The drought environment: Physical, biological and agricultural perspectives. J Exp Bot **58**: 113–117

Price AH, Young EM, Tomos AD (1997) Quantitative trait loci associated with stomatal conductance, leaf rolling and heading date mapped in upland rice (Oryza sativa). New Phytol **137**: 83–91

Redmann RE (1985) Adaptation of grasses to water stress-leaf rolling and stomate distribution. Annals of the Missouri Botanical Garden **72:** 833-842

Ripley B, Frole K, Gilbert M (2010) Differences in drought sensitivities and photosynthetic limitations between co-occurring C3 and C4 (NADP-ME) Panicoid grasses. Ann Bot **105**: 493–503

Saglam A, Kadioglu A, Demiralay M, Terzi R (2014) Leaf rolling reduces photosynthetic loss in maize under severe drought. Acta Bot Croat **73**: 315–332

Schröder S, Bahri BA, Eudy DM, Layton DJ, Kellogg EA, Devos KM (2016) Genetic diversity and origin of North American green foxtail [Setaria viridis (L.) Beauv.] accessions. Genet Resour Crop Evol 1–12

Sinclair TR, Devi J, Shekoofa A, Choudhary S, Sadok W, Vadez V, Riar M, Rufty T (2017) Limited-transpiration response to high vapor pressure deficit in crop species. Plant Sci **260**: 109–118

Sirault XRR, Condon AG, Wood JT, Farquhar GD, Rebetzke GJ (2015) "Rolled-upness": Phenotyping leaf rolling in cereals using computer vision and functional data analysis approaches. Plant Methods **11**: 1–11

Tilman D, Balzer C, Hill J, Befort B (2011) Global food demand and the sustainable intensification of agriculture. Proc Natl Acad Sci **108:** 20260–20264

Troy TJ, Kipgen C, Pal I (2015) The impact of climate extremes and irrigation on US crop yields. Environ Res Lett. Doi: 10.1088/1748-9326/10/5/054013

Truong SK, McCormick RF, Rooney WL, Mullet JE (2015) Harnessing genetic variation in leaf angle to increase productivity of *Sorghum bicolor.* Genetics **201:** 1229-1238

Turner NC, O'Toole JC, Cruz RT, Namuco OS, Ahmad S (1986) Responses of seven diverse rice cultivars to water deficits I. Stress development, canopy temperature, leaf rolling and growth. F Crop Res **13**: 257–271

Vergara MF, Rao IM, Jiménez J de la C, Cardoso JA, Pineda M (2015) Contrasting strategies to cope with drought conditions by two tropical forage C 4 grasses. AoB Plants **7**: plv107

Wang Q, Wu J, Lei T, He B, Wu Z, Liu M, Mo X, Geng G, Li X, Zhou H, et al (2014) Temporal-spatial characteristics of severe drought events and their impact on agriculture on a global scale. Quat Int **349**: 10–21

Water and Atmospheric Resources Monitoring Program. Illinois Climate Network. (2015). Illinois State Water Survey, 2204 Griffith Drive, Champaign, IL 61820-7495. https://dx.doi.org/10.13012/J8MW2F2Q.

Wright GC, Smith RCG (1983) Differences between Two Grain Sorghum Genotypes in Adaptation to Drought Stress. Aust J Agric Res **34:** 637-651

Xiang JJ, Zhang GH, Qian Q, Xue HW (2012) SEMI-ROLLED LEAF1 Encodes a Putative Glycosylphosphatidylinositol-Anchored Protein and Modulates Rice Leaf Rolling by Regulating the Formation of Bulliform Cells. Plant Physiol **159**: 1488–1500

Xu Q, Xue HW, Qian Q, Zhu XD, Zhang GH (2009) SHALLOT-LIKE1 Is a KANADI Transcription Factor That Modulates Rice Leaf Rolling by Regulating Leaf Abaxial Cell Development. Plant Cell Online **21**: 719–735

Young SN, Kayacan E, Peschel JM (2018) Design and field evaluation of a ground robot for high-throughput phenotyping of energy sorghum. Precis Agric. doi: 10.1007/s11119-018-9601-6

Zhang J, Zhang H, Srivastava AK, Pan Y, Bai J, Fang J, Shi H, Zhu J-K (2018) Knock-down of rice microRNA166 confers drought resistance by causing leaf rolling and altering stem xylem development. Plant Physiol pp.01432.2017

Zhang JJ, Wu SY, Jiang L, Wang JL, Zhang X, Guo XP, Wu CY, Wan JM (2015) A detailed analysis of the leaf rolling mutant sll2 reveals complex nature in regulation of bulliform cell development in rice (Oryza sativa L.). Plant Biol **17**: 437–448

Zou L, Sun X, Zhang Z, Liu P, Wu J, Tian C, Qiu J, Lu T (2011) Leaf rolling controlled by the homeodomain leucine zipper class IV gene Roc5 in rice. Plant Physiol **156**: 1589–1602

CHAPTER 4
SUCCESSIVE INTERNODES AS A POSTMORTEM SIGNATURE OF ELONGATION RESPONSES TO DROUGHT

ABSTRACT

The effective implementation of next generation C_4 grass biofuel feedstocks requires improvements in productivity and stress resilience. Internodes, the primary support organ for elevating photosynthetic and reproductive organs, provide a specific developmental and anatomical target for improving stem growth. However, few studies have examined internode morphology within a whole-tiller context. Here we show that the model C_4 grass, *Setaria viridis,* is an ideal system for leveraging mapping populations and image-based phenotyping of field grown material and present evidence that internode development is an important aspect of abiotic stress response and life strategy. Reproductive internode elongation responded positively to water-deficit treatment while the elongation of the distal-most vegetative internode composed a larger proportion of overall height under water-deficit, together suggesting internode elongation as a means to recover lost height and maintain the elevation of reproductive organs. In a North American *Setaria viridis* accession panel, internode morphology was correlated with population structure as well as the geography and climate of accession provenance. The co-localization between genotype-to-phenotype associations detected for internode elongation and traits that describe height and bushiness suggest that internode elongation is an important driver of growth and aboveground architecture.

INTRODUCTION

As C_4 grass crops and biofuel feedstocks continue to play an outsized role in global agriculture, there is an urgent need to improve their productivity and abiotic stress resilience in order to meet and maintain projected demand. Products from these grasses come primarily from either grain (maize and sorghum) or stem feedstocks (energy sorghum, miscanthus, and switchgrass) that provide the raw material for biofuels and other industrial products. To avoid displacing food production and natural ecosystems while also reducing external inputs, these feedstocks must be able to produce satisfactory yields on marginal acreage that is potentially water limited. Optimizing aboveground architecture is a promising avenue to achieving that goal. Historical selection efforts have produced architectures typified by having a single or few tillers,

each composed of many internodes, which support fewer and larger panicles. Current improvement efforts rely on detecting genotype-to-phenotype associations for these traits of interest to produce the foundation for selection and modification. This has been an effective means of modifying stem growth to maximize grain production and minimize lodging in modern varieties. However, to produce the variety of stem architectures required to meet diverse feedstock demands, especially in unimproved C_4 grasses grown in marginal conditions, a more focused approach on the specific anatomical elements that produce stem growth is required.

The internode is the dominant structural element of the stem and influences resource capture and storage, neighbor competition, and reproductive success. Basal internode dimension is related to resistance to lodging. Internode number, length, and arrangement determine the vertical distribution of leaf area and can influence photosynthetic activity by altering canopy ventilation and light penetration (Guo, 2005; Monteith and Unsworth, 2013). As they grow and elongate, internodes act as sinks for assimilates and nutrients while mature internodes serve as reserves for grain filling (Kirby et al., 1994). Pollination and seed dispersal are heavily influenced by the height of the inflorescence or infructesence (Haase et al., 1995; Dorp and Daleboudt, 1996). The full height of the tiller composed of vegetative internodes and the reproductive internode, or peduncle, is responsible for determining the height of these reproductive organs.

Internode growth is a coordinated function of cell division, expansion, and maturation that occurs in synchrony with other elements of the phytomer and neighboring internodes. Development proceeds upward from the base of each internode with a basal meristematic region responsible for cell division, followed by a region of cell expansion, a region of secondary cell wall deposition, and finally a mature region of sugar accumulation at the top of the internode (Martin et al., 2016). Fournier and Andrieu used X-ray photographs and serial dissections to examine internode elongation dynamics in maize in relationship to other components of the phytomer and identified four phases of elongation (Fournier and Andrieu, 2000). Elongation begins with an initial exponential rise followed by a short period of rapid increase in which leaf sheath elongation rate decreases and internode elongation rate increases. Next occurs a sustained period of constant internode elongation rate which is followed by a final short period of exponentially decline (Fournier and Andrieu, 2000). The transition from the initial exponential

period to the first phase of constant rapid elongation coincides with the emergence of the leaf collar (Nakamura et al., 2011).

As a collection of internodes, tiller development is staggered such that when elongation decreases in one internode, the rate of elongation increases in the next internode above it and initiates in the topmost internode (Morrison et al., 1994). Together, the internodes on a given tiller represent a developmental profile over time that proceeds with the oldest internodes at the base and the youngest internodes at the tip of the tiller. Internode developmental patterns are also a function of internode age such that the elongation period increases with age (Nakamura et al., 2011). Environmental perturbations to internode development are recorded as changes in internode dimension up the tiller.

The relationship between an internode and its associated phytomer components places certain constraints on the measurement of internode elongation. An internode is typically hidden by the leaf sheath of the previous phytomer. Internode elongation can be estimated by tracking the height of an elevating leaf collar relative to the previous highest collar that has completed its elevation. Otherwise, direct measurement of internode elongation requires either X-ray imaging or destructively peeling away of the leaf sheath. Serial dissections provide a destructive means to infer elongation patterns over time (Fournier and Andrieu, 2000). Because of the time-consuming nature of these direct procedures, many studies rely on dissections of destructively harvested plant material taken at a specific developmental stage with measurements of internode length and width done by tape measure and caliper (Muthurajan et al., 2011). Of these studies, very few are done on C_4 crops in a quantitative genetics context; likely due to the difficulty associated with performing these measurements on large plants (Hilley et al., 2017).

These phenotyping methods have been used to improve our understanding of stem growth responses to the environment and to elucidate the genetic architecture of internode elongation. Internode elongation responds in different ways to various environmental conditions. A classic example is the positive response of vegetative internode elongation to flooding in deepwater rice. Gibberellin biosynthesis and signal transduction have been shown be key mechanisms that control this response and numerous genes to the process have been identified (Liu et al., 2011; Qi et al., 2011; Ayano et al., 2014). On the other hand, internodes respond negatively to water-deficit in C_4 grasses (Hemaprabha et al., 2013; Yang et al., 2016). Relative to deepwater rice, these systems are understudied and the mechanisms and underlying genetic

architecture of this response are not well known. Because internodes respond variably to the environment and because these internode modifications also influence the performance of the resource capture and reproductive organs that they support, internode morphology may be a trait that impacts local adaptation. Although this has been suggested in the literature, major gaps remain in relating natural internode diversity to geography and climate (Brown, 1959; Ochiai, 1996).

Numerous studies in maize and sorghum have explored internode elongation dynamics as a means of improving biomass productivity in C_4 grass feedstocks and energy sorghum has been suggested a potential genetic model (Mccormick et al., 2016). However, these systems have a large physical stature and long growing season which makes them ungainly for studying tiller-wide internode elongation responses to abiotic stress in a quantitative genetics context. *Setaria viridis* (L.) Beauv addresses these limitations as model system for C_4 grass architecture (Doust et al., 2009). *Setaria* has many of the strengths associated with a model system: relatedness to economically valuable species, small size, rapid life cycle, inherent drought tolerance, small genome, genetic resources. Setaria has largely been used as a model for photosynthesis, but increasingly is being used to study height, aboveground biomass, water use efficiency, and stem development (Martin et al., 2016; McGaughey et al., 2016; Feldman et al., 2017; Fahlgren et al., 2018). Having a rapid life cycle means that the entire developmental cycle of the plant, from germination to panicle maturation, can be evaluated. The small size of Setaria allows imaging techniques to produce a permanent record of whole stem and component internode dimensions across entire mapping populations.

Two primary *Setaria* mapping populations are available for detecting genotype-to-phenotype associations. The first is a recombinant inbred line (RIL) population derived from a cross between *Setaria viridis* A10 and *Setaria italica* B100 which contains a phenotypic distribution representative of a mixture of both natural and domesticated aboveground plant architectures (Mauro-herrera and Doust, 2016). The resulting RILs contain a wide variation in aboveground architecture including internode characteristics that can be related to genotypic variation to detect quantitative trait loci (QTL). The second is a natural diversity panel of North American *Setaria viridis* accessions which represents both the results of local adaptation and the demographic history of introductions to the continent from Eurasia as well as introgression from *Setaria italica* (Huang and Feldman, 2017). As a result, this population contains a vast amount of

phenotypic and genotypic variation that can be leveraged to detect genotype-to-phenotype association at the single nucleotide polymorphism (SNP) level via genome wide association studies (GWAS).

The present study combined models of internode elongation with image-based measurements of internode morphology to evaluate internode elongation and arrangement responses to water-deficit treatment in the field on the two aforementioned *Setaria* mapping populations. This approached was used to ask the following questions: (1) How does internode elongation respond to water-deficit treatment? (2) How do internode phenotypes inform local adaptation? (3) What is the genetic architecture of internode elongation and arrangement?

METHODS

Field site

Experiments were conducted at the South Farms of the University of Illinois Urbana-Champaign (Latitude: 40.04, Longitude: -88.23). The field site is rain-fed, tile-drained, and has a deep, organically rich, Flanagan/Drummer series type soil. Climate conditions were downloaded from archival data collected from a weather station operated by the Illinois State Water Survey located 3.6 miles north of the field site (ISWS). All plant materials were obtained from the Donald Danforth Plant Science Center, St Louis, MO.

2014 RIL experiment

Experimental design, plant material, treatment application

The experiment, from seed sowing to final destructive biomass harvest, ran from June 8th to August 28th**,** 2014. The experiment was a complete block design replicated three times with two water treatments (well-watered and water-deficit). The position of subplots containing individual genotypes were randomized in the first block and then these positions repeated in the replicate blocks. Following the protocols used by Banan et al., 2018 and Feldman et al., 2017, 155 F7 recombinant inbred lines and the parental lines *Setaria viridis* A10 and *Setaria italica* B100 were germinated in a glasshouse and transplanted by hand into a mechanically tilled field nine days after sowing. Additional A10 and B100 were planted as check plots. Plants were arranged in 0.3 m by 0.3 m plots each containing 36 plants with 5 cm grid spacing and housed under rain-out shelters which diverted precipitation from both well-watered and water-deficit treatment plots (Gray et al., 2016). Plants in both treatments were hand watered immediately after transplanting until establishment. Drip irrigation was applied to well-watered plants and

irrigation was fully withheld from water-deficit plots after transplant establishment. As described in detail by Markelz et al., 2011, volumetric water content in 10-cm increments between depths of 5 to 105 cm was measured three times weekly using a capacitance probe inserted into access tubes installed in parental check plots distributed throughout the experimental plots (Diviner 2000, Sentek Sensor Technologies; Markelz et al., 2011).

A flooding event on July 12th, 2014 (32 DAS) interrupted the progression of the RIL experiment. Luckily, a separation in volumetric water content was established early enough to impose a treatment effect on culm height (Figure 4.1).

Panicle emergence and plant height

Panicle emergence was surveyed daily in the field and recorded as the number of days after sowing at which the panicle head was seen past the collar of the culm flag leaf in at least half of the non-perimeter individuals in a genotype specific plot. The height of three specific non-perimeter plants in each genotype subplot was measured repeatedly with a tape measure 25, 33, 40, and 47 DAS as well as at maturity. Height was defined as the distance from the plant base to the uppermost leaf collar on the culm in centimeters.

Curve fitting

A Gompertz growth function (Formula 4.1) modeled height as a function of time, *y(t),* within each subplot using the five height timepoints as data inputs.

Formula 4.1:

$$y(t) = ae^{-be^{-ct}}$$

where *e* is Euler's number, *a* describes the horizontal asymptote, *b* describes displacement along the x-axis, and *c* describes the growth rate. Curve fitting was performed in SAS using the *proc nlin* function assuming height of zero on the day of sowing and with initial parameter estimates set as a = 20 to 60 by 20, b = 40 to 60 by 10, and c = -1 to 1 by 0.5. Model output parameters were used to calculate predicted height values from 0 to 100 days after sowing for each subplot and these predicted values were used for subsequent trait calculation.

Trait calculation (summarized in Table 4.1 and Figure 4.2)

The final height of the culm was estimated as 99% of the maximum predicted value when fitting the Gompertz function (large dashed, horizontal line in Figure 4.2). The total period of

growth was determined as the number of days since sowing when this final height was achieved (large dashed, vertical line in Figure 4.2). Height on the date that panicle emergence was observed was estimated from the function of predicted height (small dashed, horizontal line in Figure 4.2). The number of days after sowing until panicle emergence was used as an estimate for the timing of the culm apical meristem's transition from vegetative to reproductive development (small dashed, vertical line in Figure 4.2). The increase in height following panicle emergence was assumed to be driven by the elongation of the distal-most vegetative phytomer, since height was measured to the base of the flag leaf and did not include the peduncle or panicle. The amount of this elongation driven height was calculated as the difference between final height and height at panicle emergence. The duration of this period of elongation driven growth was calculated as the difference between the total growth period and the number of days to panicle emergence. The proportion of height driven by elongation was calculated as the amount of elongation driven height divided by the final height and the proportion of the growth period driven by elongation was calculated as the elongation driven growth period divided by the total growth period.

QTL analysis

Quantitative trait loci analysis, calculation of relative additive effects, and definition of confidence intervals followed methods detailed in Feldman et al. 2017 and Banan et al. 2018 (Chapter 2). Data extracted from these studies were compared to the present QTL results to determine the degree of similarity in co-localization, allelic effect, and phenotypic correlation.

Statistical analysis and visualization

The following R packages were used for statistical analysis and visualization: *t.test(), lm(), cor.test(), ggplot2()*. To test whether the slope of the linear regression between height at panicle emergence (WD / WW) and height at plateau (WD / WW) differed significantly from the identity line (1:1), a t-statistic was calculated as:

(best fit slope – hypothetical slope) / standard error of slope

and matched to its corresponding two-tailed P-value using *pt()*.

2016 Diversity panel experiment

Experimental design

The experiment, from seed sowing to final destructive biomass harvest, ran from June 11th to August 24th, 2016. The experiment was a randomized complete block design replicated

twice with two water treatments (well-watered and water-deficit). 209 genotypes composed of a panel of 207 North American *Setaria viridis* accessions, *Setaria viridis* accession A10, and *Setaria italica* B100 were germinated in glasshouse and transplanted by hand into a mechanically tilled field seven days after sowing. Plants were arranged in 0.3 by 0.25 m plots each containing 30 plants with 5 cm grid spacing housed under retractable awning rain-out shelters which diverted precipitation from both well-watered and water-deficit plots (Gray et al., 2016). Plants in both treatments were hand watered immediately after transplanting until establishment. Drip irrigation was applied to well-watered plants and irrigation was fully withheld from water-deficit plots after transplant establishment. Volumetric water content was measured three times weekly using a capacitance probe inserted into access tubes installed in parental check plots distributed throughout the experimental plots (Diviner 2000, Sentek Sensor Technologies; Markelz et al., 2011).

Climate conditions (reported in Chapter 3, Supplemental Figure 3.1)

Field protocols

Panicle emergence was evaluated in the field using the same protocol as the 2014 RIL experiment. Once transplanting was established**,** three non-perimeter plants were tagged around the culm and reserved for end of season destructive sampling and internode imaging.

Sample collection and processing

At 30 days post panicle emergence in each genotype specific plot, tagged plants were removed from the field such that the crown was left intact and tillers remained connected at the plant base. Root material was separated from the crown using garden shears. Leaf blades were counted, removed, and dried at 65 ^{o}C. Panicles were removed and dried at 65 ^{o}C. The culm panicle was weighed both separately and as part of the per-plant cumulative panicle mass. Bare stems were placed in baguette bags and dried intact at 65 ^{o}C. Stem architectural traits were measured on dried samples. Basal crown width was measured as the caliper width of the crown. Tiller number was measured as the count of tillers emerging from the basal-most crown nodes. Branch number was measured as the count of primary branches emerging from tiller nodes. Culm height was evaluated as the height between the base of the plant and the collar of the flag leaf. Dried stem, leaf, and reproductive tissues were weighed on a digital mass balance.

Image collection and feature extraction

For each subsample per plot, the tagged culm was isolated from the intact stem material and sectioned into its component internodes using pruning shears. Compressed internodes at the base of the stem were not sectioned if there were no visibly expanded internodes between nodes. Sectioned internodes were arranged on a black matte fabric next to a reference object such that the basal to distal order and orientation throughout the stem and within segments was maintained. The arranged internodes were imaged using a digital camera held at a fixed height from the imaging stage on a copy stand (Canon EOS 7D, 50 mm lens, Canon Inc, Huntington, NY, USA). The resulting images were passed through an automated macro which binarized the images and identified internodes and reference objects using their area and dimensional proportions (ImageJ, National Institutes of Health, Bethesda, MD, USA). The image analysis outputs were converted from pixel scale to millimeters and used to calculate traits that describe the dimensions of the sectioned internodes. After imaging, the sectioned internodes were added back to their respective stems for weighing.

Trait calculations (summarized in Table 4.1)

Population structure

A matrix of single nucleotide polymorphisms for each accession was provided by Max Feldman. The matrix was composed of 1316 markers selected for being in a non-transcribed sequence, present in all samples, having a major allele frequency > 0.3, and having 1 marker every 100 kb evenly tiled across genome. Population structure was visualized using the biplot generated from principal component analysis of the SNP matrix using the *prcomp()* R package. The degree to which phenotypes clustered with different aspects of population structure was determined using the resulting principal components as genetic axes for correlation.

Geography and climate data

Accession latitude and longitude coordinates were provided by the primary collectors of the North American diversity panel, Dr Max Feldman and Dr Pu Huang. For map visualization, raster data was extracted and visualized from the *ggmaps()* R package. Accession collection locations were mapped and color coded based on their internode phenotype PC1.

Climate parameters were extracted from the BioClim database which contains 19 bioclimatic variables commonly used in ecology (Pearson 2014). The database was then subset to include only climate data corresponding to accession collection locations.

GWAS and candidate gene analyses

GWAS detected SNPs using three levels of significance: (1) Mbonf, (2) eBIC, and (3) MaxCoef. The first two are considered of high confidence and use multiple testing corrections. The MaxCoef is more relaxed and produces reasonable possibilities but is prone to detecting false positives. Analysis of GWAS results was subset to hits produced by the strictest criteria (Mbonf and eBIC) or individual SNPs significant in MacCoef that were detected in both treatments.

RESULTS

2014 RIL experiment

Modeled height values anchored by developmental landmarks reveal elongation-specific responses to water-deficit

Height to the base of the flag leaf was measured manually throughout the growing season and fitting a Gompertz growth function was combined with developmental landmarks (panicle emergence and final height) to generate a number of traits describing the elongation of the distal-most vegetative phytomer (Figure 4.2).

The timing and amount of cumulative vegetative height and growth produced by elongation of distal-most vegetative phytomers was compared between well-watered and water-deficit treatments across the RIL population. Although the number of days after sowing until panicle emergence was not significantly different between treatments (Figure 4.3 A, P-value = 0.93), the number of days after sowing until final height was reached was significantly delayed under water-deficit compared to well-watered (Figure 4.3 B, P-value =0.00052). A period of elongation-specific growth, which was identified as the period between panicle emergence and final height of the culm being reached, was significantly greater under water-deficit than well-watered treatments (Figure 4.3 C, P-value = 2.3e-06). The proportion of the total period of growth identified as elongation specific (i.e. no new vegetative phytomers being formed) was also significantly greater under water-deficit than well-watered treatments (Figure 4.3 D, P-value = 2e-07). Both the height at panicle emergence and the final height were significantly reduced under water deficit compared to well-watered treatments (Figure 4.3 E, P-value = 1.5e-10; Figure 4.3 F, P-value = 8.2e-06). The absolute amount of elongation by the distal-most vegetative phytomer was not significantly different between treatments (Figure 4.3 G, P-value = 0.12). But, the proportion of vegetative height produced by elongation of the distal-most vegetative

phytomer was significantly greater under water-deficit than well-watered treatments (Figure 4.3 H, P-value = 1.9e-07).

Final height was positively correlated with the number of days after sowing until panicle emergence under water-deficit (Figure 4.4 A, Pearson's R = 0.42, P-value < 0.001). But, the proportion of vegetative height produced by elongation of the distal-most vegetative phytomer was negatively correlated with the number of days after sowing until panicle emergence under water-deficit (Figure 4.4 B, Pearson's R = -0.47, P-value < 0.001). In other words, plants that transitioned from vegetative to reproductive development later in the growing seasons tended to be taller. However, these tall, late transitioning plants had a smaller proportion of their growth produced by the elongation of the distal-most vegetative phytomer.

Distal-most vegetative phytomer expansion acts as a compensatory growth mechanism in response to water-deficit

The correlation between the effect of the water-deficit treatment on height at panicle emergence and the treatment effect on final height was used to determine if elongation by the distal-most phytomer was more or less sensitive to water-deficit than the preceding growth processes. Treatment effects were calculated as the ratio of trait values in the water-deficit and well-watered treatments. The treatment response of height at panicle emergence and the treatment response of final height were positively correlated (Figure 4.5, $R^2 = 0.25$, P-value = 0.471e-16). The y-intercept of the function was 0.50 (P-value = 4.52e-11) and the slope of the linear function was 0.47, which was significantly shallower than the 1:1 line (T-statistic = 7.95, P-value = 4.24e-13). Therefore, the gap between the line of best fit and 1:1 line progressively widens as the effect of water deficit on height at panicle emergence becomes greater. This indicates that as the effect of water deficit on height at panicle emergence became stronger, it was compensated to a progressively greater degree by more sustained elongation of the distal-most vegetative phytomer. Although, it is important to note that only 25% of the variation among genotypes in the water deficit effect on final height is explained by this relationship.

Phytomer elongation traits detect genotype-to-phenotype associations reflective of phenotypic correlations and co-located with other aspects of aboveground architecture

Sixty-five significant QTL were detected across eight traits and two treatments (Table 4.2, Figure 4.6). The majority of loci clustered in 11 clusters distributed across chromosomes two, three, five, eight, and nine. QTLs were considered distinct if their confidence intervals did

not overlap, with confidence intervals being calculated as the breadth of the QTL peak where it intersected the threshold for significance assuming a peak LOD score 1.5 times the observed value. Single loci were detected for: final height under well-watered treatment (chromosome 1 @ position ~80 cM = 1@~80, 4@~50); the proportion of the total period of growth identified as elongation specific under water-deficit treatment (6@~70); and the proportion of vegetative height produced by elongation by the distal-most vegetative phytomer under water-deficit (7@~75). Only the cluster located at 5@~110 was composed solely of traits related to the height and timing of panicle emergence. The remaining QTL clusters were composed of a mixture of traits describing the timing of panicle emergence and the growth period, the height at these developmental landmarks, and the amount and proportion of growth produced by elongation of the distal-most vegetative phytomers.

To normalize allelic effects, a relative additive effect for each loci was calculated as the additive effect divided by the trait mean. In general, QTL that were found in clusters had allelic effects in the same direction as each other. Notable exceptions were observed on chromosome two, three, five, and nine in which co-located QTL had diverging allelic effects depending on the trait. However, this genetic co-localization of allelic effects with opposing influences was consistent with the pattern of phenotypic correlations where plants that transitioned from vegetative to reproductive development later in the growing season were taller but had a smaller proportion of their vegetative height produced by elongation by the distal-most vegetative phytomer (Figure 4.3 A, B). Specifically, on chromosome two (2@~90), the final height and height at panicle emergence under well-watered treatment and the total period of growth under water-deficit had positive additive effects. At that same loci, the proportion of vegetative height produced by elongation by the distal-most vegetative phytomer had a negative additive effect. On chromosome three (3@~70), the number of days after sowing until panicle emergence under both treatments had a positive effect and traits describing the amount and proportion of height produced by elongation specific growth under water-deficit treatment had a negative effect. On chromosome five (5@~55), the height and timing of panicle emergence and final height had positive additive effects while the proportion of vegetative height produced by elongation by distal-most vegetative phytomers had a negative relative additive effect. On chromosome nine (9@~35), height at panicle emergence under water-deficit treatment and final height under well-watered treatment had positive relative additive effects while the proportion of vegetative height

produced by elongation by the distal-most vegetative phytomer under water-deficit treatment had a negative relative additive effect.

Six of the 11 QTL clusters detected in the present study were co-located with clusters for plant height detected in a previous study performed using the same *Setaria* mapping population evaluated in a wide range of environments (Feldman et al, 2017). Each of these six overlapping clusters contained QTL detected from height measurements collected in the present study following the same phenotyping protocol as Feldman et al. 2017. Three loci detected in the present study were devoid of QTL related to direct measurements of height (3@~70, 6@~75, 7@~75). Of these, two co-located with QTL previously detected through measurements of aboveground architecture in Banan et al. 2018 (3@~70, 6@~75). The remaining QTL, for the proportion of height produced by the expansion of distal-most vegetative phytomers, was novel (7@~75) to the present study.

2016 Diversity panel experiment

Image analysis of post-harvest processed culm stem material from a *Setaria* diversity panel generated a number of traits describing the dimension and relative proportions of the component internodes (Table 4.1). The resulting phenotypic space was then evaluated with respect to aboveground biomass production responses to water-deficit and reproductive strategy. Internode phenotypes were also evaluated with respect to the diversity panel's population structure and geographical distribution.

Internode trait distributions

The North American *Setaria viridis* accession population was phenotypically diverse for a number of internode traits. With the exception of total cumulative internode length, *Setaria italica* B100 was found towards the tails of the trait distributions. *Setaria viridis* A10 was generally found closer to the center of the trait distributions relative to B100. Internode traits varied in the strength and direction of their responses to the water-deficit treatment. Phytomer count, the coefficient of variation of vegetative internode lengths, and total height were not significantly different between treatments (Figure 4.8 A-C, P-values > 0.1). Vegetative height was slightly reduced in response to water-deficit treatment (Figure 4.8 D, P-value = 0.069) Peduncle length responded positively to water-deficit (Figure 4.8 E, P-value = 0.008), while peduncle width and peduncle width to length ratio were not significantly different between treatments (Figure 4.8 F, P-value = 0.16; Figure 4.8 G, P-value = 0.36). The length and width of

the distal-most vegetative internode were not significantly different between treatments (Figure 4.8 I, J; P-values > 0.1), but the width to length ratio of the distal-most vegetative internode was significantly reduced under water-deficit treatment (Figure 4.8 K; P-value < 0.031). The length of the distal-most vegetative internode was not significantly different between treatments when expressed as a proportion of vegetative height (Figure 4.8 L, P-value = 0.72). Peduncle length as a fraction of total height responded positively to water-deficit (Figure 4.8 H, P-value = 0.006). Phytomer count and the coefficient of variation of vegetative internode lengths were not significantly different between treatments, suggesting that these traits are under tight developmental control. Internode length and length relative to other stem elements responded differently to water-deficit depending on the developmental function of that internode.

Internode phenotype dimension reduction and correlation with population structure

To reduce the dimension of the diversity panel internode phenotype space, principal component analysis (PCA) was performed on data collected under water-deficit treatment for all 12 internode traits derived from image analysis (Figure 4.9). Together, the first two principal components (PCs) together explained 76.77 % of the variation in the dataset. The first principal component explained 46.58 % of the variation in the dataset. Phytomer count, the coefficient of variation of vegetative internode lengths, vegetative height, peduncle width, distal-most vegetative internode width, peduncle length as a fraction of total height, and distal-most vegetative internode length as a fraction of vegetative height loaded strongly along the first principal component (Table 4.3). The second principal component explained 29.92 % of the variation in the dataset. Total height, peduncle length, peduncle width to length ratio, distal-most vegetative internode length, and distal-most vegetative internode width to length ratio loaded strongly along the second principal component. Within the two dimensional PCA plot produced from the first two internode phenotype PCs, *Setaria italica* B100 was located on the periphery of the overall data distribution while *Setaria viridis* A10 was closer to the center. Six North American *Setaria viridis* accessions were phenotypically similar to *Setaria italica* B100 on the basis of their first two PC values.

To visualize the population structure of the *Setaria viridis* diversity panel composed of the 207 North American accessions and A10, PCA was performed on the single nucleotide polymorphism (SNP) matrix. The first two PCs explained 35.74 % of the genetic variation captured by the SNP matrix. The triangular shape produced by the two dimensional PCA plot

suggests that the population structure is dominated by three major subpopulations (Figure 10). *Setaria viridis* A10 grouped with North American accessions defined by the tail of the first SNP PC distribution and this cluster of accessions contained an intermediate range of internode phenotype PC1 values. The second SNP PC was positively correlated with the first internode phenotype PC (Figure 4.11, $R^2 = 0.24$ ***), indicating an association between population structure and internode phenotypes.

Internode phenotype correlations with life strategy, geography, and climate

Internode phenotype PC1 was positively correlated with total per-plant aboveground biomass (Figure 4.12, $R^2 = 0.47$). *Setaria viridis* A10 and *Setaria italica* B100 were used as reference genotypes to visualize their contrasting phenotypes. A10 and B100 exhibit extreme and opposite phenotypes for both internode phenotype PC1 and total per-plant aboveground biomass.

A panicle mass fraction calculated as the ratio between culm panicle mass and total panicle mass per plant was used as a measure of reproductive strategy. Ratios close to one represent a large investment towards the primary panicle. Conversely, a low ratio represents a reproductive investment spread across the culm panicle and those produced on subsequent tillers and aerial branches. Internode phenotype PC1 was positively correlated with both the number of days after sowing to panicle emergence (Figure 4.13 A, $R^2 = 0.50$ ***) and the panicle mass fraction (Figure 4.13 B, $R^2 = 0.44$), suggesting that internode phenotype PC1 is associated with late flowering genotypes that invest heavily towards their primary panicle. Phytomer count was positively correlated with panicle mass fraction (Figure 4.13 D, $R^2 = 0.43$ ***) while both the coefficient of variation of vegetative internode lengths were and the ratio between peduncle length and total internode length were negatively correlated with panicle mass fraction (Figure 4.13 E, $R^2 = 0.32$ ***; Figure 4.13 C, $R^2 = 0.29$ ***). Together, these results show that genotypes that flower early and spread out their reproductive investment across multiple panicles tend to have an internode phenotype defined by a minimal number of phytomers with varied vegetative internode lengths and a peduncle that makes up a large proportion of the total cumulative internode length. Conversely, genotypes that flower late and invest heavily in a primary panicle have many phytomers with similar vegetative internode lengths and a peduncle that only makes up a small proportion of the total cumulative internode length. *Setaria viridis* A10 and *Setaria italica* B100 once again exhibited opposite phenotypes for both traits describing

internode phenotypes and traits describing reproductive strategy. B100 was consistently at the right tail end of the distribution for these traits.

To understand how internode phenotypes relate to the geographical distribution of North American *Setaria viridis* accessions, internode phenotype PC1 values were matched with their corresponding provenance latitude and longitude (Figure 4.14). Genotypes with more positive internode phenotype PC1 values were constrained to the Great Lakes and Lower Midwest region while those with neutral to negative values were more widely distributed across the northwestern portion of the continent. The six North American *Setaria viridis* accessions that were phenotypically similar to *Setaria italica* B100 were all found in a cluster centered around Illinois and Indiana. The North American *Setaria viridis* accessions that grouped closely to *Setaria viridis* A10 with respect to population structure were found in a broad geographic range that stretched from the American Southwest up to the lower Interior Plains of Canada.

Internode phenotype PC1 had a significant correlation with the mean temperature of the warmest quarter and the precipitation of the warmest quarter at the collection site for each accession (Figure 4.15 A, $R^2 = 0.17$ ***; Figure 4.15 B, $R^2 = 0.15$ ***).

Preliminary GWAS analysis detected 188 SNPs associated with internode traits derived from image analysis under well-watered and water-deficit treatments distributed across all nine chromosomes (Figure 4.16). The majority of these SNPs were found in 13 clusters. Although many SNPs overlapped between well-watered and water-deficit treatments, some clusters were treatment specific. The preliminary SNP dataset was subset to include only those SNPs detected with the highest confidence models or those SNPs detected in both treatments by the lower confidence model (Table 4.4).

Candidate gene analysis identified 443 potential genes related to traits for internode elongation and morphology in both well-watered and water-deficit treatments. Probable gene functions based on descriptions from *Arabidopsis thaliana* and *Oryza sativa* were cross referenced against keywords for processes related to internode growth and development such as cell wall biosynthesis and hormonal regulation in *Zea mays*, *Sorghum bicolor*, *Oryza sativa*, and *Setaria viridis.* This procedure reduced the list to 46 candidate genes with probable roles in processes including aquaporin patterning, gibberellin and auxin signaling, and sugar transport (Table 4.5).

DISCUSSION

This study examined the physiology and quantitative genetics of internode elongation and arrangement to provide evidence that internode development is an important aspect of the life strategy and abiotic stress response in C_4 grasses. As a support and storage organ, internodes play a key role in producing aboveground plant architecture. However, relative to the elements that they support, such as photosynthetic and reproductive organs, internodes are understudied in C_4 grasses. This is perhaps in part due to the large size of many economically valuable C_4 crop species such as maize, sorghum, and sugarcane that makes measuring internodes within a whole-tiller context ungainly. Therefore, this study leveraged *Setaria viridis* mapping populations and a combination of growth modeling and imaging techniques to take a field-based, developmentally and anatomically focused approach to better understand internode responses to water-deficit treatment.

The data presented provide three key results: First, internode elongation recovers fitness lost to water-deficit stress by compensating for reduced vegetative growth and by elevating reproductive organs. Second, internode morphology is correlated with the life strategy as well as the geography and climate of North American *Setaria viridis* accession provenance. Third, the genotype-to-phenotype associations related to internode elongation and arrangement co-localize with other aspects of aboveground architecture and improve our understanding of the mechanisms that produce plant growth. These results expand upon previous high-throughput phenotyping studies on height, are compatible with current advances in image collection and analysis, and complement recent efforts to understand the molecular basis of stem growth in C_4 grasses.

Internode elongation as a fitness recovery mechanism under water-deficit treatment

Internode elongation responses to water-deficit were dependent on the function and relative position within a tiller of that internode. Although cumulative vegetative height was reduced under water-deficit treatment (Figure 4.8 D, P-value = 0.069), peduncle length increased and composed a greater proportion of overall stem height (Figure 4.8 E, P-value = 0.008; Figure 4.8 H, P-value = 0.006). *Setaria viridis* peduncles responded to water-deficit treatment in a manner more similar to the positive vegetative internode response to flooding of deepwater rice (Nagai et al., 2012; Ayano et al., 2014) than to the negative peduncle elongation response to drought stress in lowland rainfed rice (Muthurajan et al., 2011).

This positive growth of the peduncle despite water-deficit treatment was likely to be demanding in terms of the expenditure in maintaining osmoregulation and under stress (Gamon and Pearcy, 1989; Nonami and Boyer, 1990). However, despite this cost, there are potential fitness benefits to elevating the reproductive structures that peduncles support. Setaria is largely self pollinating, so it's unlikely that it is a pollen dispersal strategy. Rather, the increased peduncle length under water-deficit likely serves to elevate mature seeds to improve the range of their distribution. The relationship between mature panicle height and seed dispersal is well documented in the literature (Dorp and Daleboudt, 1996; Pickup and Barrett, 2012; Pazos et al., 2013). Although this specific population has not been evaluated with regards to its seed shattering diversity, *Setaria viridis* broadly is known as a seed shattering species (Hodge and Kellogg, 2016). This is also reflected in the life strategy correlations that show that elongated internodes are correlated with a reproductive investment spread out across multiple panicles produced over time (Figure 4.13).

Height at panicle emergence and final height measured in the 2014 RIL experiment were reduced under water deficit (Figure 4.3 E, P-value = 1.5e-10; Figure 4.3 F, P-value = 8.3e-06). These reductions in overall vegetative height were consistent with other studies that examined the effect of drought stress on growth of C_4 crops (Hemaprabha et al., 2013; Ku et al., 2015; Li et al., 2015; Feldman et al., 2017). Also consistent with this literature, data from the 2016 diversity panel showed that phytomer count and the coefficient of variation among vegetative internode lengths were not significantly impacted by water-deficit treatment (Figure 4.8 A, P-value = 0.28; Figure 4.8 B, P-value = 0.34). Similarly, the timing of the transition from vegetative to reproductive development, marked by panicle emergence, was not impacted by water-deficit treatment (Figure 4.3 A, P-value = 0.93). These data suggest that the timing of the transition from vegetative to reproductive development as well as the number and relative length of vegetative internodes within a tiller are under tight developmental control. Therefore, reductions in vegetative height under water-deficit are due to changes in internode elongation rather than phytomer number and arrangement or the number of days after sowing until panicle emergence.

A Gompertz growth function fitted to manual measurements of culm height taken throughout the growing season provided predicted height values at a daily resolution for genotypes grown in the 2014 RIL experiment. Panicle emergence and final height were used as developmental landmarks to bookend the duration and amount of growth produced by elongation

of the distal-most vegetative phytomer (Figure 4.2). Although the traits generated from this combination of curve fitting and developmental monitoring were not direct measures of phytomer elongation, they provided a signature of growth driven primarily by the distal-most vegetative internode. This was based on the assumption that once the panicle was visible above the leaf collar, no new internodes could form and all changes in growth were the result of elongation. At this developmental transition, leaf sheath elongation had decreased and internode elongation had entered a rapid phase of increase (Fournier and Andrieu, 2000; Song et al., 2015). The panicle at half-head emergence has been previously used to pinpoint this period of rapid internode elongation in *Setaria viridis* (Martin et al., 2016). Final height, defined as the ultimate elevation of the culm flag leaf collar, marked the end of internode elongation. This general method of estimating distal-most vegetative elongation is efficient both in terms of data collection and computation but requires accurate measurement of the flag leaf collar and may not be compatible with current field-based remote sensing techniques for measuring plant height and aboveground productivity that do not identify discrete organs (Busemeyer et al., 2013; Banan et al., 2018).

The reduction in internode elongation under water-deficit treatment is likely due to alterations in the rate and duration of organ elongation. Leaf elongation rates in maize and a number of grasses have been shown to decrease in response to both diminished water supply and high levels of vapor pressure deficit (Tardieu et al., 2005). Phytomer development is a coordinated processed and the growth dynamics of the component organs are tightly correlated (Fournier and Andrieu, 2000; Fournier, 2001). A study of maize phytomer elongation dynamics showed that both the rate and duration of organ extension are highly sensitive to environmental conditions (Vidal et al., 2018). In this study, the amount of time it took to reach final height was significantly longer, in part because elongation processes were slowed by water-deficit (Figure 4.3 B, C). Not only was the elongation growth period of the distal-most vegetative phytomer prolonged under water-deficit treatment, but a greater proportion of overall vegetative height was produced by this elongation process.

Elongation of the distal-most vegetative phytomer appears to act as a compensatory growth mechanism in response to water-deficit. The impact of water-deficit treatment on final height and height at panicle emergence was calculated as the ratio between well-watered and water-deficit values for each trait (Figure 4.5). The y-intercept of the regression between the

impact of water-deficit treatment on final height and the impact of water-deficit treatment on height at panicle emergence was 0.50. The slope of this regression was 0.47 and significantly different from the 1:1 line. These coefficients describe a widening gap between the line of best fit and the 1:1 as the impact of water-deficit treatment on height at panicle emergence becomes more severe (WD / WW closer to zero). Plants that were more negatively impacted by water-deficit treatment at panicle emergence produced a proportionally greater amount of their final height via elongation of the distal-most vegetative phytomer.

Together, this increased proportion of elongation of the distal-most vegetative internode and the positive response of the peduncle growth under water-deficit treatment appear to act as a sprint to the finish line that mitigates lost vegetative height via elongation of the distal-most vegetative internode and improves seed dispersal potential by elevating panicles.

Correlation between internode morphology, life strategy, and species distribution

To provide a developmentally equivalent comparison of internode morphology across a phenotypically diverse population containing a wide range of phytomer counts, the distal-most vegetative internode and the peduncle were identified through analysis of the images taken in the 2016 diversity panel experiment. The coefficient of variation was calculated among vegetative internode lengths within a tiller to characterize the population diversity of internode arrangement. These calculated traits combined with other metrics of internode patterning produced a trait space (Figure 4.9) that captured a portion of internode phenotypic variation which correlated with aspects of North American *Setaria viridis* biomass production, population structure, and geographical distribution (Figures 4.11, 4.12, 4.14, 4.15).

Setaria viridis A10 and *Setaria italica* B100 were used as reference genotypes to help contextualize this trait space. The undomesticated *Setaria viridis* A10 was found closer to the center of the trait space, indicating that it was phenotypically similar to the bulk of the North American accession population. The domesticated *Setaria viridis* B100 was found more on the periphery of the trait space, indicating that it was a phenotypic outlier compared to the bulk of the North American accession panel. Internode phenotype PC1 strongly discriminated between *Setaria viridis* A10 and *Setaria italica* B100 due to their location on opposite ends of the internode phenotype PC1 axis. Traits that loaded strongly and positively on internode phenotype PC1 included phytomer count, vegetative height, peduncle width, and distal-most vegetative internode width. Traits that loaded strongly and negatively on internode phenotype PC1 included

the coefficient of variation of vegetative internode lengths, distal-most vegetative internode length as a fraction of vegetative height, and peduncle length as a fraction of total height. These trait loading strengths and directions match with the contrasting internode phenotypes presented by *Setaria viridis* A10 and *Setaria italica* B100. Interestingly, six accessions stood out for their phenotypic proximity to *Setaria italica* B100.

Life strategy was evaluated with respect to the timing of the transition from vegetative to reproductive development, biomass production, and reproductive investment calculated as the proportion between culm panicle mass and total per-plant panicle mass. The relationship between internode morphology and life strategy appears to be described by a distribution of contrasting architectures (Figure 4.13). One extreme is an architecture comprised of tillers assembled from a few, variably elongated internodes which support multiple panicles that spread out the reproductive investment. At the other extreme is an architecture comprised of a tiller assembled by many wide internodes each of a similar length that supports one or few panicles that contain the bulk of the plant's reproductive investment.

Internode phenotype PC1 was positively correlated with total per-plant biomass (Figure 4.12), suggesting that plants whose growth was produced by many similarly sized internodes with little investment in peduncle elongation tended to produce more absolute biomass. These differences in biomass production and internode phenotype are also consistent with correlation between the timing of the transition between vegetative and reproductive development and internode elongation and morphology. The number of days after sowing until panicle emergence was positively correlated with internode phenotype PC1 (Figure 4.13 A) such that late flowering accessions were typified by the architecture comprised of a tiller assembled by many wide internodes each of a similar length. The number of days after sowing until panicle emergence was positively correlated with final height (Figure 4.4 A) and negatively correlated with the proportion of final height produced by elongation of the distal-most vegetative phytomer (Figure 4.4 B). In other words, plants that transitioned from vegetative to reproductive development later in the growing seasons tended to be taller. However, these tall, late transitioning plants had a smaller proportion of their growth produced by the elongation of the distal-most vegetative phytomer.

The broad geographical distribution of accessions with low internode phenotype PC1 values was consistent with a growth and reproductive strategy that flowers early and spreads its

reproductive investment across multiple panicles supported by proportionally long peduncles (Figure 4.14). Many of these accessions were identified as being genetically similar to *Setaria viridis* A10. In contrast, accessions that exhibited the highest internode phenotype PC1 values were more constrained in their distribution, especially those six accessions that were identified as phenotypically similar to *Setaria italica* B100.

Following this apparent geographical clustering, internode phenotype PC1 was positively correlated with the mean temperature of the warmest quarter and the precipitation of the warmest quarter at the site of accession collection (Figure 4.15 A, $R^2 = 0.20$ ***; Figure 4.15 B, $R^2 = 0.17$ ***). This suggests that accessions with higher internode phenotype PC1 values are more commonly found in warm and wet environments while accessions with lower internode phenotype PC1 values are more commonly found in cool, dry environments. The reported R^2 values that describe the relationship between internode phenotype and climate parameter are within the range of values observed in literature that took a similar ecophysiological approach using the same BioClim database. A study of European *Arabidopsis thaliana* accessions found a significant correlation between a phenotype PC that loaded heavily for traits describing photosynthesis, aboveground architecture, and reproductive traits and a climate PC that loaded heavily for parameters describing the amount and variability of precipitation with an $R^2 = 0.36$ (Wolfe and Tonsor, 2014). A study of a large *Populus trichocarpa* accession population collected from across North America observed R^2 values between 0.04 and 0.25 describing the correlation between various stomatal traits and various climate traits (Mckown et al., 2018).

At this point it is unclear the degree to which introgression from *Setaria italica* B100 has influenced the internode phenotypes of North American *Setaria viridis* accessions. Future work should extend this geography and climate approach to bridge the internode phenotyping results presented here with the ongoing work to unravel the demographic history (Huang and Feldman; Huang et al., 2014; Schröder et al., 2016).

Genotype-to-phenotype associations for internode elongation and arrangement improve our understanding of plant architecture

QTL analysis detected numerous loci associated with phenotypes generated from the 2014 RIL experiment (Figure 4.6, Table 4.2). The majority of these loci were found in clusters associated with a mixture of traits related to the timing of panicle emergence and the growth period, the height at these developmental landmarks, and the amount and proportion of growth

produced by elongation of the distal-most vegetative phytomer. Within clusters, the direction of relative additive effects was consistent with phenotypic correlation patterns and suggested both a physiological and genetic link between the proportion of growth produced by elongation of the distal-most internode and the transition from vegetative to reproductive development (Figure 4.4 B).

Comparisons to field trials using the same RIL population showed co-localization between QTL from this study and six previously described loci associated with plant height (Feldman et al., 2017). Additionally, two loci previously described for branch number and the angle of tiller spread were co-localized with QTL related to the transition from vegetative to reproductive development and the amount and proportion of height produced by elongation of the distal-most vegetative internode (Banan et al., 2018). A single loci detected in this experiment was novel for the proportion of height produced by elongation of the distal-most vegetative internode. These clustering results suggest that while a large portion of the genetic architecture related to phytomer elongation co-localized with absolute vegetative height, there are aspects of elongation specific growth that relate to other unique aspects of aboveground architecture and development.

PCA of the SNP matrix was used to visualize the population structure of North American *Setaria viridis* accessions. The resulting two dimensional PCA plot had a triangular shape with accessions clustered at each of the three corners and also spread across the edges and throughout the middle (Figure 4.10). *Setaria viridis* A10 was used as a reference for comparison against the North American accessions and was found clustered in one of the corners of the population structure visualization.

The triangular shape of the two-dimensional SNP PCA plot was consistent with prior studies that examined the population structure of this same diversity panel and described three major subpopulations (Huang et al., 2014; Schröder et al., 2016). Two of these subpopulations are likely of Eurasian *Setaria viridis* origin and have a strong north-south geographical separation within North America while a third subpopulation has a genomic signature of *Setaria italica* introgression.

Future directions

GWAS detected numerous SNPs related to internode dimension and arrangement which can be later linked to candidate genes (Figure 4.16). Candidate genes may be related to processes

such as cell wall deposition and loosening (Martin et al., 2016), aquaporins (McGaughey et al., 2016), or gibberellin sensitivity (Nagai et al., 2012; Ayano et al., 2014). The genotype-to-phenotype associations detected by QTL analysis of internode elongation traits underlie many of the same genetic features detected by coarse height and aboveground architecture. This suggests that internode development is fundamental to generating plant growth and shape.

The correspondence between the internode elongation responses to water-deficit treatment in the present study and the elongation mechanisms described in the literature should further motivate the use of *Setaria viridis* internodes as model for improving stem growth under both ideal and stressed conditions. The data presented here emphasized morphology and quantitative genetics approaches while Martin and McGaughey emphasized a cellular and transcriptomic approach. Furthermore, the opposite elongation responses to water-deficit treatment observed between the distal-most vegetative internode and the peduncle suggest that the peduncle may act as a complementary model to the expanding internode to improve our understanding of stem growth responses to drought stress.

High-throughput phenotyping of just height or productivity are efficient means of assessing biomass but do not capture the actual processes at play. Without a developmental and anatomical focus, these methods can at best measure the gross outcome and will miss potentially interesting patterns such as peduncle positive growth and the increased proportion of final height produced by elongation of the distal-most vegetative internode under water-deficit treatment.

FIGURES AND TABLES

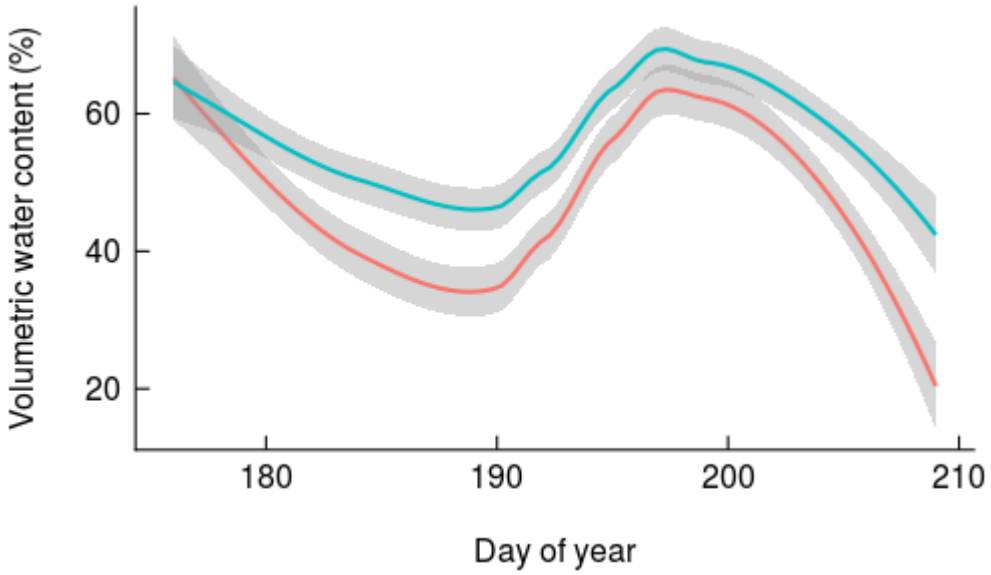

Figure 4.1: Volumetric water content (VWC, %) averaged across soil horizons 5 – 25 cm deep throughout the 2014 growing season. The blue line represents a loess regression of VWC measured in access tubes located in well-watered plots with error in grey while the red line represents the corresponding water-deficit plots. The sudden rise in VWC after day of year 192 corresponds with a flooding event in which all experimental plots were inundated.

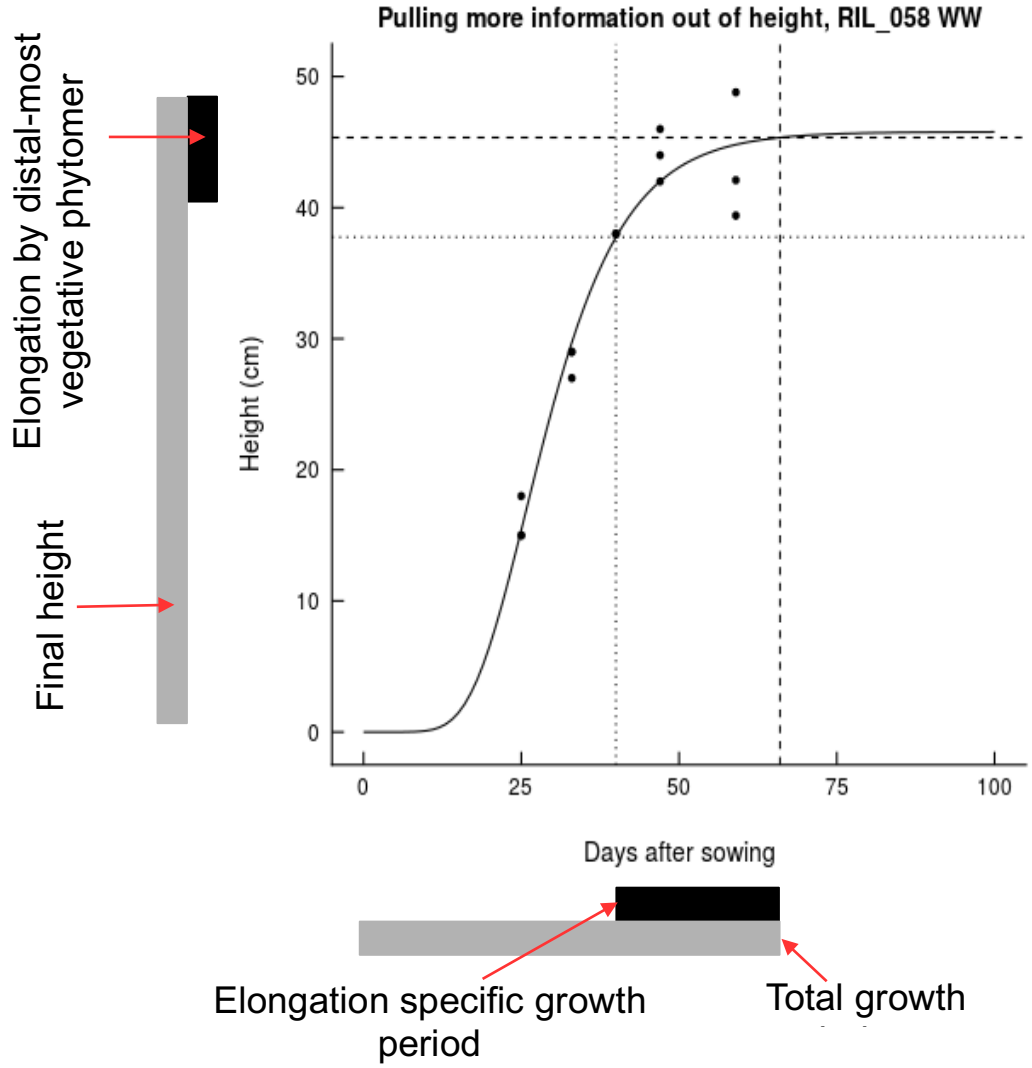

Figure 4.2: Visual representation of trait calculations for 2014 RIL experiment (also summarized in Table 4.1). Example data pulled from RIL_058 in well-watered treatment. Points represent manually collected height measurements from five timepoints throughout growing season. Solid line represents predicted values between 0 and 100 days after sowing generated from a Gompertz growth curve fit to the manually collected height measurements.

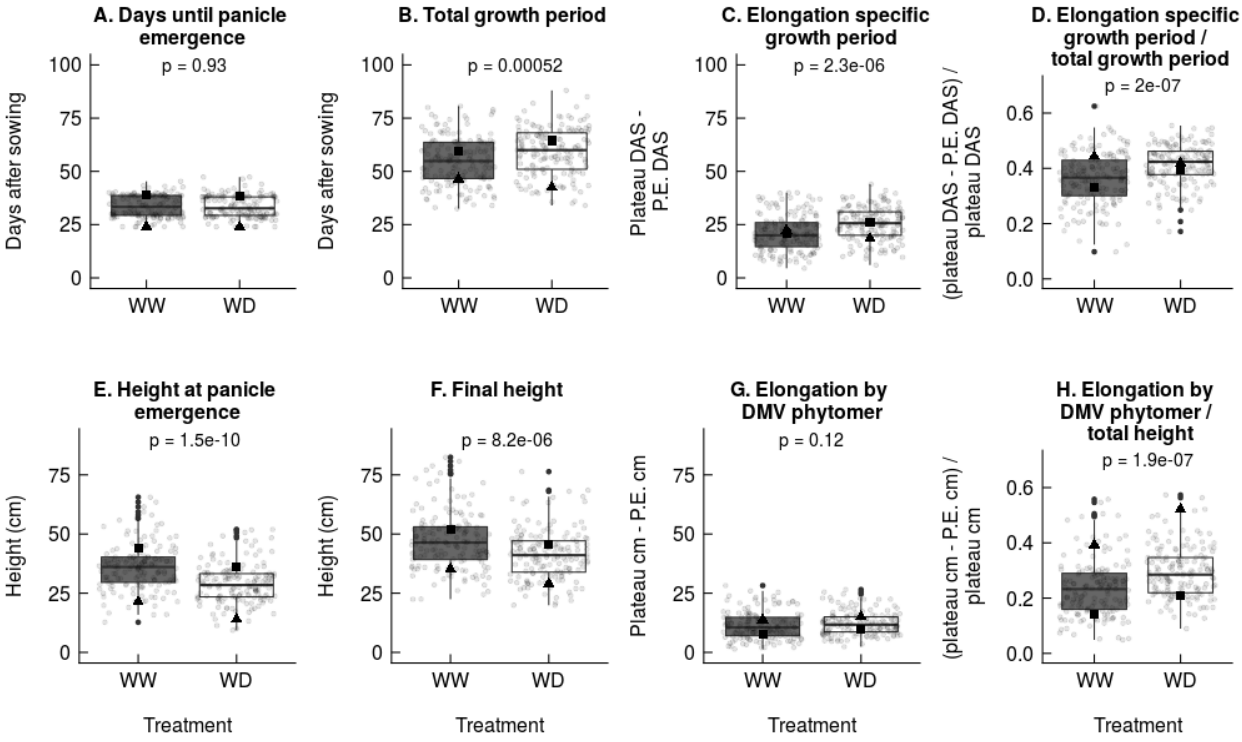

Figure 4.3 A-H: Box plots of growth and elongation traits from 2014 RIL experiment. Growth and elongation trait distributions for well-watered (dark grey box plots) and water-deficit (white box plots) treatments. Jittered light grey points represent genotype * treatment averages for each RIL, solid black squares represent average *Setaria italica* B100 values, solid black triangles represent average *Setaria viridis* A10 values. P-values displayed for results of Welch's two sample t-test. DMV: distal-most vegetative

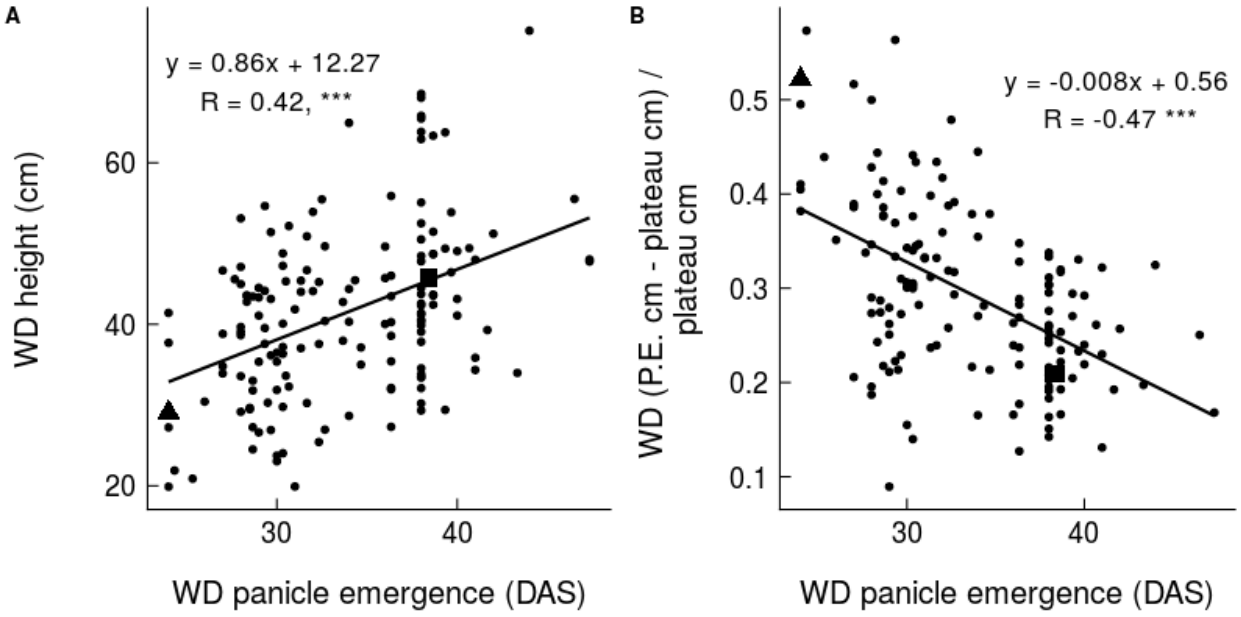

Figure 4.4: Final height and proportion of final height produced by elongation of distal-most phytomer correlations with days after sowing until panicle emergence. (Figure 4.4 A) Correlation between final height and the number of days after sowing until panicle emergence. (Figure 4.4 B) Correlation between the proportion of final height produced by elongation of the distal-most vegetative phytomer and the number of days after sowing until panicle emergence. Data taken from water-deficit treatments. Circle points represent RIL averages, square points represent *Setaria italica* B100, triangles represent *Setaria viridis* A10. Line of best fit represents linear regression between traits. Pearson's correlation coefficients are reported with stars indicating P-value: ns > 0.05, * < 0.05, ** <0.01, *** < 0.001

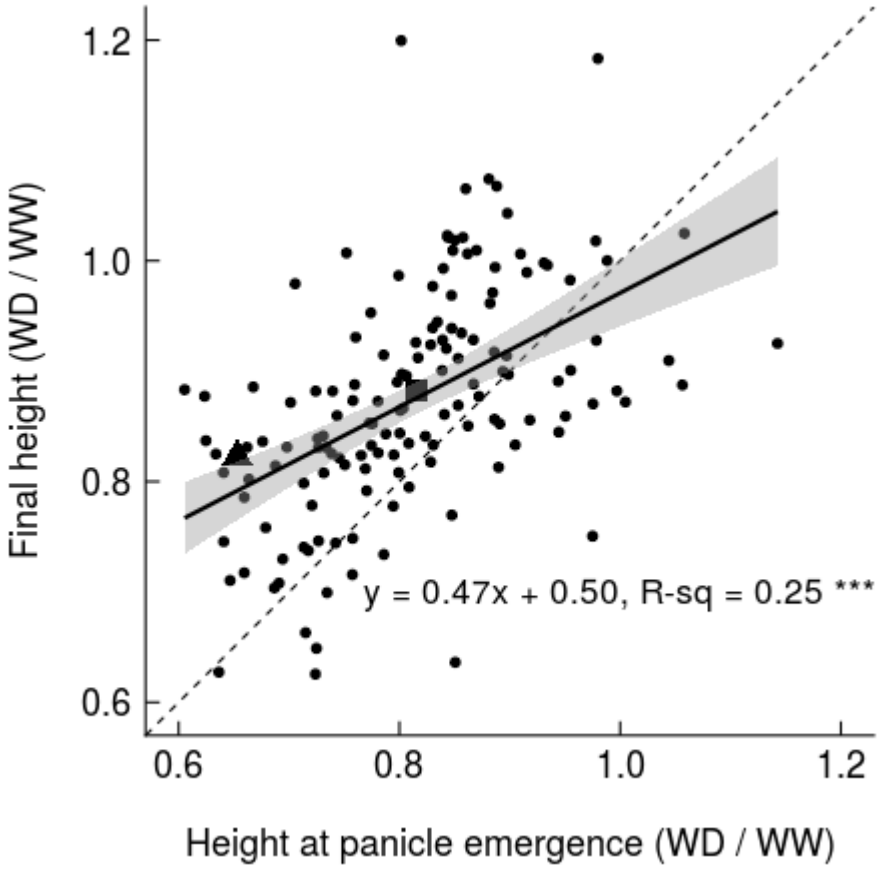

Figure 4.5: Comparison of early and late season height responses to water-deficit treatment. Correlation between response to water-deficit treatment of height at panicle emergence and final height. Response to water-deficit treatment calculated as WD value / WW value. Circle points represent RIL averages, square points represent *Setaria italica* B100, triangles represent *Setaria viridis* A10. Dashed line represents 1:1 line. Solid line represents the linear regression between traits. Slope of linear regression: M = 0.47, P-value = 4.71e-16. Y-intercept of linear regression: B = 0.50, P-value = 4.52e-11. Slope of linear regression was tested against the 1:1 line by calculating a T-statistic: -7.95 = (best fit slope – hypothetical slope) / standard error of slope, P-value = 4.24e-13.

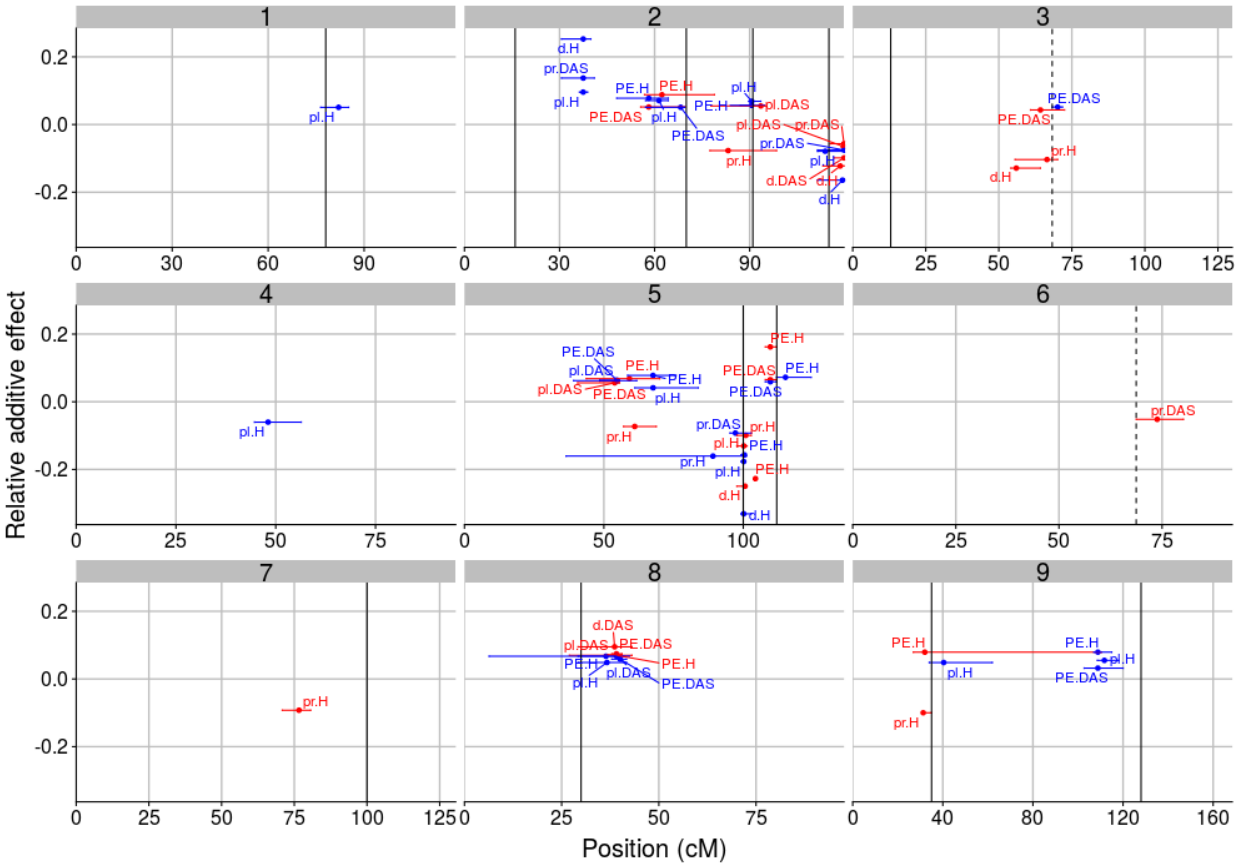

Figure 4.6: QTL mapping for growth and elongation traits. Panels 1-9 correspond to each chromosome in the Setaria genome. Additive effects relativized by phenotypic mean are plotted against centimorgan position for each QTL. Error bars represent the 1.5 LOD score confidence interval for each QTL's location. Blue points represent QTL detected for traits measured under well-watered treatment, red points represent QTL detected for traits measure under water-deficit treatment. Solid black lines represent clusters for plant height detected across a wide range of field and controlled-condition environments described in Feldman 2017. Dashed black lines represent QTL for aboveground architecture previously described in Banan 2018 (Chapter 2). PE.H=height at panicle emergence, pl.H=final height, d.H=elongation by distal-most vegetative phytomer, pr.H=proportion of vegetative height produced by elongation of the distal-most vegetative phytomer, PE.DAS=days after sowing until panicle emergence, pl.DAS=total growth period, d.DAS=elongation-specific growth period, pr.DAS=proportion of the total growth period produced by elongation of the distal-most vegetative phytomer

Figure 4.7. Environmental and soil moisture conditions during 2016 diversity panel experiment. (Please see Chapter 3, Supplemental Figure 3.1)

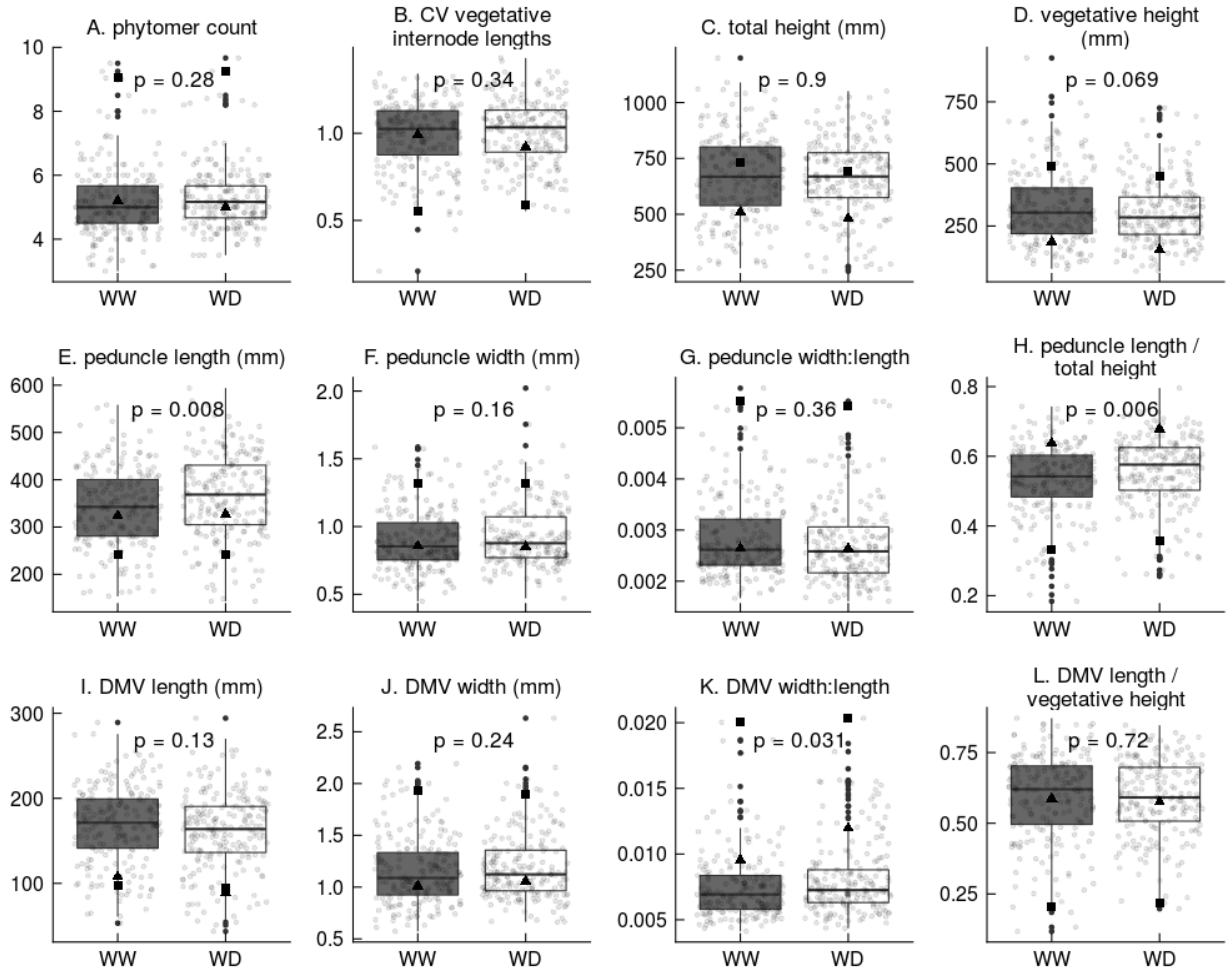

Figure 4.8 A-L: Internode morphology trait distributions for well-watered (dark grey box plots) and water-deficit (white box plots) treatments. Jittered light grey points represent genotype averages for each North American *Setaria viridis* accession, solid black squares represent average *Setaria italica* B100 values, solid black triangles represent average *Setaria viridis* A10 values. P-values displayed for results of Welch's two sample t-test. CV=coefficient of variation, DMV=distal-most vegetative internode

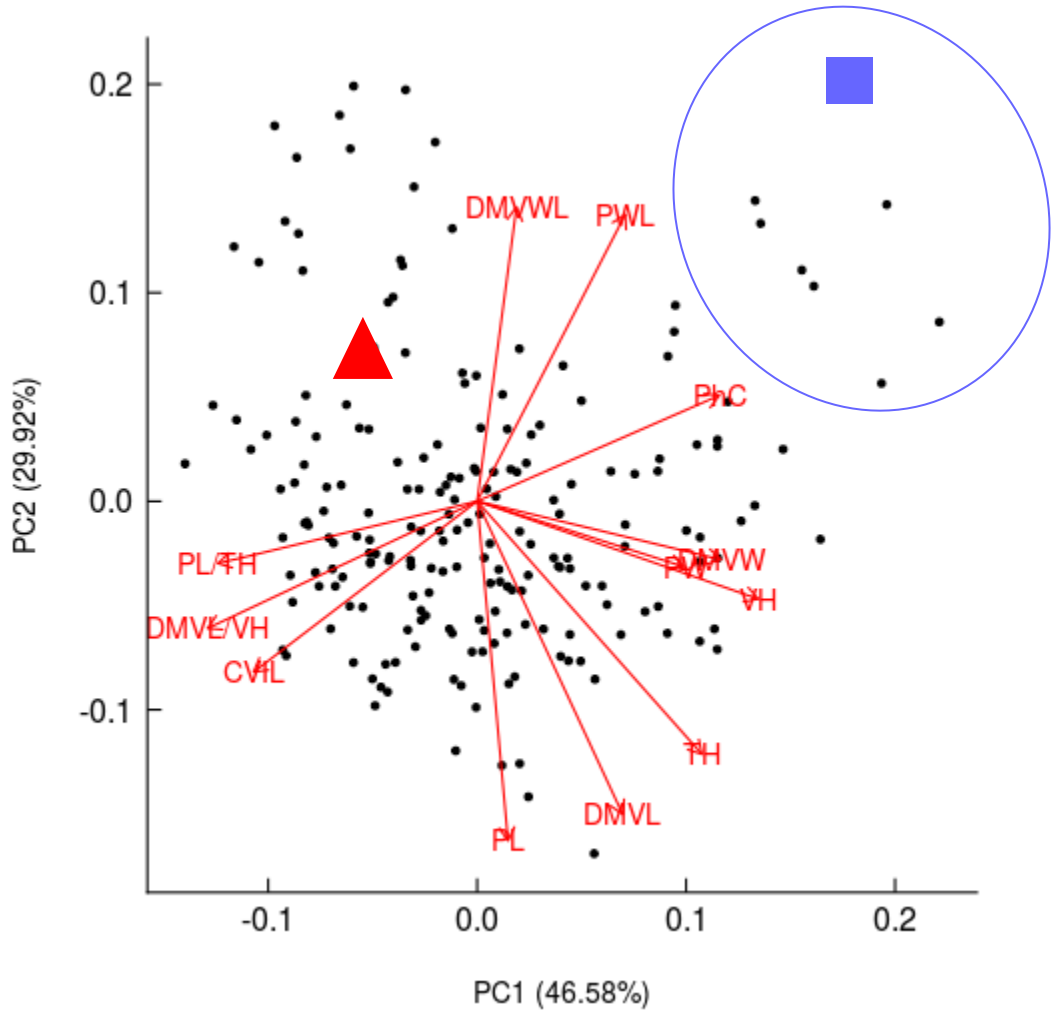

Figure 4.9: Internode phenotype principal component analysis biplot of first two principal components that together capture 76.5 % of variation in phenotype matrix from 12 internode morphology traits measured under water-deficit treatment. Red lines represent strength and direction of trait loadings based on eigenvectors (Table 4.3). Black circles represent predicted North American *Setaria viridis* accession values, blue square represent predicted *Setaria italica* B100 value, red triangle represents predicted *Setaria viridis* A10 value. Ellipse highlights six accessions most phenotypically similar to B100. CVIL=coefficient of variation of vegetative internode lengths, DMVL=distal-most vegetative internode length, DMVW=distal-most vegetative internode width, DMVWL=distal-most vegetative internode width:length, DMVL/VH=distal-most vegetative internode length as a fraction of vegetative height, PhC=phytomer count, PL=peduncle length, PW=peduncle width, PWL=peduncle length:width, PL/TH=peduncle length as a fraction of total height, TH=total height, VH=vegetative height

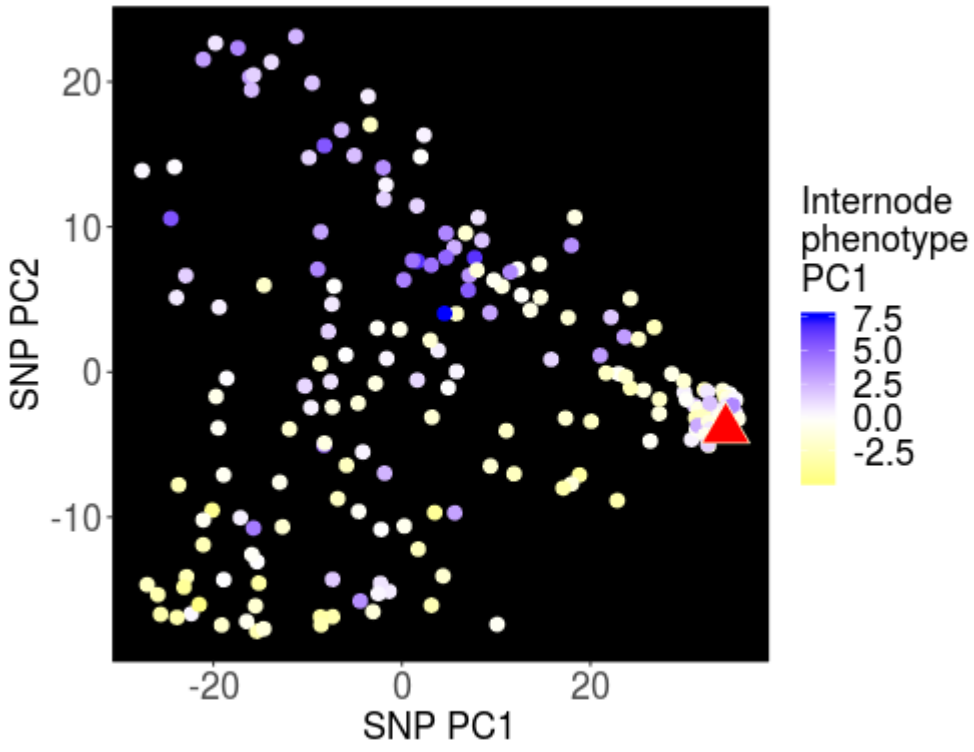

Figure 4.10: Population structure of North American *Setaria viridis* accessions visualized with PCA biplot of the first two principal components that capture 39.2 % of variation in the accession single nucleotide polymorphism (SNP) matrix. Circles represent accession SNP principal component values color scaled by internode phenotype principal component 1. Red triangle represents SNP principal component values for *Setaria viridis* A10 for use as a genetic reference.

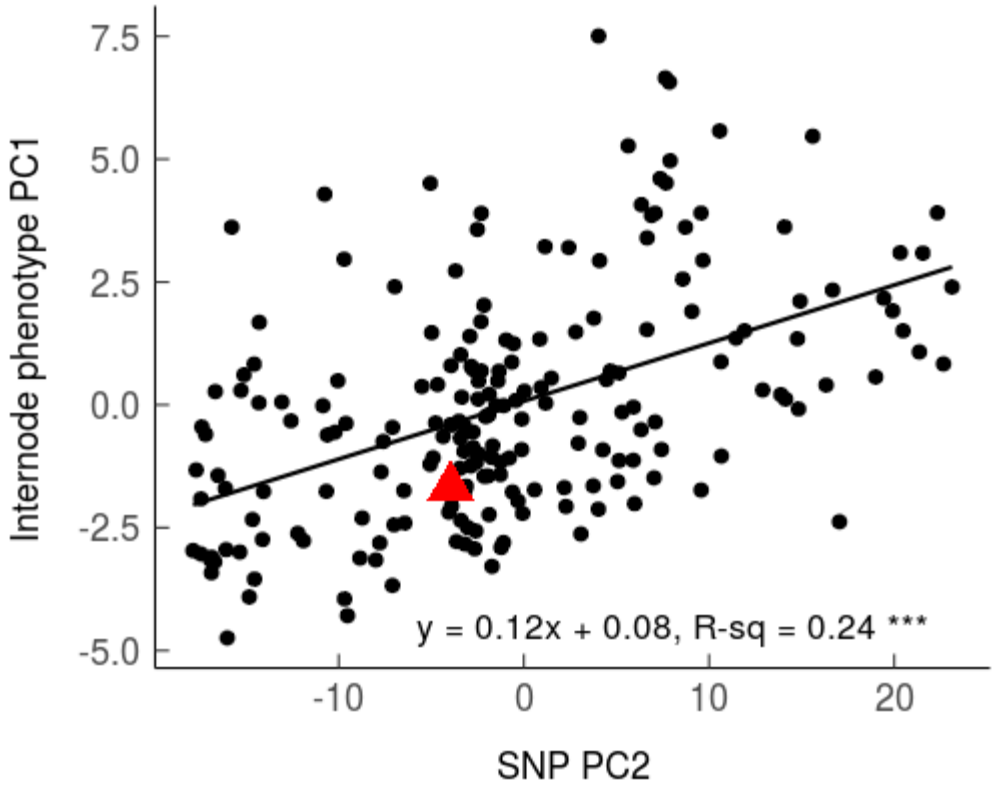

Figure 4.11: Correlation between internode phenotype PC1 and SNP PC2 with *Setaria viridis* A10 (red triangle) as a phenotypic and genetic reference. Black circles represent North American *Setaria viridis* accession values. Line represents linear regression between internode phenotype PC1 and SNP PC2 with R-squared and P-value displayed: ns > 0.05, * < 0.05, ** <0.01, *** < 0.001

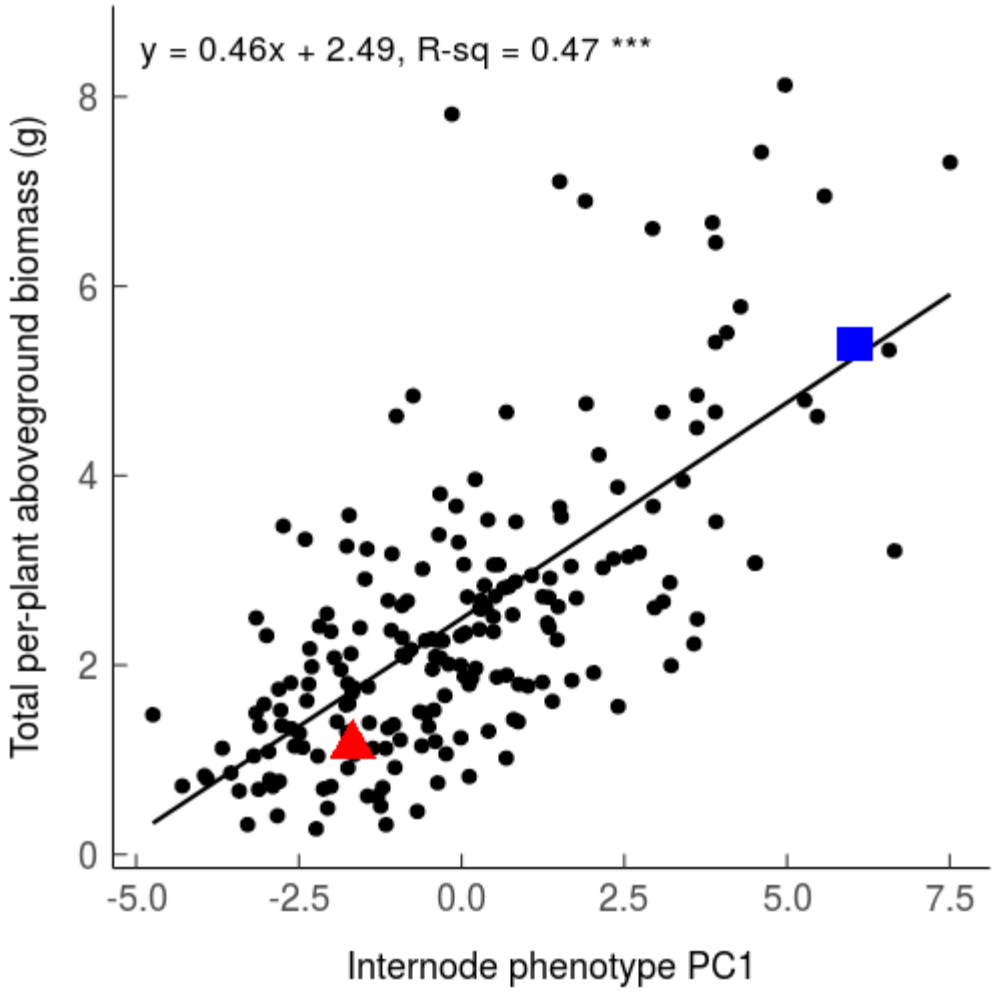

Figure 4.12: Correlation between internode phenotype PC1 and total per-plant aboveground biomass collected from water-deficit treatment with *Setaria viridis* A10 (red triangle) and *Setaria italica* B100 as phenotypic references. Black circles represent North American *Setaria viridis* accession values. Line represents linear regression between internode phenotype PC1 and total per-plant aboveground biomass with R-squared and P-value displayed: ns > 0.05, * < 0.05, ** <0.01, *** < 0.001

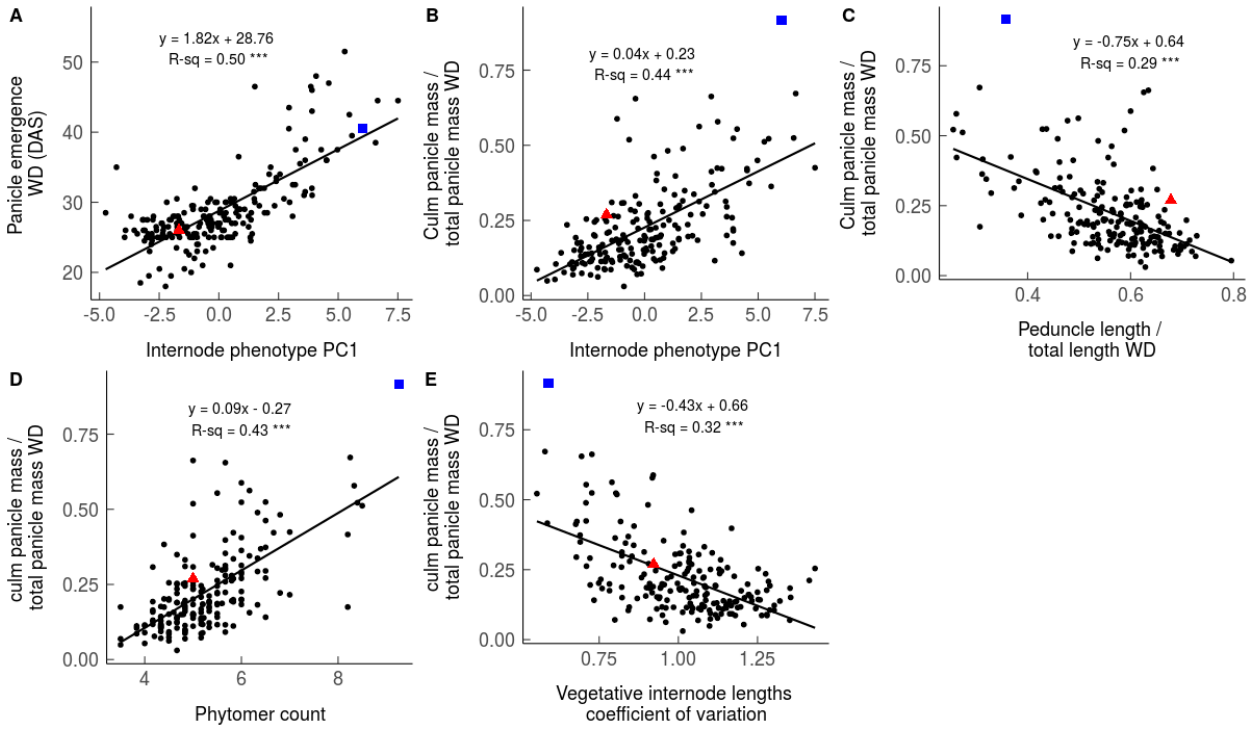

Figure 4.13 A-E: Correlations between internode traits and traits describing reproductive strategy collected from water-deficit treatment with *Setaria viridis* A10 (red triangles) and *Setaria italica* B100 as phenotypic references. Black circles represent North American *Setaria viridis* accession values. Lines represent linear regression between traits with R-squared and P-value displayed: ns > 0.05, * < 0.05, ** <0.01, *** < 0.001

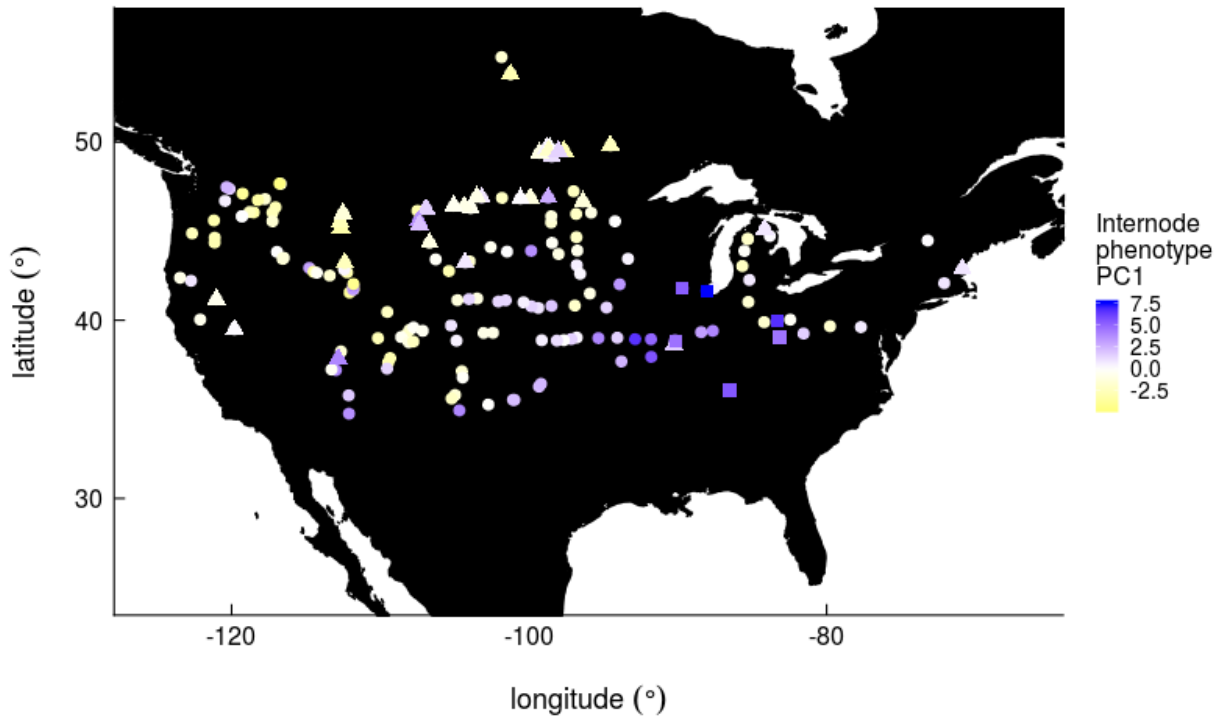

Figure 4.14: Geographical distribution of North American *Setaria viridis* accessions. Points represent site of accession collection color scaled by internode phenotype PC1. Squares represent accessions most phenotypically similar to *Setaria italica* B100, triangles represent accessions most genetically similar to *Setaria viridis* A10, circles represent unassigned accessions.

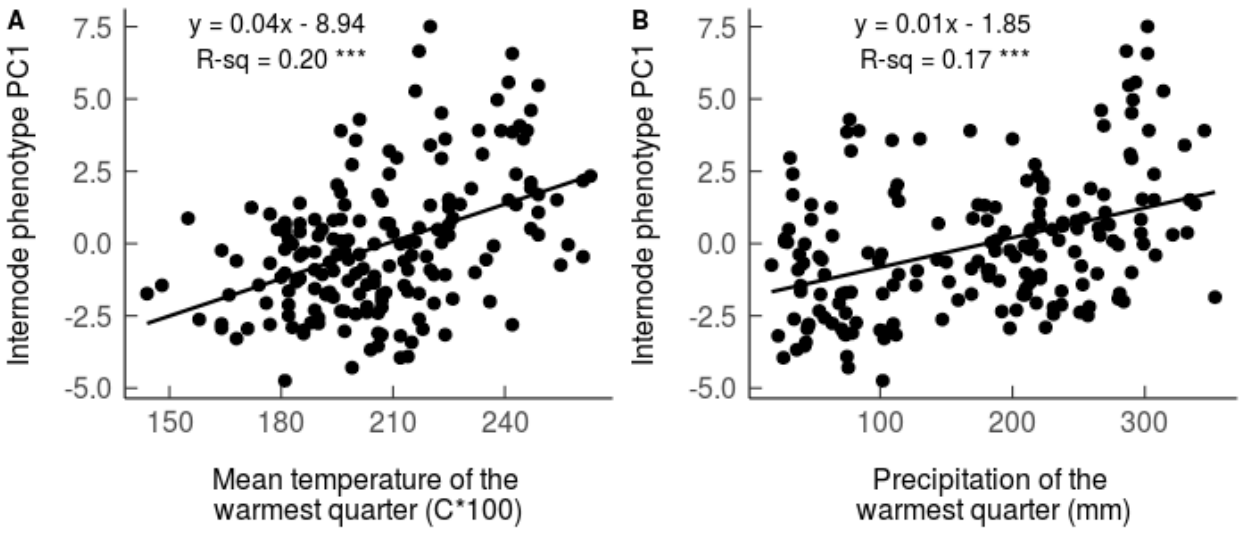

Figure 4.15: (Figure 4.15 A) Correlation between internode phenotype PC1 and the mean temperature of the warmest quarter at the site of accession collection. (Figure 4.15 B) Correlation between internode PC1 and the precipitation of the warmest quarter at the site of accession collection. Lines represent regression between internode phenotype PC1 and climate parameter with R-squared and P-value reported: ns > 0.05, * < 0.05, ** <0.01, *** < 0.001

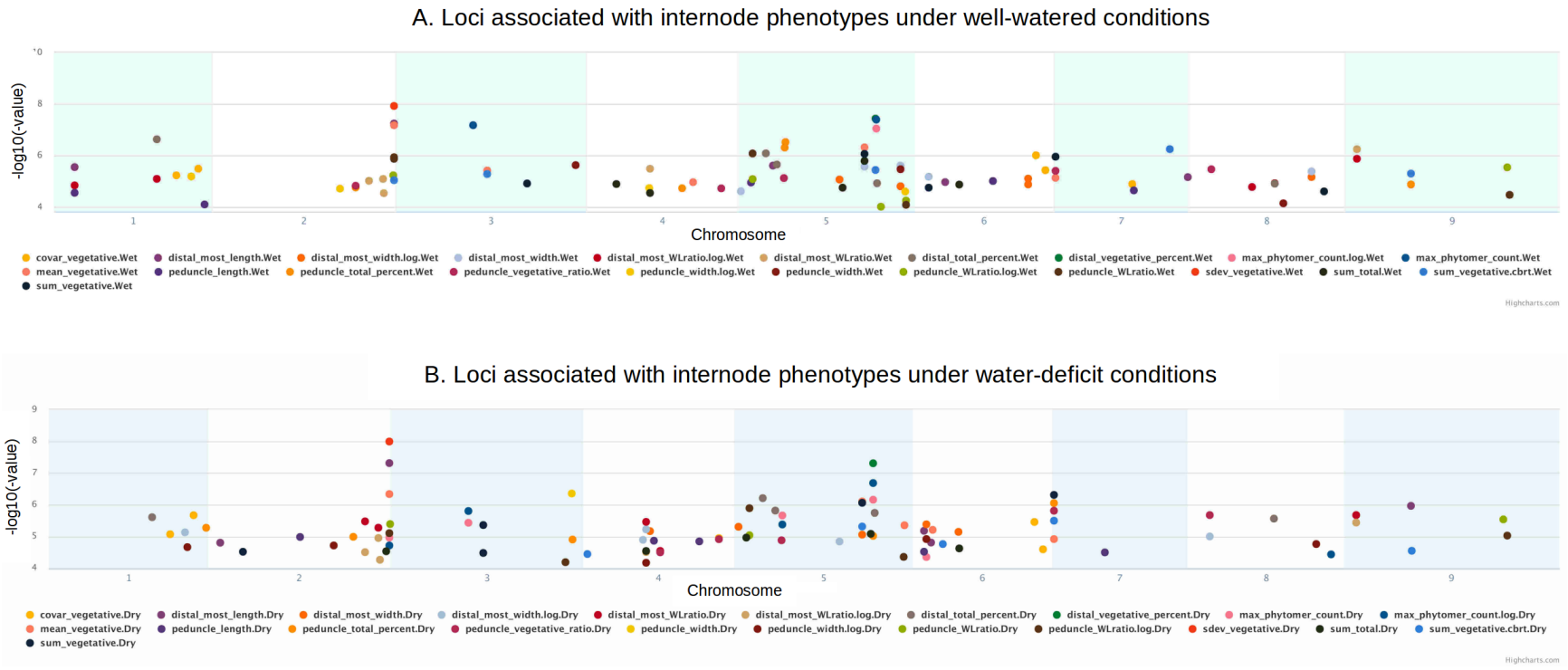

Figure 4.16: Genome wide association mapping of single nucleotide polymorphisms associated with internode phenotypes under well-watered (Figure 4.16 A) and water-deficit conditions (Figure 4.16 B).

Table 4.1: Trait definitions

Trait	Definition
2014 RIL experiment	
Observed height	Height directly measured in field or at destructive harvest; defined as distance between plant base and collar of the culm flag leaf (cm)
Predicted height	Height predicted from Gompertz growth function between 0 and 100 days after sowing (cm)
Days until panicle emergence	Number of days after sowing at which the panicle head was seen past the culm flag leaf in at least half of individuals in a genotype subplot (DAS)
Total growth period	Number of days after sowing until final height (DAS)
Elongation-specific growth	Total growth period – days until panicle emergence (DAS)
Proportion of the total growth period produced by elongation of the distal-most vegetative phytomer	Elongation-specific growth / total growth period (DAS / DAS)
Height at panicle emergence	Predicted height at panicle emergence (cm)
Final height	99 % of maximum predicted height (cm)
Elongation by distal-most vegetative phytomer	Final height – height at panicle emergence (cm)
Proportion of vegetative height produced by elongation of the distal-most vegetative phytomer	Elongation by distal-most vegetative phytomer / Final height (cm / cm)
2016 diversity panel experiment	
Phytomer count	Total number of internodes greater than 5 mm in length on culm
Coefficient of variation of vegetative internode lengths	Coefficient of variation calculated among vegetative internode lengths per culm per plant
Total height	Sum of culm internode lengths (mm)
Vegetative height	Sum of culm vegetative internode lengths (mm)
Peduncle length	Length of reproductive internode that supports the culm panicle (mm)
Peduncle width	Width of reproductive internode that supports the culm panicle (mm / mm)
Peduncle width:length	Peduncle width / peduncle length (mm / mm)
Peduncle length as a fraction of total height	Peduncle length / total height (mm / mm)
Distal-most vegetative internode length	Length of the last vegetative internode before the culm peduncle (mm)
Distal-most vegetative internode width	Width of the last vegetative internode before the culm peduncle (mm)
Distal-most vegetative internode width:length	Distal-most vegetative internode width / distal-most vegetative internode length (mm / mm)
Distal-most vegetative internode length as a fraction of vegetative height	Distal-most vegetative internode length / vegetative height

Table 4.2: Summary of QTL results detected for eight traits across two treatments. Marker name, location, proportion of genotypic variance explained, and relative additive effect for QTL identified for 13 measured traits at a 0.05 detection threshold are reported. PE.H=height at panicle emergence, pl.H=final height, d.H=elongation by distal-most vegetative phytomer, pr.H=proportion of vegetative height produced by elongation of the distal-most vegetative phytomer, PE.DAS=days after sowing until panicle emergence, pl.DAS=total growth period, d.DAS=elongation-specific growth period, pr.DAS=proportion of the total growth period produced by elongation of the distal-most vegetative phytomer

Trait abbreviation	Treatment	Marker	Chromosome	Position (cM)	LOD	Proportion of variance	Additive relative effect
d.DAS	dry	S8_4400594	8	38.63	3.93	10.41	0.10
d.DAS	dry	S2_47811870	2	119.77	4.21	11.20	-0.10
d.H	dry	S2_47321091	2	118.57	4.10	8.15	-0.12
d.H	dry	S3_11857473	3	55.99	4.22	8.40	-0.13
d.H	dry	S5_42085155	5	100.66	13.75	32.06	-0.25
d.H	wet	S2_47612492	2	119.29	5.46	9.77	-0.16
d.H	wet	S5_41800456	5	100.17	17.14	37.30	-0.33
d.H	wet	S2_14861996	2	37.47	3.98	6.96	0.25
PE.DAS	dry	S2_33713678	2	58.15	6.32	8.79	0.05
PE.DAS	dry	S5_43714262	5	109.70	9.43	13.80	0.07
PE.DAS	dry	S8_4742820	8	39.10	15.00	24.12	0.07
PE.DAS	dry	S3_16016173	3	64.26	5.55	7.61	0.04
PE.DAS	dry	S5_11951257	5	54.65	10.48	15.61	0.06
PE.DAS	wet	S3_19988515	3	70.16	8.53	10.89	0.05
PE.DAS	wet	S5_11951257	5	54.65	12.67	17.34	0.06
PE.DAS	wet	S2_36623538	2	68.22	7.61	9.57	0.05
PE.DAS	wet	S9_42122344	9	108.83	3.65	4.30	0.03
PE.DAS	wet	S5_43714208	5	109.70	9.02	11.61	0.06
PE.DAS	wet	S8_5027156	8	40.06	11.14	14.86	0.06
PE.H	dry	S2_35182461	2	62.31	4.54	7.49	0.09
PE.H	dry	S5_42757204	5	104.37	10.21	18.47	-0.23
PE.H	dry	S5_43714262	5	109.70	5.63	9.45	0.16
PE.H	dry	S8_4643788	8	39.10	3.83	6.24	0.07

Table 4.2 (cont.)

Trait abbreviation	Treatment	Marker	Chromosome	Position (cM)	LOD	Proportion of variance	Additive relative effect
PE.H	dry	S9_5686516	9	31.99	4.06	6.64	0.08
PE.H	wet	S8_3256297	8	36.41	4.86	6.37	0.07
PE.H	wet	S9_42122344	9	108.83	6.37	8.55	0.08
PE.H	wet	S5_28323105	5	67.63	6.09	8.14	0.08
PE.H	wet	S2_33713678	2	58.15	5.16	6.80	0.08
PE.H	wet	S2_43563669	2	90.65	3.36	4.30	0.06
PE.H	wet	S5_41999990	5	100.41	16.58	26.47	-0.16
PE.H	wet	S5_44003086	5	115.13	4.21	5.45	0.07
pl.DAS	dry	S2_44073549	2	93.53	3.83	7.32	0.05
pl.DAS	dry	S8_4643788	8	39.10	7.23	14.61	0.07
pl.DAS	dry	S2_47811870	2	119.77	5.94	11.75	-0.07
pl.DAS	dry	S5_11863225	5	53.90	4.74	9.20	0.06
pl.DAS	wet	S5_11951257	5	54.65	3.41	9.21	0.06
pl.DAS	wet	S8_4742820	8	39.10	3.98	10.83	0.07
pl.H	dry	S5_41800456	5	100.17	9.10	25.09	-0.13
pl.H	wet	S1_36166226	1	82.03	4.98	3.68	0.05
pl.H	wet	S2_43563669	2	90.65	7.19	5.51	0.07
pl.H	wet	S2_46820675	2	113.85	9.28	7.38	-0.08
pl.H	wet	S2_14861996	2	37.47	4.83	3.56	0.10
pl.H	wet	S2_34544107	2	61.37	7.03	5.38	0.07
pl.H	wet	S5_28323105	5	67.63	3.13	2.25	0.04
pl.H	wet	S5_41800456	5	100.17	32.55	38.97	-0.18
pl.H	wet	S8_3376258	8	36.65	4.56	3.35	0.05
pl.H	wet	S4_11221439	4	48.09	6.15	4.64	-0.06
pl.H	wet	S9_42612418	9	111.72	5.66	4.23	0.05
pl.H	wet	S9_9448732	9	40.40	4.23	3.09	0.05
pr.DAS	dry	S2_47811870	2	119.77	4.23	11.32	-0.06
pr.DAS	dry	S6_33052891	6	73.84	3.55	9.40	-0.05
pr.DAS	wet	S5_41265928	5	97.19	4.94	11.95	-0.09

Table 4.2 (cont.)

Trait abbreviation	Treatment	Marker	Chromosome	Position (cM)	LOD	Proportion of variance	Additive relative effect
pr.DAS	wet	S2_47766857	2	119.77	3.55	8.38	-0.08
pr.H	dry	S3_17274073	3	66.49	6.55	11.61	-0.10
pr.H	dry	S5_25139375	5	61.08	3.43	5.78	-0.07
pr.H	dry	S5_42113193	5	100.90	5.33	9.27	-0.10
pr.H	dry	S2_41724219	2	83.19	3.53	5.96	-0.08
pr.H	dry	S9_5497941	9	31.30	5.16	8.95	-0.10
pr.H	dry	S7_28851780	7	76.62	5.42	9.43	-0.09
pr.H	wet	S5_36742284	5	89.13	4.94	14.52	-0.16

Table 4.3: Principal component analysis of internode phenotypes generated from image analysis of 2016 diversity panel samples. Trait loadings based on eigenvectors are reported for each trait within each principal component (PC). Eigenvalue for each PC is reported.

Trait	Abbreviation	PC1	PC2	PC3
Phytomer count	PhC	0.33	0.15	0.20
Phytomer length (mm)	PL	0.04	-0.47	-0.27
Phytomer width (mm)	PW	0.29	-0.09	-0.53
Phytomer width/length	PWL	0.20	0.40	-0.17
Total internode height	TH	0.31	-0.35	0.00
Vegetative internode height	VH	0.39	-0.14	0.19
Coefficient of variation of vegetative internode length	CVIL	-0.31	-0.24	-0.07
Distal-most vegetative internode length	DMVL	0.20	-0.43	0.10
Distal-most vegetative internode width	DMVW	0.34	-0.08	-0.43
Distal-most vegetative internode width:length	DMVWL	0.05	0.41	-0.43
Peduncle length / total internode height	PL/TH	-0.36	-0.09	-0.35
Distal-most vegetative internode length / vegetative internode height	DMVL/VH	-0.37	-0.18	-0.15
Eigenvalue		2.36	1.89	1.29

Table 4.4: Summary of GWAS results detected for 12 traits measured under well-watered and water-deficit treatments. SNP identity, model added P-value, model, and trait names are reported.

SNP	Model added P-value	Model	Trait
5_36480922	4.94E-08	Mbonf	distal_vegetative_percent.Dry
2_24268073	1.03E-05	Mbonf	peduncle_length.Dry
4_18536974	1.35E-05	Mbonf	peduncle_length.Dry
4_30521471	1.42E-05	Mbonf	peduncle_length.Dry
6_3013700	2.99E-05	Mbonf	peduncle_length.Dry
7_13982184	3.15E-05	Mbonf	peduncle_length.Dry
2_47734914	4.04E-06	Mbonf	peduncle_WLratio.Dry
5_4023617	9.07E-06	Mbonf	peduncle_WLratio.Dry
9_41939928	2.88E-06	Mbonf	peduncle_WLratio.Dry
2_47690022	1.02E-08	Mbonf	sdev_vegetative.Dry
5_36480922	3.67E-08	Mbonf	distal_vegetative_percent.Wet
5_36517297	8.97E-08	Mbonf	max_phytomer_count.log.Wet
3_20450110	6.62E-08	Mbonf	max_phytomer_count.Wet
5_36517297	4.02E-08	Mbonf	max_phytomer_count.Wet
2_47690022	1.19E-08	Mbonf	sdev_vegetative.Wet
1_27156025	2.46E-06	MaxCof	distal_total_percent.Dry
1_27156025	0.000000233	MaxCof	distal_total_percent.Wet
2_47571711	7.80E-06	MaxCof	peduncle_WLratio.log.Dry
2_47571711	0.00000577	MaxCof	peduncle_WLratio.log.Wet
2_47679839	4.88E-08	MaxCof	distal_most_length.Dry
2_47679839	4.60E-07	MaxCof	mean_vegetative.Dry
2_47679839	0.00000895	MaxCof	sum_vegetative.cbrt.Wet
4_16559096	5.94E-06	MaxCof	distal_most_width.log.Dry
4_16559096	6.67E-05	MaxCof	peduncle_width.log.Dry
4_16559096	0.0000181	MaxCof	peduncle_width.log.Wet
4_35508720	1.21E-05	MaxCof	peduncle_vegetative_ratio.Dry
4_35508720	0.0000185	MaxCof	peduncle_vegetative_ratio.Wet
5_33508625	7.86E-07	MaxCof	mean_vegetative.Dry
5_33508625	0.000000477	MaxCof	mean_vegetative.Wet
5_33508625	0.0000016	MaxCof	sum_total.Wet

Table 4.4 (cont.)

SNP	Model added P-value	Model	Trait
5_36480922	2.07E-07	MaxCof	max_phytomer_count.log.Dry
5_36480922	0.0000036	MaxCof	sum_vegetative.cbrt.Wet
5_36517297	8.97E-08	Mbonf	max_phytomer_count.log.Wet
5_36517297	9.54E-06	MaxCof	peduncle_total_percent.Dry
5_36899398	1.79E-06	MaxCof	distal_total_percent.Dry
5_36899398	0.0000118	MaxCof	distal_total_percent.Wet
5_4023617	1.28E-06	MaxCof	peduncle_WLratio.log.Dry
5_4023617	0.0000081	MaxCof	peduncle_WLratio.log.Wet
5_44487383	4.37E-05	MaxCof	peduncle_WLratio.log.Dry
5_44487383	0.0000549	MaxCof	peduncle_WLratio.log.Wet
5_7488817	6.18E-07	MaxCof	distal_total_percent.Dry
5_7488817	0.000000817	MaxCof	distal_total_percent.Wet
6_31910765	3.48E-06	MaxCof	covar_vegetative.Dry
6_31910765	0.00000097	MaxCof	covar_vegetative.Wet
7_545122	1.20E-05	MaxCof	mean_vegetative.Dry
7_545122	0.00000727	MaxCof	mean_vegetative.Wet
7_562186	8.83E-07	MaxCof	peduncle_total_percent.Dry
7_562186	1.54E-06	MaxCof	peduncle_vegetative_ratio.Dry
7_562186	0.00000389	MaxCof	peduncle_vegetative_ratio.Wet
8_22673025	0.0000117	MaxCof	distal_most_WLratio.log.Wet
8_22673025	2.72E-06	MaxCof	distal_total_percent.Dry
8_22673025	0.0000122	MaxCof	distal_total_percent.Wet
8_5912813	2.11E-06	MaxCof	peduncle_vegetative_ratio.Dry
8_5912813	0.00000337	MaxCof	peduncle_vegetative_ratio.Wet
9_3306218	3.62E-06	MaxCof	distal_most_WLratio.log.Dry
9_3306218	0.00000132	MaxCof	distal_most_WLratio.log.Wet
9_42901641	9.32E-06	MaxCof	peduncle_WLratio.log.Dry
9_42901641	0.00000284	MaxCof	peduncle_WLratio.log.Wet

Table 4.5. Candidate genes for internode morphology and elongation traits in *Setaria viridis*

Trait	Gene ID	Arabidopsis Description	Rice Description	Keyword	Notes
Distal-most vegetative internode length as a fraction of total height WD	Sevir.5G337000	ABC transporter family protein	ABC transporter, ATP-binding protein, putative, expressed	ABC	(Avila 2016) ATP-binding cassette phosphoglyco protein, internode elongation Zm
Distal-most vegetative internode length as a fraction of total height WW	Sevir.5G337000	ABC transporter family protein	ABC transporter, ATP-binding protein, putative, expressed	ABC	
Mean vegetative internode length WD	Sevir.5G290400	ABC-2 type transporter family protein	ABC-2 type transporter domain containing protein, expressed	ABC	
Mean vegetative internode length WW	Sevir.5G290400	ABC-2 type transporter family protein	ABC-2 type transporter domain containing protein, expressed	ABC	
Total height WW	Sevir.5G290400	ABC-2 type transporter family protein	ABC-2 type transporter domain containing protein, expressed	ABC	
cube root(Vegetative height WD)	Sevir.5G290400	ABC-2 type transporter family protein	ABC-2 type transporter domain containing protein, expressed	ABC	
log(Peduncle width WD)	Sevir.4G134100	ABC transporter family protein	White-brown complex homolog protein, putative, expressed	ABC	
log(Distal-most vegetative internode width WD)	Sevir.4G134100	ABC transporter family protein	White-brown complex homolog protein, putative, expressed	ABC	
log(Peduncle width WW)	Sevir.4G134100	ABC transporter family protein	White-brown complex homolog protein, putative, expressed	ABC	

Table 4.5 (cont.)

Trait	Gene ID	Arabidopsis Description	Rice Description	Keyword	Notes
Mean vegetative internode length WD	Sevir.5G290300	Kelch repeat-containing F-box family protein	expressed_protein	F Box	(Ayano 2014) F-box, E3 ligase, GA signaling factor, part of Os ethylene response
Mean vegetative internode length WW	Sevir.5G290300	Kelch repeat-containing F-box family protein	expressed_protein	F Box	
Total height WW	Sevir.5G290300	Kelch repeat-containing F-box family protein	expressed_protein	F Box	
cube root(Vegetative height WD)	Sevir.5G290300	Kelch repeat-containing F-box family protein	expressed_protein	F Box	
Distal-most vegetative internode length as a fraction of total height WW	Sevir.1G199700	Galactose oxidase/kelch repeat superfamily protein	OsFBK8: F-box domain and kelch repeat containing protein, expressed	F Box	
Distal-most vegetative internode length as a fraction of total height WD	Sevir.1G199700	Galactose oxidase/kelch repeat superfamily protein	OsFBK8: F-box domain and kelch repeat containing protein, expressed	F Box	
Distal-most vegetative internode length as a fraction of total height WW	Sevir.5G336800	F-box family protein	OsFBX26: F-box domain containing protein: expressed	F Box	
Distal-most vegetative internode length as a fraction of total height WW	Sevir.5G336800	F-box family protein	OsFBX26: F-box domain containing protein: expressed	F Box	

Table 4.5 (cont.)

Trait	Gene ID	Arabidopsis Description	Rice Description	Keyword	Notes
log(Phytomer count WD)	Sevir.5G329800	HD-ZIP IV family of homeobox-leucine zipper protein with lipid-binding START domain	Homeobox and START domains containing protein, putative, expressed	HDZIP	(Todaka 2012) HD-ZIP, phytochrome regulation in Os internode elongation response to stress
cube root(Vegetative height WW)	Sevir.5G329800	HD-ZIP IV family of homeobox-leucine zipper protein with lipid-binding START domain	Homeobox and START domains containing protein, putative, expressed	HDZIP	
Distal-most vegetative internode length WD	Sevir.2G454700	Leucine-rich repeat protein kinase family protein	MRH1, putative, expressed	LRR	(Yamamuro 2000) leucine rich repeat receptor kinase, Os internode elongation
Mean vegetative internode length WD	Sevir.2G454700	Leucine-rich repeat protein kinase family protein	MRH1, putative, expressed	LRR	
Peduncle width:length WD	Sevir.2G454700	Leucine-rich repeat protein kinase family protein	MRH1, putative, expressed	LRR	
Standard deviation of vegetative internode lengths WD	Sevir.2G454700	Leucine-rich repeat protein kinase family protein	MRH1, putative, expressed	LRR	
Standard deviation of vegetative internode lengths WW	Sevir.2G454700	Leucine-rich repeat protein kinase family protein	MRH1, putative, expressed	LRR	
cube root (Vegetative height WW)	Sevir.2G454700	Leucine-rich repeat protein kinase family protein	MRH1, putative, expressed	LRR	

Table 4.5 (cont.)

Trait	Gene ID	Arabidopsis Description	Rice Description	Keyword	Notes
Distal-most vegetative internode length as a fraction of total height WW	Sevir.5G093600	Protein kinase superfamily protein	Ser/Thr protein kinase, putative, expressed	Ser/Thr	(Hilley 2017) serine/threonine kinase, Dw1, Sb internode length regulation
Distal-most vegetative internode length as a fraction of total height WD	Sevir.5G093400	Protein kinase superfamily protein	Ser/Thr protein kinase, putative, expressed	Ser/Thr	
Distal-most vegetative internode length as a fraction of total height WD	Sevir.5G093600	PR5-like receptor kinase	Ser/Thr protein kinase, putative, expressed	Ser/Thr	
Distal-most vegetative internode length as a fraction of total height WW	Sevir.5G093400	Protein kinase superfamily protein	Ser/Thr protein kinase, putative, expressed	Ser/Thr	
Distal-most vegetative internode length as a fraction of total height WW	Sevir.5G093600	PR5-like receptor kinase	Ser/Thr protein kinase, putative, expressed	Ser/Thr	
Peduncle length WD	Sevir.4G143700	Type one protein phosphatase 1	Ser/Thr protein phosphatase family protein, putative, expressed	Ser/Thr	
log(Distal-most vegetative internode length WD)	Sevir.4G133900	Nucleotide-sugar transporter family protein	UAA transporter family domain containing protein, expressed	sugar	(Martin 2016) Sv nucleotide sugar transporter
log(Distal-most vegetative internode width WD)	Sevir.4G133900	Nucleotide-sugar transporter family protein	UAA transporter family domain containing protein, expressed	sugar	

Table 4.5 (cont.)

Trait	Gene ID	Arabidopsis Description	Rice Description	Keyword	Notes
log(Peduncle width WW)	Sevir.4G133900	Nucleotide-sugar transporter family protein	UAA transporter family domain containing protein, expressed	sugar	
Distal-most vegetative internode length WD	Sevir.2G454600	Ubiquitin activating enzyme 2	Ubiquitin-activating enzyme, putative, expressed	ubiquitin	(Hilley 2016) E3 ubiquitin ligase, syntaxin degradation, Sb internode length
Mean vegetative internode length WD	Sevir.2G454600	Ubiquitin activating enzyme 2	Ubiquitin-activating enzyme, putative, expressed	ubiquitin	
standard deviation(Vegetative internode lengths WD)	Sevir.2G454600	Ubiquitin activating enzyme 2	Ubiquitin-activating enzyme, putative, expressed	ubiquitin	
standard deviation(Vegetative internode lengths WW)	Sevir.2G454600	Ubiquitin activating enzyme 2	Ubiquitin-activating enzyme, putative, expressed	ubiquitin	
cube root (Vegetative height WW)	Sevir.2G454600	Ubiquitin activating enzyme 2	Ubiquitin-activating enzyme, putative, expressed	ubiquitin	(Avila 2016) WD40, auxin signaling Zm
Peduncle width:length WD	Sevir.2G455300	Transducin family protein /WD-40 repeat family protein	expressed_protein	WD40	
Standard deviation of vegetative internode lengths WD	Sevir.2G455300	Transducin family protein /WD-40 repeat family protein	expressed_protein	WD40	
Standard deviation of vegetative internode lengths WW	Sevir.2G455300	Transducin family protein /WD-40 repeat family protein	expressed_protein	WD40	

REFERENCES

Ayano M, Kani T, Kojima M, Sakakibara H, Kitaoka T, Kuroha T, Angeles-Shim RB, Kitano H, Nagai K, Ashikari M (2014) Gibberellin biosynthesis and signal transduction is essential for internode elongation in deepwater rice. Plant, Cell Environ **37**: 2313–2324

Banan D, Paul RE, Feldman MJ, Holmes MW, Schlake H, Baxter I, Jiang H, Leakey ADB (2018) High-fidelity detection of crop biomass quantitative trait loci from low-cost imaging in the field. 1–8

Busemeyer L, Ruckelshausen A, Möller K, Melchinger AE, Alheit K V, Maurer HP, Hahn V, Weissmann E a, Reif JC, Würschum T (2013) Precision phenotyping of biomass accumulation in triticale reveals temporal genetic patterns of regulation. Sci Rep **3**: 2442

Dorp D Van, Daleboudt C (1996) Seed dispersal capacity of six perennial grassland species measured in a wind tunnel at varying wind speed and height. **1963**: 1956–1963

Doust AN, Kellogg EA, Devos KM, Bennetzen JL (2009) Foxtail Millet: A Sequence-Driven Grass Model System. Plant Physiol **149**: 137–141

Fahlgren N, Ellsworth PZ, Cousins AB, Baxter I, Gehan MA, Feldman MJ (2018) Components of Water Use Efficiency Have Unique Genetic Signatures in the Model C 4 Grass Setaria . Plant Physiol **178**: 699–715

Feldman MJ, Paul RE, Banan D, Barrett JF, Sebastian J, Dinneny R, Yee M, Jiang H, Lipka AE, Brutnell TP, et al (2017) Time dependent genetic analysis links field and controlled environment phenotypes in the model C 4 grass Setaria. PLoS Genet **13**: 1–31

Fournier C (2001) A functional – structural model of elongation of the grass leaf and its relationships with the phyllochron. 881–894

Fournier C, Andrieu B (2000) Dynamics of the elongation of internodes in maize (Zea mays L.): Analysis of phases of elongation and their relationships to phytomer development. Ann Bot **86**: 551–563

Gamon JA, Pearcy RW (1989) Leaf movement, stress avoidance and photosynthesis in Vitis californica. Oecologia **79**: 475–481

Haase P, Pugnaire FI, Incoll LD (1995) Seed production and dispersal in the semi-arid tussock grass Stipa tenacissima L . during masting. 55–65

Hemaprabha G, Swapna S, Lavanya DL, Sajitha B, Venkataramana S (2013) Evaluation of Drought Tolerance Potential of Elite Genotypes and Progenies of Sugarcane (Saccharum sp. hybrids). Sugar Tech **15**: 9–16

Hilley JL, Weers BD, Truong SK, McCormick RF, Mattison AJ, McKinley BA, Morishige DT, Mullet JE (2017) Sorghum Dw2 Encodes a Protein Kinase Regulator of Stem Internode Length. Sci Rep **7**: 1–13

Hodge JG, Kellogg EA (2016) Abscission zone development in Setaria viridis and its domesticated relative, Setaria italica 1. **103**: 998–1005

Huang P, Feldman M Genetic Diversity and Geographic Distribution of North American Setaria viridis Populations. 45–59

Huang P, Feldman M, Schroder S, Bahri BA, Diao X, Zhi H, Estep M, Baxter I, Devos KM, Kellogg EA (2014) Population genetics of Setaria viridis, a new model system. Mol Ecol **23**: 4912–4925

Kirby EJM, Appleyard M, Simpson NA (1994) Co-ordination of stem elongation and Zadoks growth stages with leaf emergence in wheat and barley. J Agric Sci **122**: 21–29

Ku L, Cao L, Wei X, Su H, Tian Z, Guo S, Zhang L, Ren Z, Wang X, Zhu Y, et al (2015) Genetic dissection of internode length above the uppermost ear in four RIL populations of maize (Zea mays L.). G3 (Bethesda) **5**: 281–9

Li W, Zhang B, Li R, Chang X, Jing R (2015) Favorable alleles for Stem water-soluble carbohydrates identified by association analysis contribute to grain weight under drought stress conditions in wheat. PLoS One **10**: 1–15

Liu Y, Xu Y, Xiao J, Ma Q, Li D, Xue Z, Chong K (2011) OsDOG, a gibberellin-induced A20/AN1 zinc-finger protein, negatively regulates gibberellin-mediated cell elongation in rice. J Plant Physiol **168**: 1098–1105

Martin AP, Palmer WM, Brown C, Abel C, Lunn JE, Furbank RT, Grof CPL (2016) A developing Setaria viridis internode: an experimental system for the study of biomass generation in a C4 model species. Biotechnol Biofuels **9**: 45

Mauro-herrera M, Doust AN (2016) Development and Genetic Control of Plant Architecture and Biomass in the Panicoid Grass , Setaria. 1–27

Mccormick RF, Truong SK, Mullet JE (2016) 3D sorghum reconstructions from depth images enable identification of quantitative trait loci regulating plant architecture. 1–29

McGaughey SA, Osborn HL, Chen L, Pegler JL, Tyerman SD, Furbank RT, Byrt CS, Grof CPL (2016) Roles of Aquaporins in Setaria viridis Stem Development and Sugar Storage. Front Plant Sci **7**: 1–13

Mckown AD, Guy RD, Klápště J, Geraldes A, Friedmann M, Cronk QCB, El-kassaby YA, Mansfield SD, Douglas CJ, Geraldes A, et al (2018) Geographical and environmental gradients shape phenotypic trait variation and genetic structure in Populus trichocarpa.

Morrison TA, Kessler JR, Burton DR (1994) Maize internodes elongation patterns. Crop Sci **34**: 1055–1060

Muthurajan R, Shobbar ZS, Jagadish SVK, Bruskiewich R, Ismail A, Leung H, Bennett J (2011) Physiological and proteomic responses of rice peduncles to drought stress. Mol Biotechnol **48**: 173–182

Nagai K, Kuroha T, Ayano M, Kurokawa Y, Angeles-Shim RB, Shim J-H, Yasui H, Yoshimura A, Ashikari M (2012) Two novel QTLs regulate internode elongation in deepwater rice during the early vegetative stage. Breed Sci **62**: 178–185

Nakamura S, Nakajima N, Nitta Y, Goto Y (2011) Analysis of Successive Internode Growth in Sweet Sorghum Using Leaf Number as a Plant Age Indicator. 14:

Nonami H, Boyer JS (1990) Wall extensibility and cell hydraulic conductivity decrease in enlarging stem tissues at low water potentials. Plant Physiol **93**: 1610–1619

Pazos GE, Greene DF, Katul G, Soons MB, Brown B, Madryn UP (2013) Seed dispersal by wind : towards a conceptual framework of seed abscission and its contribution to long-distance dispersal. 889–904

Pickup M, Barrett SCH (2012) Reversal of height dimorphism promotes pollen and seed dispersal in a wind-pollinated dioecious plant. 245–248

Qi W, Sun F, Wang Q, Chen M, Huang Y, Feng YQ, Luo X, Yang J (2011) Rice ethylene-response AP2/ERF factor OsEATB restricts internode elongation by down-regulating a gibberellin biosynthetic gene. Plant Physiol **157**: 216–228

Schröder S, Bahri BA, Eudy DM, Layton DJ, Kellogg EA, Devos KM (2016) Genetic diversity and origin of North American green foxtail [Setaria viridis (L.) Beauv.] accessions. Genet Resour Crop Evol 1–12

Song Y, Birch C, Rui Y, Hanan J (2015) Allometric Relationships of Maize Organ Development under Different Water Regimes and Plant Densities. **18**: 1–10

Tardieu F, Reymond M, Muller B, Granier C, Simonneau T, Sadok W, Welcker C (2005) Linking physiological and genetic analyses of the control of leaf growth under changing environmental conditions. Aust J Agric Res **56**: 937–946

Vidal T, Dillmann C, Andrieu B (2018) A coordination model captures the dynamics of organ extension in contrasted maize phenotypes. 2018 6th Int Symp Plant Growth Model Simulation, Vis Appl 126–133

Wolfe MD, Tonsor SJ (2014) Adaptation to spring heat and drought in northeastern Spanish Arabidopsis thaliana. 323–334

Yang F, Gong XY, Liu HT, Schäufele R, Schnyder H (2016) Effects of nitrogen and vapour pressure deficit on phytomer growth and development in a C_4 grass. AoB Plants **8**: plw075

CHAPTER 5
CONCLUSIONS

SUMMARY

This thesis utilized a combination of imaging and direct measurement techniques to characterize phenotypic and genetic variation in the aboveground architectural responses of *Setaria viridis* to drought stress. Architecture influences plant productivity, mediates interactions with the local environment, and provides a framework for determining specific crop improvement targets. Traits associated with domestication such as resistance to lodging and greater reproductive allocation have resulted from manipulation of aboveground architecture. However, manipulation of architecture to improve stress tolerance has historically received less attention. In this thesis, architecture traits such as leaf rolling and internode elongation were assessed in reference to productivity responses to water-deficit to evaluate their stress tolerance capacity. The genotype-to-phenotype associations revealed from these studies represent a preliminary step in accelerating the improvement of next generation C_4 grass biofuel feedstocks. These feedstocks must be highly productive and stress tolerant in order to serve as a viable and sustainable option for meeting the increasing demand for food, fuel, and other industrial products.

Chapter 2 tested the ability of a hemispherical canopy imaging system to capture the same aboveground productivity genotype-to-phenotype associations as conventional harvest measures. Direct assessment of plant productivity and architecture is difficult due to the time consuming and destructive nature of conventional measurement collection. Therefore estimates of Plant Area Index (PAI) generated from analysis of below-canopy hemispherical images were used to assess variation in productivity and architecture across a *Setaria viridis* x *italica* recombinant inbred line (RIL) population and detect quantitative trait loci (QTL). Results showed that PAI estimated from canopy hemispherical images correlated significantly with directly measured traits describing biomass. Additionally, QTL detected for PAI were co-located with QTL detected for directly measured traits describing biomass. However, QTL detected for PAI did not correlate well with or have genetic co-localization with QTL detected for traits that described the bushiness or partitioning of aboveground biomass. These results suggested that canopy hemispherical imaging could serve as an efficient means for non-destructively

phenotyping productivity in the field. However, more targeted approaches would be needed to understand how specific aspects of plant architecture can be modified to improve productivity responses to drought stress. With this in mind, Chapters 3 and 4 focused on drought induced changes in leaf and internode architecture.

As a reversible means of reducing transpiration and photoinhibition, leaf rolling has the potential for improving drought tolerance. However, a number of questions remain regarding its efficacy as a drought tolerance trait in C_4 grasses before it can be more widely adopted. Therefore, Chapter 3 sought to characterize the potential adaptive significance of leaf rolling in a North American *Setaria viridis* diversity panel by combining canopy hemispherical imaging at multiple timepoints with direct measures of leaf morphology. This approach revealed that, in response to water-deficit, leaves became more folded and upright at midday while a greater proportion of light penetrated through the canopy. A visual leaf rolling score was correlated with these diurnal canopy adjustments and effectively captured variation across the population. The visual score was used to identify accessions that exhibited a high degree of leaf rolling as well as the set of closest related accessions that exhibited low-to-no leaf rolling. Despite being larger, having prolonged growth, and potentially experiencing more drought stress, high rolling accessions lost a similar proportion of vegetative biomass in response to water-deficit treatment compared to their low-to-non rolling closest relatives. Together, these results are consistent with leaf rolling as an adaptive trait for accessions that need to conserve water during moderate or variable drought conditions in order to produce more growth over longer periods.

Chapter 4 examined internode morphology and elongation responses to water-deficit treatment using both RIL and accession populations. Internodes are the dominant structural element of the stem and understanding their responses to water-deficit is especially important in the context of maximizing and maintaining productivity in next generation C_4 grass biofuel feedstocks. From a whole plant perspective, internodes influence the performance of photosynthetic and reproductive organs and can be interpreted as the scaffolding for the results described in the previous two data chapters. The application of a Gompertz growth function anchored by developmental landmarks showed that elongation of the distal-most vegetative internode produced a greater proportion of total height in responses to water-deficit despite an overall reduction in vegetative growth. The peduncle, or reproductive internode, displayed increased elongation in response to water-deficit. Together, these stress responses suggest that

internode elongation can serve as a means to recover vegetative growth lost earlier in development to water-deficit and ensure the elevation of reproductive structures. Within the North American accession population, internode morphology was significantly correlated with traits related to reproductive strategy and clustered with the geography and climate at the site of collection. These results show that internode morphology and elongation are important aspects of maintaining fitness under stress and that these phenotypes are reflective of life strategy and local adaptation.

DISCUSSION

Imaging techniques are especially well suited for capturing phenotypes related to architecture due to their ability to quickly provide a permanent and detailed record of plant form. The techniques used in this thesis are low cost, simple to operate, have accessible analysis outputs, and complement conventional approaches to understanding plant architecture.

Measures of PAI estimated from canopy hemispherical imaging and light attenuation modeling effectively captured phenotypic and genotypic variation in aboveground productivity in a non-destructive manner. This approach took advantage of recent size and cost reductions in durable digital camera and hemispherical lens technology and proved to be a major time saver. In the applications presented in this thesis, collection of hemispherical images was limited by having to manually move the camera from plot to plot. Further improvements in phenotyping throughput can be achieved by mounting the imaging system on a ground based robot to enable more continuous data collection throughout the day and growing season. The deployment of hemispherical imaging on a ground based robot in energy sorghum shows that this method is scalable for larger crops and can achieve a volume of data collection similar to aerial platforms (Young et al. 2018). Regardless of platform, it should be emphasized that estimates of productivity generated from hemispherical imaging represent the influence of all canopy elements and do not distinguish between the specific structures that produce growth. Therefore, more tailored methods are required to characterize the specific features of variation in plant architecture that may contribute to productivity responses to stress.

Canopy hemispherical images collected at both dawn and midday revealed the degree to which the proportion of light penetrating the canopy changes throughout the day. This was coupled with direct measurements of leaf roll angle and leaf inclination angle to show that leaf rolling responses to water-deficit was responsible for reversible alteration of the canopy light

environment. Further improvements to this approach could combine the technique with the above-mentioned ground based robot and use a high resolution time course of image collection to determine the ideal observation window (Baret et al., 2017).

Overhead imaging of stable, dried, postmortem stem material combined field relevance with laboratory-based procedures and helped to redistribute processing time and effort to the off-season. The resulting images produced a permanent and detailed record of stem architectural responses to drought stress. Although the procedure in its current form is time consuming and destructive, the rich dataset produced can serve as a reference for validating results generated from remote-sensed whole-plant phenotyping efforts that utilize feature extraction software or produce latent space phenotypes (Chitwood and Topp, 2015; Gehan et al., 2017). For the purpose of characterizing variation in internode morphology and elongation in diverse mapping populations, *Setaria viridis* is an ideal model system.

The *Setaria viridis* x *Setaria italica* RIL population and North American *Setaria viridis* accession panel examined in this thesis each contain a wide range of informative phenotypic and genotypic variation related to architectural traits relevant to the improvement of next generation C_4 grass biofuel feedstocks. The RIL population contains variation resulting from the influence of both domesticated and weedy backgrounds while the accession panel reflects local adaptation to environments across North America. These mapping populations exhibited a large range of variation in traits including leaf rolling, growth strategies, internode morphology, and productivity responses to stress. Although *Setaria* is much smaller in stature and has a shorter life cycle than potential target feedstocks such as energy sorghum, miscanthus, and switchgrass, these traits have broad application in neo-domestication and improved stress tolerance (Sang, 2011; Meyer et al., 2012). The ability to detect genotype-to-phenotype associations related to these architectural traits allows for the improved description of syntenic regions in target next generation feedstocks using comparative genetics (Bennetzen and Freeling, 1997; Gale and Devos, 1998).

Realization of next generation C_4 grass biofuel feedstocks will require unique plant architecture targets compared to historical domestication efforts. Modern cereals are the result of selection for non-shattering seed heads, increased partitioning to reproductive versus vegetative biomass, and shortened internodes that resist lodging. In contrast, cellulosic feedstocks should emphasize stem architectures that maximize tiller size as well as leaf morphologies and

phytomer spacings that allow for efficient distribution of light deeper into the canopy. Furthermore, to ensure that productivity is maintained under marginal conditions, architectural responses to water-deficit such as the maintenance of internode elongation or leaf rolling should also be investigated.

Leaf rolling acts as a reversible form of leaf modification that helps to maintain productivity through periods of drought stress by reducing the amount of light intercepted by the canopy and reducing transpiration. The leaf rolling results presented in Chapter 3 are consistent with the trait being adaptive for C_4 grasses in conditions of moderate and variable drought stress. These results highlight *Setaria viridis* as an effective model for studying leaf rolling in C_4 grasses and provide a set of methods for studying the trait in the field with potential for improvements in throughput. Future research into leaf rolling in *Setaria viridis* can take advantage of the set of potential high and low rolling score parents to produce populations that emphasize variation associated with leaf rolling.

Results in Chapter 4 showed that internode morphology correlates with a number of traits relating to life strategy and with climate conditions. Internode elongation appeared to have a compensatory effect that recovers height lost early in growth to water-deficit. These results identify the distal-most vegetative internode and the peduncle as distinct developmental units that have contrasting responses to drought stress within the same plant where water-deficit has a negative impact on the elongation of the distal-most vegetative internode and a positive impact on the elongation of the peduncle. Martin et al. (2016) described a series developmental zones in an actively expanding internode and characterized the transcription patterns occurring within each zone. Together, the distal-most vegetative internode and the peduncle can serve as a complementary system for studying differences in the transcription and physiology of cellular elongation in actively expanding internodes experiencing drought stress. This approach would have the potential to determine which pathways are unique to positive versus negative elongation responses or how control of common pathways switches depending on location within vegetative versus reproductive phytomers. These controls can be compared to deep water rice internode elongation responses to flooding to examine the degree of conservation across genera (Nagai et al., 2012).

CONCLUSION

Improvements in the productivity and abiotic stress tolerance of next generation C_4 grass biofuel feedstocks are urgently needed in order to meet global demand for food, fuel, and industrial products. Due to its influence on productivity and mediation of the microenvironment, plant architecture provides a framework for targeted improvement of these feedstocks. *Setaria viridis* is an ideal model system for accelerating detection of useful genotype-to-phenotype associations and is gaining rapid adoption in the research community. Here, imaging techniques complemented by conventional direct measurements of plant architecture were used to assess genotypic and phenotypic variation in aboveground productivity, leaf rolling, and internode elongation responses to water-deficit in two *Setaria viridis* mapping populations. The approach showed that architectural responses to water-deficit are dynamic processes and detected genotype-to-phenotype associations that may be useful for informing improvement efforts broadly amongst C_4 grasses. Continued progress will require broader adoption of high-throughput phenotyping techniques coupled with mapping populations that emphasize variation in traits of interest.

REFERENCES

Baret F, Madec S, Irfan K, Lopez J, Comar A, Hemmerle M, Praud S, Tixier MH (2018) Leaf-rolling in maize crops: from leaf scoring to canopy-level measurements for phenotyping. **69:** 2705-2716

Bennetzen JL, Freeling M (1997) The unified grass genome: synergy in synteny. Genome Res **7:** 301-306

Chitwood DH, Topp CN (2015) Revealing plant cryptotypes: defining meaningful phenotypes among infinite traits. Curr Op in Plant Biology **24:** 54-60

Gale MD, Devos KM (1998) Comparative genetics in the grasses. PNAS **95:** 1971-1974

Gehan MA, Fahlgren N, Abbasi A, Berry JC, Callen ST, Chavez L, Doust AN, Feldman MJ, Gilbert KB, Hodge JG, et al. (2017) PlantCV v2: Image analysis software for high-throughput plant phenotyping. PeerJ **5e:** 4088

Martin AP, Palmer WM, Brown C, Abel C, Lunn JE, Furbank RT, Grof CP (2016) A developing *Setaria viridis* internode: an experimental system of the study of biomass generation in a C4 model species. Biotehnol of Biofuels **9:** 45

Meyer RS, DuVal AE, Jensen HR (2012) Patterns and processes in crop domestication: historical review and quantitative analysis of 203 global food crops. New Phytologist **196:** 29-48

Nagai K, Kuroha T, Ayano M, Kurokawa Y, Angeles-Shim RB, Shim JH, Yasui H, Yoshimura A, Ashikari M (2012) Two novel QTLs regulate internode elongation in deepwater rice during the early vegetative stage. Breeding Sci **62:** 178-185

Sang T (2011) Toward the domestication of lignocellulosic energy crops: learning from food crop domestication. JIPB **53:** 96-104

Young SN, Kayacan E, Peschel JM (2018) Design and field evaluation of a ground robot for high-throughput phenotyping of energy sorghum. Precis Agric doi: 10.1007/s11119-018-9601-6